Improving the functional connectivity magnetic resonance imaging (fcMRI) blood oxygenation level dependent (BOLD) signal through the characterization of processing effects

Andrew S. Nencka

May 27, 2009

Contents

List of Figures

List of Tables

Committee Members

Daniel B. Rowe[1,2] (Advisor)
James S. Hyde[1]
Kathleen M. Schmainda[1,3]
Raymond G. Hoffmann[2]
Douglas C. Noll[4,5]

[1] Department of Biophysics, Medical College of Wisconsin, Milwaukee, Wisconsin, United States
[2] Division of Biostatistics, Medical College of Wisconsin, Milwaukee, Wisconsin, United States
[3] Department of Radiology, Medical College of Wisconsin, Milwaukee, Wisconsin, United States
[4] Department of Biomedical Engineering, University of Michigan, Ann Arbor, Michigan, United States
[5] Department of Radiology, University of Michigan, Ann Arbor, Michigan, United States

Abstract

The functional connectivity blood oxygenation dependent signal in magnetic resonance imaging is measured by calculating the correlation of voxel time series. As this signal is small, non-negligible processing steps are applied to the acquired data. Some previous studies have developed empirical measures of the effects of such processing steps. In this work, we examine the effects of the processing steps through an exact, analytical framework. We parameterize the process of reconstruction as a linear process on a real-valued isomorphism of the acquired complex valued data. We then develop linear operators to perform standard image processing steps, including: echo planar data censoring, echo planar data reordering, Nyquist ghost elimination, partial Fourier reconstruction, intra-acquisition decay and decay correction, magnetic field inhomogeneity effects and magnetic field inhomogeneity correction, frequency-space apodization, and image-space smoothing. We further expand the linear framework to include processes which are applied to the acquired time series, including: the extension of image processing operations to temporal image processing operations, dynamic magnetic field correction, dynamic intra-acquisition decay correction, slice timing correction, motion correction, and temporal filtering. In each case of spatial and temporal processing, we analytically demonstrate the effects caused by applying the operators both individually and in groups and illustrate the results in acquired phantom data. The results of the analytical framework correspond well to the empirical results described by others. Finally, we motivate the implementation of the developed operators in experimental functional magnetic resonance imaging and functional connectivity magnetic resonance imaging data.

Chapter 1

Introduction

Over the past several years, our work has focused upon two central themes in functional and functional connectivity magnetic resonance imaging (fMRI and fcMRI): (1) obtaining more information from traditionally acquired data, and (2) understanding the implications which arise from unmodeled physical processes and unmodeled data processing. We have found these themes to be inherently interconnected and the following work is a subset of the advances we have made in our research endeavours.

This dissertation is organized in six chapters. The first chapter provides an introduction to our work, and highlights the background upon which it is based. The second chapter describes our initial attempt to use the traditionally discarded phase data in fMRI to identify the vascular source of observed signal contrast. That work, while providing insight to the performance of different phase-sensitive data analysis techniques, highlighted the enhanced need for processing complex-valued data. The following two chapters develop a linear framework for analytically considering the effects of spatial and temporal processing in fMRI and fcMRI. The results of those

chapters further confirm the importance of processing complex-valued data, and the described framework offers a method for including data processing in considered statistical models. We have since applied the particularly important process of dynamic magnetic field correction to both fMRI and fcMRI data, and our considerations of the latter are presented in the fifth chapter. The final chapter summarizes the results of the work presented in this dissertation and offers opinions as to where this line of research may lead in the future.

1.1 BOLD contrast

The blood oxygenation level dependent (BOLD) contrast mechanism is responsible for contrast with task in functional magnetic resonance imaging (fMRI) and is the cause of contrast in functional connectivity magnetic resonance imaging (fcMRI). Blood flow to the cortex increases with cortical activity. This activity may include specific task-related activity [Ogawa et al., 1993] or "spontaneous" activity [Biswal et al., 1995]. With the increase in blood flow, the concentration of deoxyhemoglobin decreases in the active capillaries and down stream veins. The functional contrast is a result of the blood flow increase outpacing the increase of the metabolic rate of oxygen consumption in the area of active cortex [Villringer, 2000]. The lower concentration of deoxyhemoglobin decreases the apparent magnetic susceptibility, causing it to become more diamagnetic. Thus, the susceptibility of the blood becomes closer to the susceptibility of the surrounding tissue, leading to more homogeneous magnetic fields at the vascular level. More homogeneous magnetic fields result in less dephasing of the precessing spin isochromats within an imaging voxel, and therefore increased signal intensity [Sprenger, 1994]. If the magnetic field perturbation of the altered

blood susceptibility is on the order of the size of the voxel, the signal change may be dominated by the accrual of a different net phase in response to the different magnetic field, rather than isochromat dephasing [Menon, 2002, Zhao et al., 2007, Feng et al., 2009].

BOLD MRI contrast has become the standard imaging contrast utilized for neuroscience and psychological study of the brain. A simple PubMed search of the literature from 2007 yields 20,254 results for functional MRI and 233 results for functional connectivity MRI. As shown in Fig. 1.1(a), these publications are part of a large and expanding area of research. Additionally, the use of functional connectivity MRI in research is growing rapidly as seen in Fig. 1.1(b). As functional connectivity is a rapidly expanding field of research, our work has aimed to address factors which may confound computed voxel correlations. Specifically, we have developed a theoretical framework to quantify correlations associated with some reconstruction and temporal preprocessing, and compared methods for separating global correlations caused by systemic physiologic processes that cause global magnetic field shifts, including respiration, from regional correlations associated with interesting physiology.

1.2 The ubiquity of data preprocessing

It is common to process fMRI and fcMRI data prior to statistical analysis. Such preprocessing arises from both necessities in image reconstruction and from yielding favorable results on computed activations.

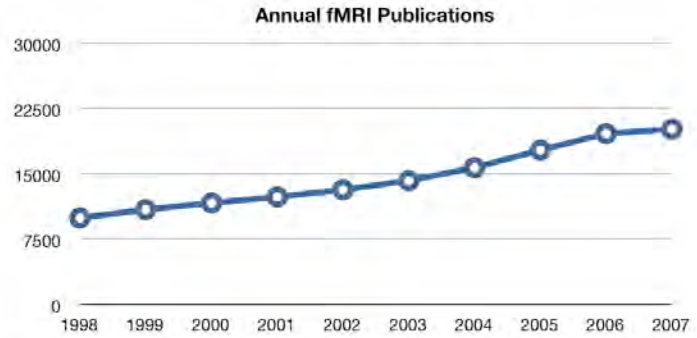

(a)

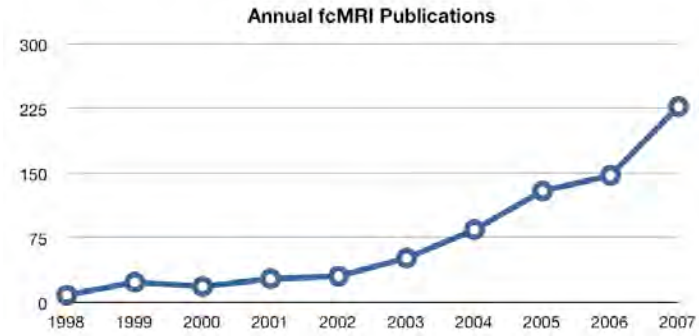

(b)

Figure 1.1: PubMed entries for functional MRI and functional connectivity MRI over the past ten years illustrate the increasing use of the methods in biomedical research.

Reconstruction preprocessing

In magnetic resonance imaging, the Fourier transform of the object being imaged is generally acquired. This acquisition technique only approximates the mathematical ideal of Fourier imaging. The Fourier transform requires an infinite continuous support. However, only a subset of the basis is acquired. Thus, only a small portion of the possible spatial frequencies are collected, with spatial frequencies above the observed frequencies assumed to be periodic copies of the acquired data. This results in the effective repetition of the Fourier reconstructed image with the Fourier transform of the acquired k-space. Therefore, with higher frequencies not observed and a periodicity assumed on the k-space data, step discontinuities in the reconstructed image are not effectively resolved. The Fourier reconstructed image is effectively smoothed with a sinc function defined by the observed window of k-space under ideal circumstances.

The physical process of transverse spin relaxation unavoidably occurs over the time in which a k-space acquisition is made. This spin relaxation causes the attenuation of the acquired signal over the period of acquisition, causing symmetric k-space points to be weighted differently by the signal decay. The temporal signal decay over the course of image acquisition causes blurring of reconstructed images [Haacke et al., 1999]. In echo planar imaging, the observation bandwidth is about one hundred times greater in the frequency encoding direction than in the phase encoding direction. The high bandwidth in the frequency encoding direction minimizes intra-acquisition decay associated blurring in that direction, while the low bandwidth in the phase encoding direction exacerbates such blurring in the phase encoding direction. Thus,

a non-isotropic point spread function exists in echo planar imaging because of the intra-acquisition decay.

Beyond such effects from the acquisition process, data processing often occurs in image reconstruction. Physical processes and limitations result in imperfections in the Fourier encoding of the acquired image. Gradient timing errors and eddy current effects can lead to alternating k-space lines being shifted from each other [Haacke et al., 1999]. This error in encoding results in an artifact in the representation of the lowest spatial frequency in the direction of phase encoding. This artifact is often called the Nyquist ghost, or the N/2 ghost, as it includes a low intensity duplicate of the desired image offset by one half of the field of view in the phase encoding direction [Bernstein et al., 2004]. To address this artifact, the offset of the alternating k-space lines may be calculated, and the lines shifted to correct it [Jesmanowicz et al., 1993, 1995, Nencka et al., 2008]. This preprocessing may correct the artifact, although it includes interpolation of the acquired k-space data to implement the shift. This interpolation may induce correlations in the acquired k-space data. As Fourier reconstruction is a linear process, correlations in k-space are necessarily associated with correlations in image-space.

In addition to timing and eddy current errors, concomitant static field errors may cause imperfections in the Fourier encoding of the acquired image. Such errors include the temporally varying image-space phase of the acquired image over the duration of the image acquisition. Such an error leads to the spatial warping of the acquired image [Jezzard and Balaban, 1995]. With the spatial warping, an interpolation process occurs in image space. Such warping may cause neighboring voxels to become

correlated.

Physical limitations of the scanner equipment may also cause imperfections in the acquisition of a time series of data. Rapidly switching, strong gradients associated with fast echo planar pulse sequences require high currents to be run through the gradient coils. This causes the coils to heat, thereby altering their resistivity. The altered resistivity results in a systematic error as a voltage applied to drive the gradient coils will lead to a magnetic field which is dependent upon the temperature of the gradient coils. This may lead to a temporal drift in the phase of the reconstructed images, or, in the case of extreme gradient heating, a bulk shift of the images in the phase encoding direction caused by the resulting resonance frequency offset [Jesmanowicz et al., 1995]. Image registration [Jenkinson et al., 2002] or ω_0 correction [Jesmanowicz et al., 1995, Nencka et al., 2008] are often performed to correct this artifact.

Beyond physical imperfections in the encoding process, there is a fundamental limitation to the observation process. That is, only a finite number of k-space points may be observed after the excitation of the spins. With only a limited number of points acquired, the assumption is made that only a limited region of k-space about its origin need be sampled. This under sampling of k-space makes it impossible to resolve step-like discontinuities of image-space contrast. Left unprocessed, such a discontinuity leads to the artifact of Gibbs ringing [Gonzalez and Woods, 1992]. To attenuate the effects of Gibbs ringing, the k-space observations may be apodized [Bernstein et al., 2004]. In such a process, the k-space values near the center of k-space are multiplied by unity, while observations near the edge of the acquisition are attenuated so that there is a smooth transition between the assumed periodic

values outside of the observed k-space values and the observed k-space values. This results in an image-space convolution of the acquired image with the inverse Fourier transform of the apodization mask, thereby smoothing out the Gibbs ringing caused by the discontinuity while also inducing spatial correlations in the reconstructed data.

In addition to apodization, some reconstruction software will add zeros to the edges of the k-space. This is required by older fast Fourier transform algorithms which require the input to be a power of two [Gonzalez and Woods, 1992]. This zero padding is equivalent to interpolating the image-space voxels with a two dimensional sinc wave, and may, therefore, induce correlations in the data.

Data analysis preprocessing

Distinct from the physical processes which occur during image acquisition and the associated preprocessing performed in reconstruction to correct artifacts induced by such processes, preprocessing may additionally be performed to yield more favorable results when statistically analyzing the acquired data.

Subject motion over the course of the time series acquisition may result in the change of imaged material within a voxel over time. Thus, a voxel which starts a time series completely containing active grey matter may finish the time series containing a combination of active gray matter, white matter and cerebrospinal fluid. This may lead to the voxel's intensity varying over the course of the experiment based upon the alteration of partial volume effects rather than functional activity. As the image shifts over the experimental run, voxels with similar compositions will be correlated as partial volume effects change. For this reason, some perform image registration over the course of the time series [Jenkinson et al., 2002]. This improves the stability

of functional time series by reducing the contribution from voxel composition varying over the course of the experiment. Of course, the image shifting which is associated with registration utilizes image interpolation procedures which may induce image correlations. Additionally, uncorrected residual motion will likely cause image-space correlations.

In addition to registration, many studies perform image smoothing. Smoothing is performed to highlight large regions of relatively weak activation while reducing activation contributions from significant but small regions [Skudlarski et al., 1999]. Smoothing may be performed by means of point-wise multiplying k-space observations with a windowing function, or equivalently by convolving with a smoothing kernel in image space. It is obvious that such a process will cause correlations between neighboring image-space voxels.

Beyond the purely spatial processing like smoothing, and the spatial and temporal processing like image registration, purely temporal processes may be implemented on the acquired data. Often multiple slices of a volume of interest are acquired over a repetition period. To make each slice represent the same time point of the acquisition, slice time series can be temporally shifted through interpolation so that each volume is effectively considered at the same time. This temporal process is called slice timing correction. Additionally, some temporal frequencies, like that of respiration, are known to contribute signal which is not of interest. Thus, temporal filtering may additionally be applied to the time series data. These temporal processing methods can lead to modifications of the temporal mean, covariance and correlation of the considered data.

The problem with preprocessing

Most cortical statistical activations are determined either through the fit of a general linear model [Friston et al., 1995] or through computing correlation coefficients between time series [Bandettini et al., 1993, Biswal et al., 1995]. Such methods are used to create statistical parameter maps which are in turn thresholded to produce maps of statistically significant activation or connectivity [Logan and Rowe, 2004, Logan et al., 2008]. Many thresholding processes require that each voxel time series is independent. Other thresholding techniques, including permutation resampling, have been implemented to control the family wise error (FWE) and false discovery rate (FDR) thereby relaxing the assumption of no spatial correlation [Logan and Rowe, 2004]. Additionally, many methods assume that the voxel observations are corrupted independent and identically distributed noise. Once again, more complicated statistical methods which allow for temporal correlation in the data including autoregressive models have been implemented to relax the necessary assumptions [Lou and Nichols, 2003].

Furthermore, differences exist between vendors in their reconstruction procedures. A prime example of such differences is the apodization process. The apodization process causes image smoothing. This smoothing affects local voxel time series correlations [Gretton et al., 2006]. The use of different apodization procedures by different vendors requires that images be processed to yield comparable smoothness for direct comparisons to be made, *even if scan acquisition parameters are identical* [Friedman et al., 2006].

1.3 Physiologic noise in functional connectivity magnetic resonance imaging

The functional connectivity magnetic resonance imaging experiment traditionally relies upon BOLD contrast in a time series of T_2^* weighted echo planar images. As a result of the required pulse sequence parameters, the T_2^* weighted images include contrast which arises from undesirable sources. This includes global changes in blood susceptibility as well as changes in magnetic field homogeneity.

Global changes of blood susceptibility are known to occur over the time scales used in functional connectivity magnetic resonance imaging studies. Such changes of susceptibility may occur through several mechanisms. Global changes in vasodilation or vasoconstriction alter the rate of blood flow to the brain. Such changes in blood flow alter the concentration of deoxyhemoglobin in the vasculature, thereby altering the blood susceptibility. This BOLD signal is not desirable as it is global in nature. Thus, it may confound local BOLD signals associated with cortical regions which are functionally connected.

Additionally, variations in blood pressure [Guyton and Hall, 2000] and respiratory depth [Birn et al., 2006] over the time series of the acquisition may alter the blood signal. As with vasoconstriction and vasodilation, changes in blood pressure may alter cerebral blood flow. These changes in flow may give rise to global BOLD effects. Respiratory depth alters the level of oxygenation of arterial blood. Such changes in oxygenation alter global blood oxygenation and global blood flow, thereby providing BOLD contrast.

Beyond physiologic BOLD contrast changes from global processes which are not of interest in functional connectivity studies, magnetic field alterations may be correlated to physiologic processes. Respiration includes the motion of the chest wall outside of the imaging plane but within the imager bore. This motion of magnetically susceptible material within the chest in the strong magnetic field of the imager yields magnetic field fluctuations [Raj et al., 2000]. Such magnetic field fluctuations may cause sub-voxel image shifts which alter voxel partial volume compositions, and thus cause voxel time series variance and covariance.

Other physiologic motion is related to the pulsatile flow of blood. The blood pulsations in the arteries of the brain cause a pulsation which is transmitted through the brain [Guyton and Hall, 2000]. Such brain pulsations associated with the cardiac cycle cause the brain to deform on the sub-voxel scale in functional studies, thereby altering voxel partial volume compositions. Such sub-voxel shifts can cause voxel time series variance and covariance.

1.4 Correcting physiologic noise in functional magnetic resonance imaging

Several methods have been developed to reduce the contributions from cardiac and respiratory effects. Some such methods are described below.

Respiratory effect correction

The effect of respiratory related out of field of view motion on images acquired with echo planar techniques has been described above. The underlying problem with out of field of view motion is that it modulates the magnetic field at the imaging plane.

Therefore, several techniques have been described to dynamically account for such magnetic field variations.

Most simplistically, the magnetic field offset associated with out of field of view motion may be considered as a uniform magnetic field shift at the imaging plane. Thus the resonant frequency of the acquired slice is shifted by$\Delta\ \omega = \gamma \Delta B$, where ω is the resonant frequency, γ is the gyromagnetic ratio, and B is the magnetic field. The offset of the resonant frequency may be considered through the use of navigator echoes [Jesmanowicz et al., 1995, Pfeuffer et al., 2002]. With the resonant frequency offset known, the acquired data may be appropriately corrected with k-space multiplication with $e^{-i\gamma \Delta B t}$, where t is the time at which the k-space point is acquired.

In image-space, the artifact associated with a resonance frequency offset is an image shift in the phase encoding direction. Thus, an alternative to such resonance frequency offset corrections is simply rigid body image registration. Such a correction may not only account for global resonance shifts caused by out of field of view motion, but also shifts of the imaged object over the course of the time series acquisition. The weakness of this method, as with all global resonant frequency correction methods, is that it will not address effects caused by local resonant frequency shifts within the imaging plane.

Other methods consider spatially varying magnetic field offsets caused by out of field of view motion. If the magnetic field offset is known, the shim coils responsible for the magnetic field homogeneity of the region being imaged may have their currents adjusted to correct for the magnetic field error. This has been proposed by van

Gelderen et al. [2007]. Magnetic field maps are first generated for a subject at several time points within the respiratory cycle. Then, when the imaging experiment is performed, the sim coil currents are adjusted to account for the magnetic field associated with the current phase of the respiratory cycle. While such a method allows for the correction of both in plane and through plane magnetic field inhomogeneities, any variations of the magnetic field with varied breathing patterns are not considered.

Other methods have been developed to retrospectively map and correct the magnetic field at the time the image was acquired. The moving race track trajectory may be used to acquire a second, low resolution image at a slightly offset echo time during and acquisition so that a low resolution magnetic field map may be calculated as $B = (\Delta\phi)/(\gamma\Delta TE)$ [Roopchansingh et al., 2003]. The spiral-in/spiral-out method acquires two images with different echo times as well to compute the magnetic field dynamically [Sutton et al., 2004]. With the magnetic field map known, it may be corrected with either time segmented [Noll et al., 1991] or frequency segmented methods [Noll et al., 1992], or variations thereof.

Other methods have been developed to consider changes in the magnetic field between two images acquired at the same echo time as$\Delta\ B = (\Delta\phi)/(\gamma TE)$ [Lamberton et al., 2007, Hahn et al., 2008]. These methods are unable to compute the net magnetic field, although they allow for the consideration of dynamic magnetic field changes over the course of an experiment, without modification of the standard echo planar imaging pulse sequence. Minor alterations to the sequence may be implemented to also acquire a static magnetic field map to correct bulk image warping. With dynamic magnetic field maps calculated, the magnetic field alterations may be

corrected.

A further method to correct magnetic field alterations is the phase regressor method described by Menon [2002]. This method requires that, for each voxel time series, magnitude is regressed as a linear function of phase. This fit is then used to estimate a magnitude value for each time point based upon the observed phase. The estimated magnitude is subtracted from the observed magnitude, yielding a corrected magnitude time series. The multi-step process is described by the equations $M_c = M_o - M_e,\ M_e = \alpha\phi + \delta$, where M_c is the corrected magnitude time series, M_o is the original magnitude time series, M_e is the estimated magnitude time series, ϕ is the temporally unwrapped phase time series, and α and δ are fit parameters. The fit parameters are estimated using a regression model assuming normal errors in both magnitude and phase observations. The corrected magnitude time series is then analyzed. This method has been demonstrated to reduce activation contributions from voxels with draining veins and correct voxels contaminated by motion artifacts [Menon, 2002, Martin et al., 2004, Barry et al., 2008].

Chapter 2

Functional Activations in Complex Data

We begin the substantive portion of this dissertation by both illustrating a potential use of the complex-valued data which is generally acquired but not analyzed, and illustrating the need for appropriate image processing. In this chapter we describe the use of phase to identify contributions from macrovascular sources in fMRI. We characterize the performance of two previously published statistical methods to reduce macrovascular contributions to computed cortical activations, the phase regressor method and the complex constant phase method, through simulation and we apply the methods to a small group of experimental data. Through the simulation, we find fundamental differences in the performance of the different statistical methods which lead to varying performance in the acquired experimental data. Furthermore, we find that the considered statistical methods are sensitive to non-task related phase fluctuations. We conclude that the complex constant phase method exhibits more favorable characteristics than the phase regressor method in both the simulated and experimental data. We further conclude that additional processing of

the complex-valued data is necessary to improve the robustness of complex-valued functional image analysis.

2.1 Introduction

The measured signal in MRI can be encoded to represent the complex-valued Fourier transform (FT) of the object being imaged. The image is generally reconstructed by performing an inverse Fourier transform (IFT) on the collected data [Rowe et al., 2007b]. The object is physical, and is thus real-valued. Therefore, under ideal conditions, the FT of the object would result in observed complex-valued data and the IFT of this data would result in the reconstruction of the unaltered, real-valued image of the object. However, small scale inhomogeneities in the magnetic field and measurement noise lead to complications in this mathematical treatment of the data [Haacke et al., 1999]. The reconstructed image is thus complex-valued, and can be visualized through a unique representation in real and imaginary images.

Functional MRI (fMRI) traditionally relies upon the statistical analysis of time series of magnitude-only images using blood oxygen level dependent (BOLD) contrast to determine areas of cortical activation [Ogawa et al., 1993, Bandettini et al., 1993, Cox et al., 1995]. Because popular methods of determining brain activation through fMRI only utilize magnitude images over the experimental time course, they discard information about small scale magnetic field disturbances contained in the complex-valued data, or phase image time course [Rowe and Logan, 2004]. This phase data is often corrupted by physiologic processes, slight subject motion and other noise [Pfeuffer et al., 2002]. In spite of the noise in this data, some have proposed using the information in this data to improve the detection power of activation methods

[Lai and Glover, 1997, Nan and Nowak, 1999]. Others have directly used the phase information alone to detect activations [Rowe et al., 2007a]. This phase data, related to local magnetic field changes, may hold a great deal of information about the source of the BOLD signal.

The BOLD signal arises from changes in blood oxygenation, and is thus sensitive to the capillaries where the oxygenation change occurs and down stream draining veins. With activation the concentration of oxyhemoglobin in the active capillaries and veins increases, effectively altering the blood's susceptibility. This leads to a change in the magnetic field within active vessels which correlates with the activity. Thus, the magnetization within these active vessels will acquire a different net phase with activation than with rest. If the active vessels within a voxel are large well oriented draining veins which contribute strongly to the observed signal, they will contribute a task related phase change [Menon, 2002]. Smaller venules and capillaries located in the parenchymal tissue, which are more randomly oriented, more densely packed, and carry a smaller volume of blood, lead to random de-phasing without a preferential direction. Therefore, because of these randomly oriented phase alterations within a voxel in the parenchyma, the signal will decay but will not exhibit a coherent phase change. The orientation of the vessels with respect to the magnetic field, and many other variables, will obviously affect the strength of the task related phase change (TRPC), as it will be minimized, for instance, with the vein at the "magic angle." Thus voxels with TRPCs will most likely be contaminated by the macrovasculature while it is not certain that voxels without TRPCs are free from draining veins [Klassen and Menon, 2005].

Because it is believed that the most relevant cortical activations detected through BOLD contrast are those which are tied to the microvasculature where the blood oxygenation change occurs, many attempts have been made to reduce the contributions from the macrovasculature, or large draining veins, to the BOLD computed cortical activations. In standard resolution fMRI, activations from draining veins are generally not of concern as such veins are co-localized in voxels with active parenchyma. Further down stream, the venous blood is diluted resulting in less signal change. It has been shown that with an active cortex area of 100 mm^2 such dilution is observable about 4 mm down stream from the active cortex, with only 1/4 of the oxygenation change of active cortex up to 25 mm away [Turner, 2002]. In higher resolution fMRI, however, this draining vein signal becomes more problematic. Draining vein contributions are less consistently co-localized in voxels with active parenchyma and they may be several voxels away from the active cortex. Furthermore, smaller voxel volume leads to attenuated partial volume effects and intra-voxel dephasing, allowing draining veins to have a greater influence in the signal of down stream voxels. Thus, the delocalization of activations from draining veins becomes problematic when higher resolution fMRI is used.

It is the goal of this paper to explore two recently proposed post-processing methods which utilize the magnitude and phase components of the complex-valued signal to determine BOLD cortical activations. It has been suggested that the complex phase regressor method localizes computed activations to the parenchyma by reducing draining vein contributions [Menon, 2002]. Likewise, Rowe and Logan's method of magnitude activation in complex data assuming constant phase has been claimed to

both localize activations to the parenchyma and reduce the draining vein component of activations [Rowe and Logan, 2004, Rowe, 2005c, Nencka and Rowe, 2005]. In this study, we compare the ability of the two statistical techniques to bias against voxels which exhibit task related phase changes under ideal simulated conditions. We also discuss the application of these techniques to preliminary experimental data and several confounding factors which must be resolved for such phase-based draining vein identification to be practically implemented.

2.2 Statistical Methods

We first briefly outline the parameterization of the advanced statistical activation detection techniques and offer illustrative simulated voxel time series. Both the phase regressor and complex constant phase methods employ the use of general linear models. Simple general linear models are well developed in the literature. Further descriptions of the implementations of the phase regressor and complex constant phase models are given in Appendices A and B.

The phase regressor method (Menon, 2002) assumes normally distributed noise on the magnitude and phase data. The model also assumes that task related magnitude changes associated with draining veins are linearly related to the task related phase changes of those veins. Assuming errors in both variables, the magnitude values for a time series are regressed as a function of the corresponding phase values for a given voxel. Based upon each phase time point value, an estimated magnitude is determined using the computed regression. This phase-estimated magnitude is then subtracted from the observed magnitude to discount the phase associated magnitude component in a "phase corrected" magnitude time series. The common magnitude-only general

linear model is then used to analyze the corrected magnitude time series.

Examples of this method are illustrated through simulated voxel time series shown in Fig. 2.1. The simulated data were created using the complex-valued general linear model as described by Rowe [2005a]:

$$\begin{aligned} Y_t &= [(\beta_0 + \beta_1 t + \beta_2 x_{2t}) \cos(\gamma_0 + \gamma_1 t + \gamma_2 x_{2t}) + \eta_{Rt}] \\ &\quad + i[(\beta_0 + \beta_1 t + \beta_2 x_{2t}) \sin(\gamma_0 + \gamma_1 t + \gamma_2 x_{2t}) + \eta_{It}]. \end{aligned} \tag{2.1}$$

In all cases, no linear trend was modeled in phase, $\gamma_1 = 0$, and β_2, γ_2, and β_0 were set to determine the contrast-to-noise ratio (CNR $= \beta_2/\sigma$), task related phase change (TRPC $= \gamma_2 * 180/\pi$), and signal-to-noise ratio (SNR $= \beta_0/\sigma$). In Figs. 2.1(a) and 2.1(d) the ideal magnitude time series (red), noise corrupted time series (green), phase corrected magnitude time series (blue) and phase regressor model fit (black) are shown. Figs. 2.1(b) and 2.1(e) depict the corresponding ideal and simulated phase time series. In Figs. 2.1(c) and 2.1(f) scatter plots of magnitude (vertical axis, arbitrary units) and phase (horizontal axis, degrees) are shown for time points during the active (star) and inactive (circle) periods. The regression for magnitude as a function of phase, accounting for errors in both variables, is shown by the solid black line.

The first row of Fig. 2.1 is for a time series with a very strong task related magnitude changes (CNR = 1) and no task related phase changes (TRPC = 0°), as would be expected in a voxel containing only parenchyma. It can be seen that the phase regressor method preserves the statistically significant block design in the

corrected magnitude time series with reduced magnitude.

The second row of Fig. 2.1 depicts a time series with a moderate task related magnitude change (CNR = 0.78) and moderate task related phase change (TRPC = 2°), as could be expected in a voxel containing a draining vein. In this case, error in the fit of the magnitude as a function of the phase leads to a statistically insignificant over-correction of the magnitude data in the phase corrected magnitude data. Thus, while the original magnitude-only time series exhibits a statistically significant block design, the corrected time series does not as the phase regressor method subtracts larger magnitude estimates from the observed magnitude time series during active blocks, reducing the statistical significance of the activation statistic.

The complex constant phase method [Rowe and Logan, 2004] aims to bias against time series which exhibit phase changes through an entirely different mechanism than the phase regressor model. The complex constant phase method models the entire complex-valued voxel time series in a general linear model. This statistical model assumes normally distributed noise on the complex-valued data and assumes that the phase is temporally fixed on a voxel-wise basis. Thus, the model simultaneously fits a block design to the magnitude data and a constant phase to the phase data. When a time series exhibits phase changes, the fit of the constant phase to the incorrectly modeled temporally varying phase leads to an increase in the variance of the residuals from the fit model. As it is shown in Appendix B, an increase in the variance of the residuals from the fit model will lower the computed activation statistic. Thus, the bias against voxels with phase changes in the complex constant phase statistical method is achieved through the increase of the variance of the residuals from the

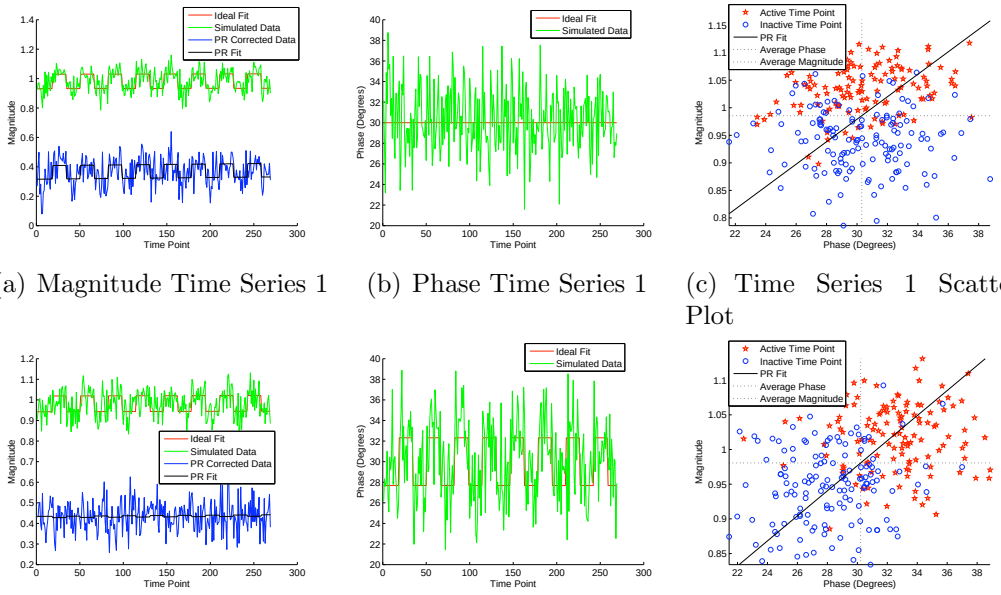

(a) Magnitude Time Series 1 (b) Phase Time Series 1 (c) Time Series 1 Scatter Plot

(d) Magnitude Time Series 2 (e) Phase Time Series 2 (f) Time Series 2 Scatter Plot

Figure 2.1: Simulation Time Series for CNR=1, TRPC=0° (row 1) and CNR=0.78, TRPC=2° (row 2). Figures (a) and (d) illustrate the ideal magnitude time series (red), simulated magnitude time series (green), phase corrected magnitude time series (blue) and fit phase regressor model (black). Figures (b) and (e) illustrate the ideal phase time series (red) and simulated phase time series (green). Figures (c) and (f) show scatter plots of the active (star) and inactive (circle) time points with phase (in degrees) on the horizontal axis and magnitude (arbitrary units) on the vertical axis. The fit of magnitude as a function of phase for the phase regressor method is shown as a solid line and the mean phase angle and mean magnitude value are shown as dotted vertical and horizontal lines respectively.

model in voxels with phase changes. This is opposed to the empirical modeling of the mangitude-phase relationship determined in the phase-regressor model. Instead of modeling the draining vein response, the complex constant phase method relies upon a reduced statistical fit of the model in expected draining veins. This identification of veins based upon a reduced fit of the model, rather than directly modeling the venous response, can be a criticism of the complex constant phase statistical model.

Example time series for the constant phase method are shown in Fig. 2.2. The first row shows an active voxel with a strong magnitude change (CNR=1) and no task related phase change (TRPC=0°). This data is the same as presented in Figs. 2.1(a), 2.1(b), and 2.1(c). The magnitude fit is in good correspondence to the data and is seen that the errors from the phase time series fit result only from the phase noise. The residual variance from this fit is identical to that of the magnitude-only fit. The second row includes a time series from a simulated voxel with a moderate magnitude change (CNR=0.35) and large task related phase change (TRPC=4°). These parameters differ from those in Figs. 2.1(d), 2.1(e) and 2.1(f) as the models exhibit favorable vein reducing characteristics with different CNR/TRPC combinations, as will be discussed in the next section. As in the previous case, the magnitude fit from the constant phase method is good, nearly corresponding to the ideal simulated data. However, the residuals of the phase model are inflated through the addition of the structured phase change in addition to the random phase noise. This leads to an increase in the variance of the fit model's residuals and a corresponding decrease in the associated activation statistic. Thus, the constant phase method biases against voxels with temporally non-constant phase, including voxels with task related phase changes because of the

reduced model fit to the data.

2.3 Computer Simulation Study

2.3.1 Methods

To examine the properties of these statistical activation detection methods under known conditions a simulation was performed in MATLAB (The Mathworks, Natick, MA, USA). In the simulation, time courses for each pixel of a 128 $\times$ 128 array were first created using the complex-valued general linear model defined in Eqn. 2.1. In all cases, there was no linear trend in the phase ($\gamma_1 = 0$). All pixels were made active so that a non-zero contribution was made by the reference function to the magnitude and/or phase data ($\beta_2 = 0$ to σ and $\gamma_2 = 0$ to $5\pi/180$). The strengths of the magnitude contributions were determined by setting the temporal contrast-to-noise ratios (CNR= β_2/σ), and the strengths of the phase changes were determined by setting γ_2s, and thus the number of degrees in the task related phase changes (TRPCs). In all of the 128 $\times$ 128 pixels, the complex-valued simulated data was corrupted with randomly generated, normally distributed noise in the real and imaginary components with a temporal signal-to-noise ratio (SNR= β_0/σ) of 20. This temporal SNR approximately corresponds to the SNR measured in the human data presented later, as determined by the β_0 and σ terms in the magnitude-only general linear model regression. Each pixel of the 128 $\times$ 128 array was assigned a different CNR-TRPC combination, for a total of 16384 separate combinations. One thousand iterations of computing activations on different generated data sets were performed to determine powers of the various method for declaring pixels active above an $\alpha = 0.05$

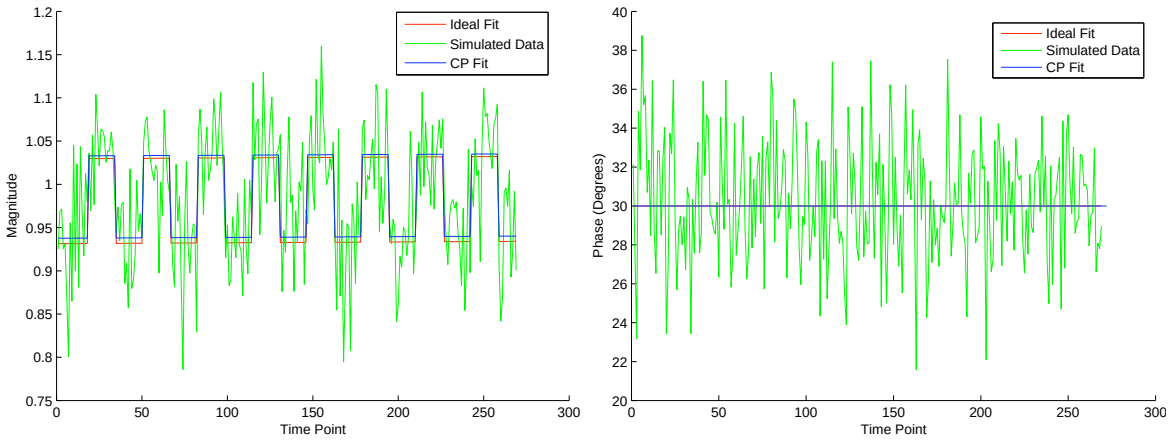

(a) Magnitude Time Series 1

(b) Phase Time Series 1

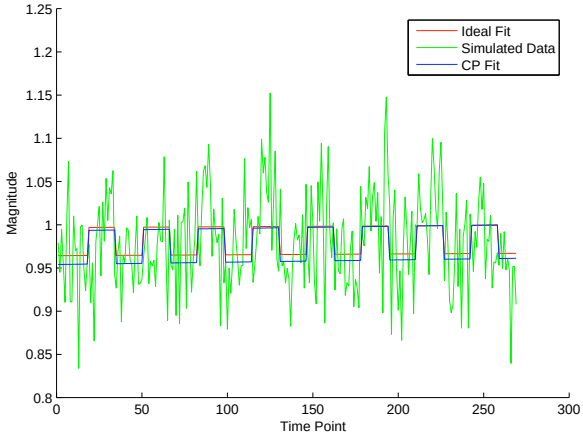

(c) Magnitude Time Series 2

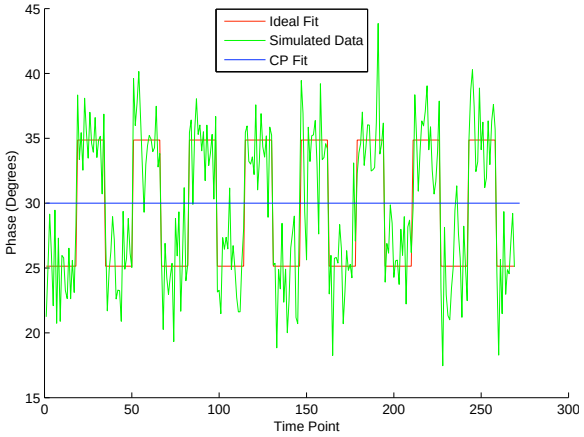

(d) Phase Time Series 2

Figure 2.2: Simulation Time Series for CNR=1, TRPC=0° (row 1) and CNR=0.35, TRPC=4° (row 2). Figures (a) and (c) illustrate the ideal magnitude time series (red), simulated magnitude time series (green), and constant phase fit (blue). Figures (b) and (d) illustrate the ideal phase time series (red), simulated phase time series (green), and constant phase regression fit (blue). The constant phase regression of the phase is coincident with the ideal phase time series in (b).

Bonferroni adjusted threshold in each iteration of this simulation [Logan and Rowe, 2004]. The activation power for a method was defined to be the percentage of times in the one thousand data sets that a pixel was declared active by that method.

2.3.2 Results

The results of the simulation are shown in Fig. 2.3. The horizontal axis represents the CNR, as it changes from 0 on the left hand side to 1 on the right hand side in 128 equal steps, and the vertical axis represents the TRPC as it changes from 0° on the top to 5° on the bottom in 128 equal steps. Each subfigure depicts a surface indicating the power of each post-processing method for detecting activations with the varying CNR-TRPC combinations.

As shown in Figs. 2.3(a) and 2.3(b), both the magnitude-only and phase-only statistical methods are dependent upon only the CNR and the TRPC respectively. However, the complex constant phase and complex phase regressor analysis methods show obvious dependencies upon both the CNR and TRPC. As seen in Fig. 2.3(c), with small TRPCs, just like the magnitude-only method, the complex constant phase statistical method declares all voxels with significant CNRs active with high power. Such TRPC-CNR combinations are observed in parenchymal voxels. However, as TRPCs increase, this similarity between the magnitude-only and complex constant phase statistical methods diminishes, as also shown in an abstract by Nencka and Rowe [2006]. When larger TRPCs are present in the time series, the constant phase method requires a higher CNR to declare voxels active. In the brain, such voxels with moderate CNRs and larger TRPCs include voxels which contain draining veins. Thus, this simulation suggests that the complex constant phase method may bias against

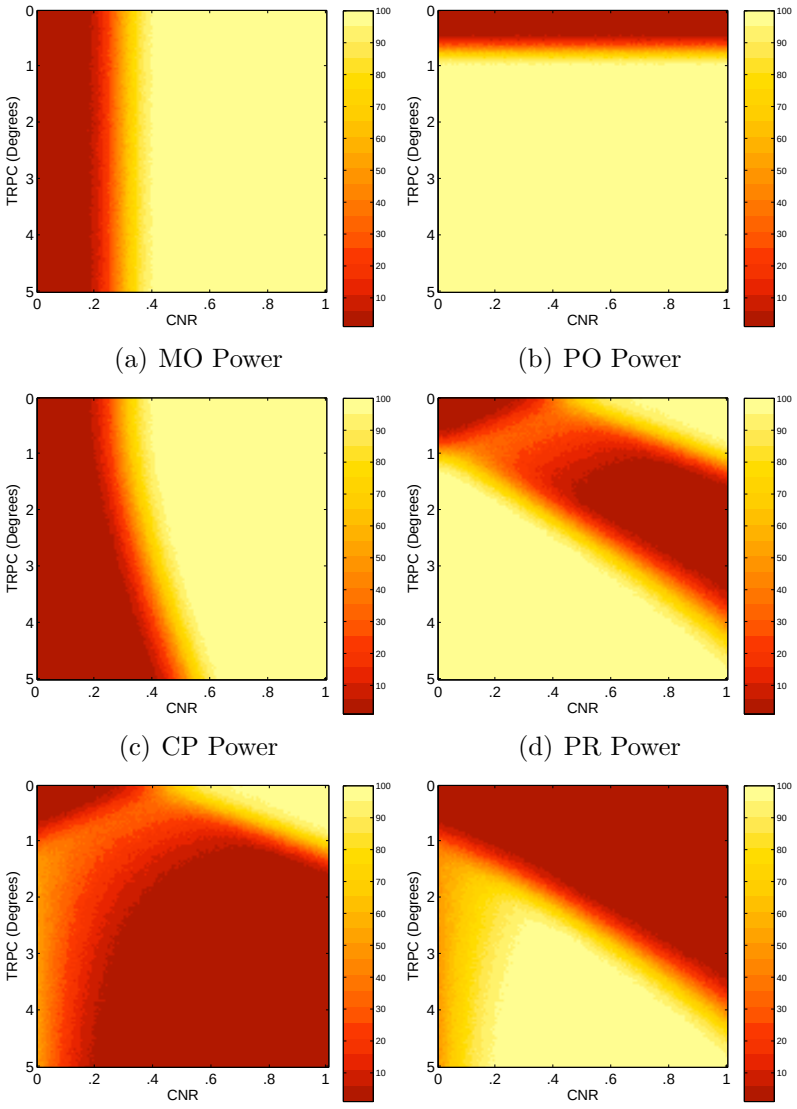

(a) MO Power (b) PO Power

(c) CP Power (d) PR Power

(e) PR (+) Power (f) PR (-) Power

Figure 2.3: Simulation z-Statistic Activation Power Surfaces. The magnitude-only (MO, a), phase-only (PO, b) and constant phase (CP, c) methods positive z-statistic power surfaces are identical to the shown unsigned surfaces. The MO and PO methods are dependent upon only CNR and task related phase change (TRPC) respectively. The CP method biases against larger TRPCs. The phase regressor method (PR, d) includes positive and negative statistics. Positive z-statistic PR method (e) exhibits a sharp bias against TRPCs and fails if a voxel exhibits a small CNR. When large TRPCs are observed in voxels, the negative PR method (f) over-corrects for phase-related magnitude changes.

such voxels which may contain draining veins. However, if a voxel contains both a large TRPC and CNR, the constant phase method declares the voxel active with the same power as the magnitude-only method. These TRPC-CNR combinations can result from large draining veins which exhibit extraordinarily large CNRs. In such cases, the constant phase method does not bias against the contaminated voxels. This suggests that the complex constant phase method may bias against some voxels with TRPCs while not removing all of them.

As shown in Figs. 2.3(d), 2.3(e) and 2.3(f), the phase regressor method yields more complicated results than the other methods which are more easily understood with the analysis of individual time series in Figs. 2.1 and 2.4. In the situations shown in Fig. 2.1, the phase regressor statistical method performs as expected when there are small TRPCs and large CNRs by biasing against time series with TRPCs. However, errors can be introduced into the analysis through errors in the regression of magnitude as a function of phase. Examples of such errors are shown in Fig. 2.4 as two simulated time series with identical parameters but different seed values for the random noise yield different phase regressor statistics. Slight errors in the estimation of the phase or magnitude variance needed for the fit assuming errors in both variables can lead to large variation in the fit. With small CNRs this leads to occasional over and under-correction of the magnitude signal. In Fig. 2.3(e) this is responsible for the band of moderate power with small CNRs. With larger CNRs, the errors in the fit from either over-estimating the phase variance or under estimating the magnitude variance dominate as the magnitude time series are systematically over-corrected. In Fig. 2.3(f) this is responsible for the large region of determined negative correlation,

although no negative correlation was simulated.

In the region where the phase regressor method performs as expected, it exhibits a bias against smaller TRPCs which is sharper than the complex constant phase method. Additionally the phase regressor method exhibits a bias against smaller CNRs with no TRPCs that the complex constant phase method does not exhibit.

This simulation on ideal data suggests that the complex constant phase method may exhibit a more conservative region of activations, possibly including some draining vein activations with large TRPCs. The phase regressor method may exhibit a more aggressive bias against draining veins under ideal conditions, but it also may include many false positives from slight errors in the regression of magnitude as a function of phase. Additionally, the constant phase statistical method retains the power of the magnitude-only method at low CNRs when no TRPCs are present while the phase regressor method requires a higher CNR to find activations.

2.4 Preliminary Human Experimental Study

2.4.1 Methods

A preliminary human study was performed that consisted of a blocked design bilateral finger tapping experiment to yield activation in the primary motor cortex and an angiogram was obtained to identify large veins. The task consisted of resting 20 seconds, followed by 8 epochs of 16 seconds of tapping and 16 seconds of rest. Each subject (N=5) performed the task while being imaged using a gradient recalled echo EPI pulse sequence. Scanning used a GE Signa LX 3T scanner with a quadrature receive coil, where 10 axial slices of 96×96 were acquired in the motor cortex.

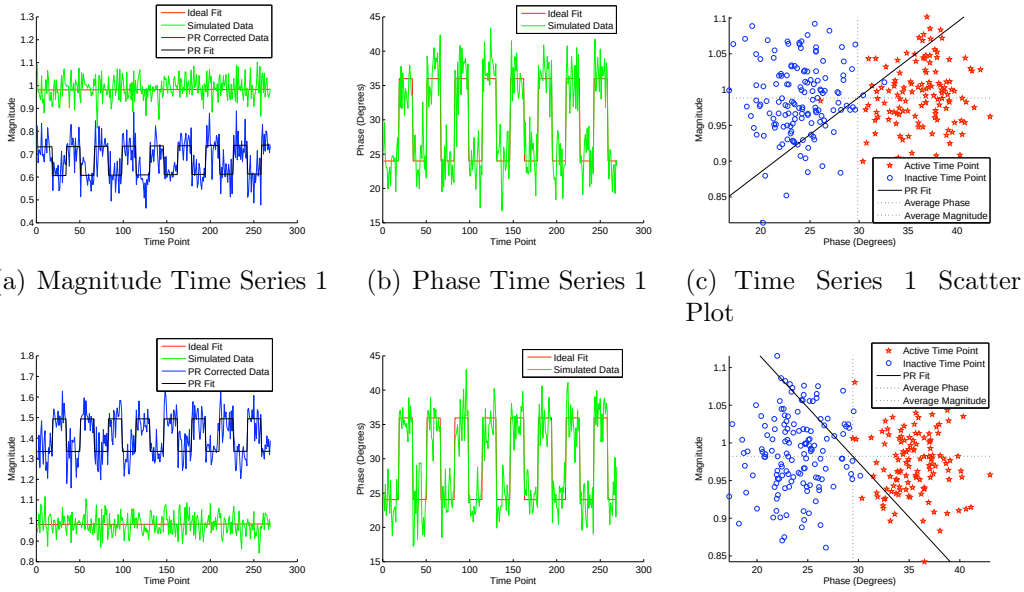

(a) Magnitude Time Series 1 (b) Phase Time Series 1 (c) Time Series 1 Scatter Plot

(d) Magnitude Time Series 2 (e) Phase Time Series 2 (f) Time Series 2 Scatter Plot

Figure 2.4: Simulation Time Series for CNR=0 and TRPC=5°. The first row shows a time series with the complex data corrupted by normal noise and the second row shows the same time series with the random noise generated by a different seed value. Figures (a) and (d) illustrate the ideal magnitude time series (red), simulated magnitude time series (green), phase corrected magnitude time series (blue) and fit phase regressor model (black). Figures (b) and (e) illustrate the ideal phase time series (red) and simulated phase time series (green). Figures (c) and (f) show scatter plots of the active (star) and inactive (circle) time points with phase on the horizontal axis and magnitude on the vertical axis. The fit of magnitude as a function of phase for the phase regressor method is shown as a solid line and the mean phase angle and mean magnitude value are shown as dashed vertical and horizontal lines respectively. The expected fit of the magnitude as a function of phase corresponds to the horizontal dotted line at the mean magnitude value.

Slices demonstrating activation in the primary motor cortex as well as superior slices containing draining large veins as identified in the angiogram were examined in this study. The scanning parameters for the EPI acquisitions included a minimum full k-space TE of 50 ms, TR of 2000 ms, flip angle of 80°, field of view of 19.2 cm, slice thickness of 2 mm, and 138 time points. This resulted in 2 mm isotropic voxels. Data was pre-processed to correct for minor k-space offsets in alternating lines caused by eddy currents. A time of flight spoiled gradient recalled echo pulse sequence was used to acquire an angiogram. Parameters for this sequence included an acquisition matrix of 256×256, TE of 5.1 ms, TR of 40 ms, flip angle of 40°, field of view of 24.0 cm, and slice thickness of 1.4 mm. This sequence saturates the stationary tissue signal, allowing the unsaturated in-flowing blood to be imaged as a hyper-intense.

Algorithms developed in MATLAB (The Mathworks, Natick, MA, USA) were used to compute activations in the functional data. Before computing activations, an ideal 0/1 frequency filter [Gonzalez and Woods, 1992] was used to remove respiration and extremely low frequency noise from signal drift in the voxel time courses [Smith et al., 1999]. Also, the first three time points were removed from analysis to adjust for signal stabilization. Activation statistics were then computed using the magnitude-only statistical method, unwrapped phase-only statistical method, phase regressor statistical method as described in Appendix A [Menon, 2002], and complex constant phase statistical method as described in Appendix B [Rowe and Logan, 2004]. The resulting z-statistic activation maps were thresholded using a Bonferroni adjusted $\alpha = 0.05$ threshold on a per-slice basis [Logan and Rowe, 2004]. No clustering techniques were considered to show the raw results of applying the statistical methods

and because the methods were originally presented assuming no spatial correlation in activations. Each thresholded activation map was overlaid on the first slice of the functional time series for anatomical reference. Additionally, the corresponding slices from the angiograms were examined to determine the localization of large draining veins.

In all subjects eight axial slices were considered, with four through the active parenchyma and four through superior slices as pial veins draining the motor cortex run superiorly to the sagittal sinus. The slices with active parenchyma were chosen as the slices with the highest number of voxels with magnitude-only activation z-statistics above a slice-wise $\alpha = 0.05$ Bonferroni adjusted threshold in the motor cortex. The superior slices with draining pial vein contributions were selected as slices at least 4 mm superior to the previously described slices and exhibited phase-only activations [Rowe et al., 2007a] along the cortical surface. These activations were near the central sulcus and coincided with the anatomical locations of pial veins in the angiogram. Furthermore, signal loss due to venous dephasing was also observed in the regions of the expected draining veins. EPI slices were not registered to the corresponding angiogram slices because small scale B-field inhomogeneities caused minor warping in the EPI images preventing accurate alignment with the small structures observed in the angiogram.

2.4.2 Preliminary Results

Representative activation maps shown in Fig. 2.5 . The anatomical underlays for these parenchymal and venous slices are shown in Figs. 2.6(a) and 2.6(c), respectively, with the angiograms shown in Figs. 2.6(b) and 2.6(d). Note that the activations in

the parenchymal slice (Fig. 2.5(a)) do not correspond with hyper-intense signal in the angiograms while the activations in the venous slice (Fig. 2.5(e)) are well localized with the hyper-intense vascular signal in the venous slice. Furthermore, stronger negative activation statistics are found with the phase-only statistical method in the regions of the active veins in Fig. 2.5(f), while very few phase-only activations are found in the parenchymal slice in Fig. 2.5(b). Other less significant phase activations are seen in Fig. 2.5(f), as likely the result of task related, out of field of view motion.

The parenchymal slice constant phase activations in Fig. 2.5(c) are a subset of the activations found through the magnitude-only method in Fig. 2.5(a). The constant phase activations in the parenchymal slice are a small subset of the magnitude-only activations, although the voxels do not exhibit statistically significant TPRCs. The reduction of constant phase activations is only partially explained by sub-threshold TRPCs. At this time, the data is not of sufficient quality to produce the stable phase time series required for the complex constant phase statistical model. The constant phase model is vulnerable to instabilities in the phase time series, not only phase instabilities which correlate with the task. In the real data, phase instabilities which are off the task frequency exist. Thus, in the parenchymal slice, both sub-threshold TRPCs and other temporal phase instabilities lead to lowering the statistical significance of the suspected constant phase parenchymal activations. As discussed later, modified acquisition techniques may improve the phase stability of the time series and thus improve the results of the constant phase model.

The results of the constant phase method in the venous slice (Fig. 2.5(g)) are also a small subset of the magnitude-only activations (Fig. 2.5(e)). As apparent

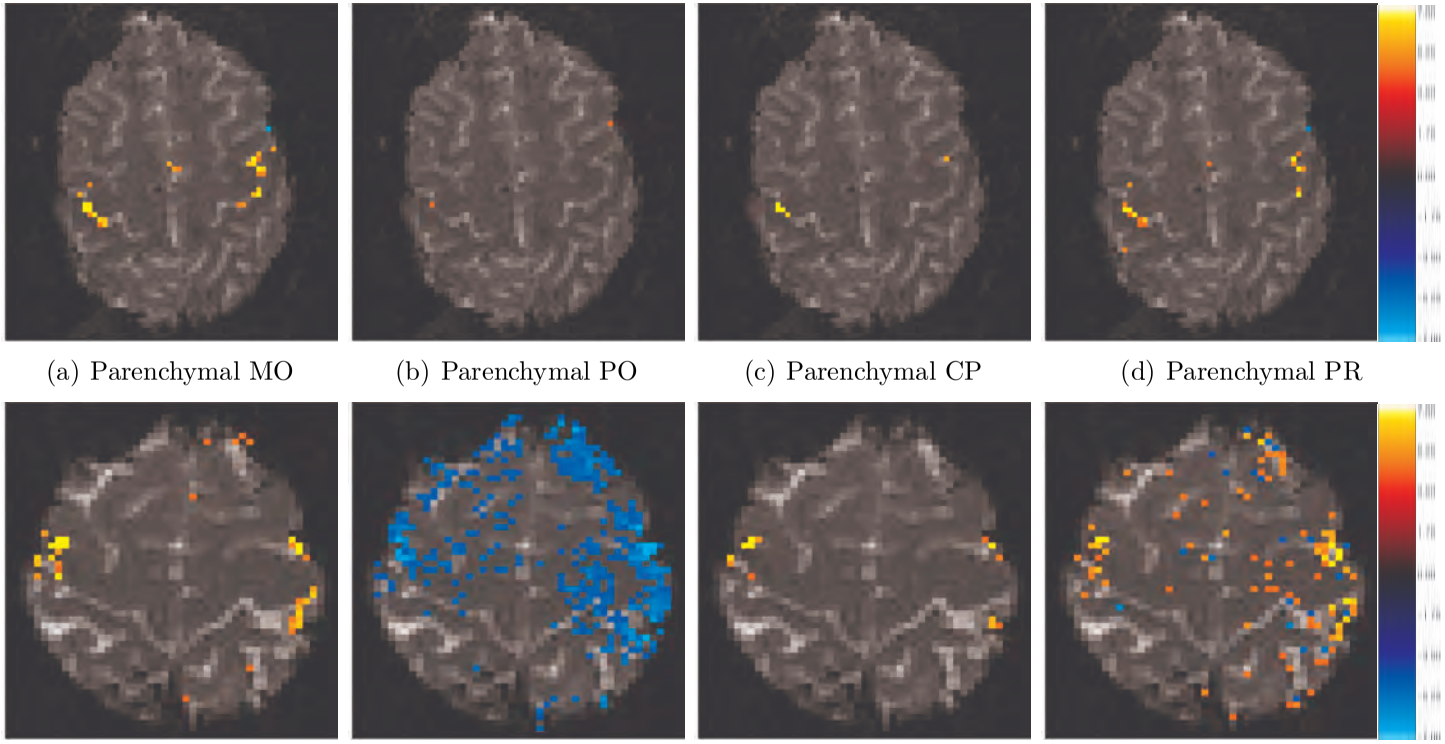

(a) Parenchymal MO (b) Parenchymal PO (c) Parenchymal CP (d) Parenchymal PR

(e) Venous MO (f) Venous PO (g) Venous CP (h) Venous PR

Figure 2.5: Representative activations from the human data are shown in a parenchymal slice (first row) and venous slice (second row) cropped to the region around the brain. MO activations are shown in (a) and (e), PO activations in (b) and (f), CP activations in (c) and (g), and PR activations in (d) and (h). The CP activations are generally a subset of the MO activations, while the PR activations include many voxels which are not MO active. The PO time series suffers from several confounding factors and leads yield diffuse activations in (f).

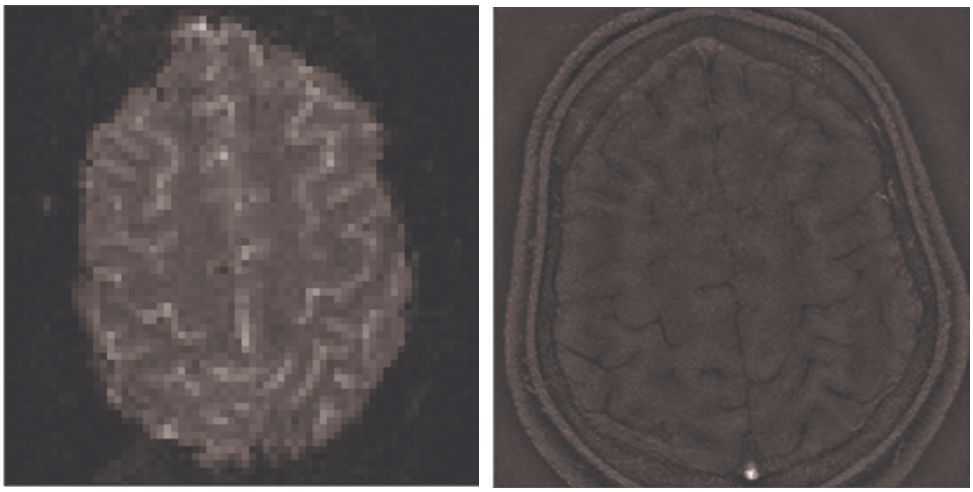

(a) Parenchymal Slice Anatomical (b) Parenchymal Slice Angiogram

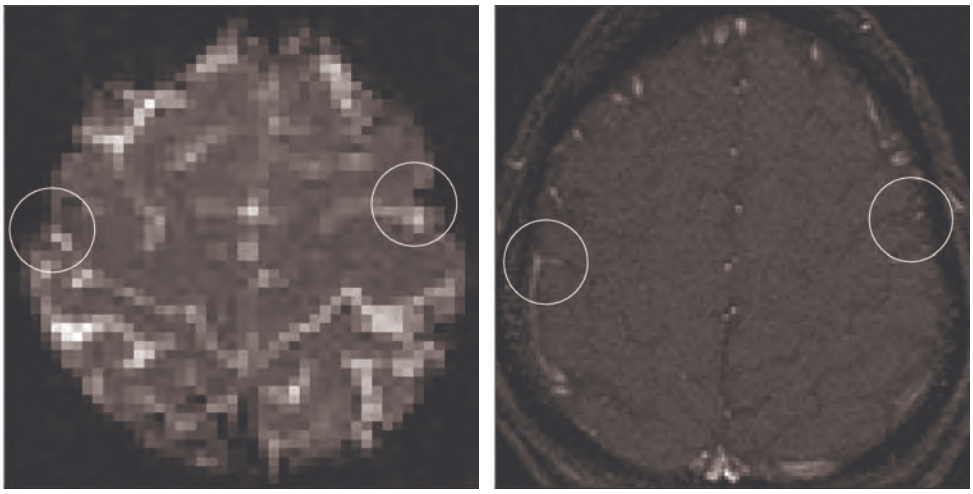

(c) Venous Slice Anatomical (d) Venous Slice Angiogram

Figure 2.6: The anatomical underlays for the representative parenchymal and venous slices shown in Fig. 2.5 are shown here in (a) and (c). The corresponding time of flight angiograms from those slices are shown in (b) and (d). The vasculature is imaged as hyper-intense in the angiogram, and it is apparent that the venous slice activations are co-localized with the imaged vasculature while the parenchymal slice activations are not. The locations of probable active veins are circled in (c) and (d).

in Fig. 2.5(f), significant TRPCs are observed in the MO active voxels with large TRPCs in the suspected draining veins. The constant phase method thus biases against the voxels with TRPCs as shown in the simulation. Voxels with large TRPCs coupled with large CNRs are found to be active while voxels with smaller CNRs are eliminated. This bias is likely the result of the observed TRPCs from the draining veins and, as in the parenchymal case, other unmodeled temporal phase variation.

The phase regressor activations in the parenchymal slice are shown in Fig. 2.5(d). These activations correlate quite well with the magnitude-only activations in the parenchymal slice. This is consistent with an ideal method designed to reduce draining vein contributions as the parenchymal slice activations are not eliminated. The statistical significance of the parenchymal slice activations is generally lower than found with the magnitude-only method, likely because of the sub-threshold TRPCs observed in these voxels. Thus, with sub-threshold TRPCs, the phase regressor activations in real parenchymal data are consistent with the simulated activations.

Venous slice activations found with the phase regressor method are shown in Fig. 2.5(h). These activations include several unexpectedly located activations which are not present in the magnitude-only or complex constant phase activations. These several unexpectedly located phase regressor activations throughout the brain result from errors in the regression of the magnitude as a function of phase when significant TRPCs are present. This is also seen in the simulation in Fig. 2.3(f) where the phase regressor method over compensates for the positive correlation with task in the phase data in several voxels to yield unexpected negative phase regressor activations. In this experimental data, many voxels with negatively correlated task related phase changes

	% Voxels also MO Active		
	All Slices	Parenchymal Slices	Venous Slices
CP	85.6%	86.8%	88.8%
PR	31.7%	36.8%	37.8%
	% Voxels also PO Active		
	All Slices	Parenchymal Slices	Venous Slices
CP	15.7%	14.8%	20.4%
PR	42.6%	34.3%	40.1%

Table 2.1: Percentage of constant phase and phase regressor activations which are also magnitude only and phase only activations.

are found to have positive phase regressor activations as the simulation predicts. Thus, the confounding factors in the phase data which lead to unexpectedly located phase-only activations propagate into the phase regressor activations. This is clearly not a property which an ideal method for eliminating draining vein activations would exhibit.

The trends illustrated in the above representative data set extend through all subjects as shown in Table 2.1 which consolidates the data from all subjects. It is apparent that most of the constant phase activations are also magnitude-only activations. Fewer of the phase regressor activations are also magnitude-only activations as the problem of false positives arising from the problematic fit of magnitude as a function of phase. As both methods are argued to reduce magnitude-only activations by biasing against voxels with task related phase changes, the constant phase method favorably finds a subset of the magnitude-only activations to be above threshold, while the phase regressor method appears to have an increased rate of false positives.

Further illustrating the problem of the phase regressor statistical method failing when significant TRPCs are present, the median phase-only activation statistic for

the phase regressor active voxels is 4.62. This is significant with a relatively strong Bonferroni adjusted $\alpha = 0.10$ threshold. The complex constant phase statistical model, which consistently exhibits a bias against voxels with large TRPCs in both the simulated and real data, however, has a median phase-only activation statistic of 1.95 in its active voxels. This is not significant with a weak, uncorrected $\alpha = 0.05$ threshold. Based only upon this, the complex constant phase statistical method appears more favorable.

However, the complex constant phase method is relatively conservative and finds a small subset of the magnitude-only activations to be active. Only 18.1% of the magnitude-only activations in all slices are also constant phase activations (14.5% in parenchymal slices and 22.7% in venous slices). In all cases, significant non-task related phase changes in the real data challenge the complex constant phase model's assumption of constant phase, leading to reduced activation statistics. Only when large CNRs are present does the complex constant phase method find activations. Such CNRs are present in highly active cortex and delocalized veins with large TRPCs. As shown in the simulation, voxels with large TRPCs and large CNRs are not eliminated by the complex constant phase statistical method. It is the coupling of large TRPCs with large CNRs that leads to the increase of correspondence between the magnitude-only and complex constant phase activations in the venous slices.

The phase regressor method finds a higher percentage of the magnitude-only activations. In all slices, 56.1% of the magnitude-only activations are also phase regressor activations. In parenchymal slices 59.9% of the magnitude-only activations are found, while 55.7% of the venous slice magnitude-only activations are active through the

phase regressor method. This, of course, is tempered by the tremendous number of phase regressor activations which are not also magnitude-only activations.

2.5 Discussion and Conclusion

The data presented in this chapter raises challenges to the applicability of statistical activation methods which reduce draining vein contributions to real data. Simulations have revealed the vulnerability of the phase regressor statistical method to slight errors in the estimates of the baseline magnitude and phase variance in the regression of magnitude as a function of phase. This leads to over correction of the magnitude data when large task related phase changes are present in the data. This problem was illustrated in both simulated and real data with the presence of apparent false positives.

A current challenge of the complex constant phase method was also illustrated in the presented experimental data. As the method relies upon a reduced fit of the data to the constant phase model to eliminate draining vein activations, the complex constant phase statistical method also biases against voxels with non-task related phase instabilities in current real data and unshown simulations. This problem was illustrated in the real data in this chapter with the reduction of activations in parenchymal data with sub-threshold task related phase changes.

Modifications to the implementations or data collection methods for both the phase regressor statistical method and the complex constant phase statistical method might need to be made for either to reliably bias only against voxels with task related phase changes. Because the variance in the magnitude data is generally expected to be far greater than the variance in the phase data, an implementation of the phase

regressor method assuming error only in the magnitude values is reasonable. Such unpublished implementations exist and preliminary investigations show that they reduce the false positives observed in this study. Further work needs to be done to evaluate different methods for computing the regression of magnitude as a function of phase in an attempt to reduce the vulnerability to over corrections.

The complex constant phase statistical method relies upon data with a relatively temporally constant phase, and further work needs to be done to ensure the temporal stability of the global phase signal. This includes either filtering the acquired phase signal to remove non-task related temporal variations, or collecting data with more temporally stable phase time series. The latter includes the acquisition of dynamic B-field maps with each TR to correct for global phase changes [Roopchansingh et al., 2003], the acquisition of smaller voxels where less dephasing can occur, and the reduction of TE to reduce the time for disparate phases to accrue. Furthermore, a complex data model which directly models both the magnitude and phase, with a phase reference function accounting for global B-field changes, such as that presented by Rowe [2005a], may yield improved results without the limitations of the constant phase restriction.

Once these models and data acquisition methods are improved to reliably bias against draining veins in simple quadrature-detected data, they could be generalized for use with multi-coil methods which are growing in popularity. Such receive coils can yield different phases for the same spatial locations in the reconstructed images from each channel. These different phases from each of the channels will clearly lead to complications in these statistical methods which utilize phase. Appropriate

consideration for the phase in such multi-channel acquisitions should be examined so that these methods may be expanded to accommodate such data sets.

We have found that data, as traditionally acquired and processed for standard magnitude only fMRI studies contains many phase instabilities which much be addressed for complex data analysis methods to be robustly implemented. These instabilities lead to the generally decreased power of the complex constant phase method. These instabilities may be addressed through the processing of the complex-valued data. Methods must be developed to both process the data to improve the quality of the complex-valued data and evaluate the effects of such processing on computed statistical results.

Chapter 3

Image processing

With the need for processing complex-valued data illustrated in the previous chapter, specifically the need for temporally processing the phase signal to remove global, non-task related phase fluctuations, we have developed a linear framework to both process complex-valued data and include the effects of processing complex-valued data in applied statistical models. This chapter and the following chapter define the mathematical framework and offer analytical and experimental results to verify the framework. In this chapter, we specifically consider spatial processing of the data. The assumption is made that identical spatial processes will be applied to every image in an acquired time series. We develop linear operators for processes to censor and reorder acquired echo planar imaging (EPI) data, apply corrections for artifacts which cause Nyquist ghosts, calculate the effects of intra-acquisition decay and magnetic field inhomogeneity, apply shifts and rotations to acquired images, apodize k-space data, perform Fourier reconstruction, and apply image-space convolution. With the developed operators, we computationally determine the effects of the processes on

the mean, covariance, and correlation structure of ideal, uncorrelated data. Some processes are shown to introduce spatial correlation into ideally uncorrelated data. Furthermore, multiple serial processes are shown to alter spatial covariance and correlation in ways that are not the simple summation of the effects of each process. The developed framework also provides the opportunity to consider acquisition parameters which would yield optimal covariances in acquired data when given reasonable approximations for the physical properties of the system being imaged.

3.1 Introduction

Magnetic field gradients can be used in magnetic resonance imaging to encode the measured signal as a linear transformation of the object being imaged. An inverse transform is then applied to the acquired signal to reconstruct an image of the object. As the encoding and reconstruction are linear transformations, they can be considered through the constructs of linear algebra as multiplications of matrices upon vectors representing either the physical object or the acquired signal. Rowe et al. [2007b] have recently published a description of this mathematical formalism, using Fourier encoding and reconstruction as a specific example. In the case of Fourier encoding, the acquired data is in the spatial frequency space, k-space, and it is reconstructed through the inverse Fourier transform to image-space. In addition to describing the mathematical formalism of image reconstruction, the work also illustrated that, because of the linear properties of the reconstruction, correlated observations in k-space lead to correlated volume elements, or voxels, in the reconstructed image.

Correlated voxels, which necessarily arise from correlated k-space measurements, are the basis of functional connectivity studies [Biswal et al., 1995]. These connectivity

studies determine voxels to be connected if their time series exhibit high correlations. Common techniques, including cross correlation analysis, principle component analysis (PCA), and independent component analysis (ICA), have been used to determine regions with high correlations in their time series [Biswal et al., 1995, Friston et al., 1993, van de Ven et al., 2004]. Regardless of the analysis method, voxel correlation, and thus k-space correlation, affect the measured voxel connectivity.

The low temporal frequency physiologic processes upon which functional connectivity studies rely are clearly not the only sources of voxel correlation. Global signal fluctuation may arise from physiologic processes [Glover et al., 2000, Pfeuffer et al., 2002, Birn et al., 2006, Shmueli et al., 2007]. As described by Rowe et al. [2007b], temporal autocorrelation in the acquired signal also may lead to image-space voxel correlation. Artifactual time series correlations have also been observed in inanimate phantom studies [Kriegeskorte et al., In Press]. Additionally, as this chapter describes, operations on k-space data before reconstruction and image space data after reconstruction can produce correlations in voxels. Sequences of spatially correlated images lead to temporally correlated time series. Clearly one must be mindful of the effects of such operations when drawing conclusions from functional connectivity (fcMRI) and functional (fMRI) data.

In this chapter we consider several operations. These include: Fourier encoding anomalies, k-space observation censoring, k-space line shifting, symmetric k-space generation, and smoothing through k-space windowing, zero filling, and image-space convolution. We first develop linear operators for the mentioned operations and show toy examples of each using an 8×8 data set. We then utilize the operators to

theoretically examine image-space correlations associated with the operators under more relevant parametrizations, including 96×96 data acquisition arrays. Finally we illustrate the results of the operations in acquired 96×96 phantom data.

3.2 Theory

3.2.1 Operator Development

In this section we extend the mathematical formalism of image reconstruction presented by Rowe et al. [2007b] to a more general case. We describe Cartesian Fourier reconstruction for the sake of demonstration, although the mathematics hold true for any linear reconstruction operator. Other linear operators may include regridding operators for non-Cartesian k-space sampling methods. First we further extend the previously published statistical model to include the data as it is ideally collected. This includes modeling the points acquired during the phase encoding blips of echo planar imaging (EPI), and the reversal of lines acquired with negative frequency encoding gradients. We describe models of Fourier encoding anomalies, k-space line shifting, symmetric k-space generation, zero filling, and multiplication of the k-space observations with a windowing function in light of the extended statistical model.

Rowe et al. [2007b] have described complex-valued Fourier reconstruction through a real-valued isomorphism such that a vector of the reconstructed image, y, is the product of a Fourier reconstruction operator,Ω , with a vector of the observed k-space observations, s:

$$y = \Omega s. \tag{3.1}$$

In the above equation, if the reconstructed image is m rows by n columns, y is a vector with mn real image values stacked above mn imaginary image values, Ω is a reconstruction operator array with dimensions of $2mn \times 2mn$, and s is a vector of mn appropriately ordered real Cartesian k-space observations stacked above mn imaginary Cartesian k-space observations. The Cartesian Fourier reconstruction operator may be written as

$$\Omega = \begin{pmatrix} \Re(\Omega_C) & -\Im(\Omega_C) \\ \Im(\Omega_C) & \Re(\Omega_C) \end{pmatrix}, \tag{3.2}$$

where $\Re(\cdot)$ and $\Im(\cdot)$ take the real and imaginary parts of the arguments respectively, andΩ_C is the Kronecker product of two matrices,Ω_x andΩ_y, which Fourier transform the columns and rows of the acquired k-space, respectively,

$$\Omega_C = \Omega_x \otimes \Omega_y.$$

The Kronecker product, denoted by $\otimes$, multiplies each element of the first matrix by the entire second matrix. The jk^{th} element ofΩ_x, where j and k are indices from 0 to $n-1$, may be written as

$$(\Omega_x)_{jk} = w^{\left(-\frac{n}{2}+j\right)\left(-\frac{n}{2}+k\right)},$$

where $w = \frac{1}{n}e^{\frac{i2\pi}{n}}$ for the inverse Fourier transform and $w = e^{\frac{-i2\pi}{n}}$ for the forward Fourier transform. A similar matrix of dimension m exists forΩ_y.

Under the formalism of Equation 3.1, if the k-space observations have a covariance matrix of $\mathrm{cov}(s) = \Gamma_0$, the resulting reconstructed image-space values have a covari-

ance matrix of$\Omega\Gamma\ {}_0\Omega^T$, where T denotes transposition. Here we develop operators, O, such that the acquired signal, $\mathcal{S}$, may be processed as desired and transformed to image-space. It is helpful to note that s represents the properly ordered k-space data while $\mathcal{S}$ represents the real/imaginary k-space observation pairs acquired along the k-space trajectory, including points acquired during echo planar imaging phase encoding blips. With such operators developed, the original reconstruction relationship shown in Equation 3.1 may be more appropriately modeled as

$$y = O\mathcal{S}, \tag{3.3}$$

with a covariance matrix resulting from the k-space covariance matrix,Γ , calculated as

$$\text{cov}(y) = O\Gamma O^T. \tag{3.4}$$

In light of the new parameterization, if the originally collected k-space data, $\mathcal{S}$, has mean of $\mathcal{S}_0$, the final reconstructed complex-valued image, y, has a mean of $O\mathcal{S}_0$ and a covariance matrix as shown above.

The covariance structure of the square of the magnitude data may be derived from this complex data covariance matrix. The covariance matrix for the square of the magnitude data is considered as an analytical solution exists in the described linear framework. The magnitude operation, being non-linear in nature, does not extend well to the described framework. Nevertheless, it can be shown that the magnitude squared covariance asymptotically approaches the magnitude covariance. It will be seen that the magnitude squared correlation structure, which is asymptotically equal

to the magnitude data correlation structure, is generally found to exhibit similar properties to the real and imaginary correlation structures. A brief derivation of the magnitude squared covariance matrix is included in Appendix C.

In light of this framework, the effects of several processing techniques will be considered. The mean, covariance, and correlations will be computed for each operation on the complex and magnitude squared data. A brief description of each operator follows, with expanded descriptions of their compositions included in the appendices.

Anomalies in Fourier Encoding

The k-space observation process is often assumed to be instantaneous at the echo time, TE [Haacke et al., 1999]. Under that assumption, and assuming an exponential intra-acquisiton decay map of $T_2^*(x,y)$ and magnetic field inhomogeneity map of $\Delta B(x,y)$, the acquired k-space signal is

$$s(k_x,k_y)=\int_{-\infty}^{\infty}\int_{-\infty}^{\infty}\rho(x,y)e^{-TE/T_2^*(x,y)}e^{i\gamma\Delta B(x,y)TE}e^{-i2\pi(k_xx+k_yy)}\mathrm{d}x\mathrm{d}y, \tag{3.5}$$

where γ is the proton gyromagnetic ratio and ρ is the proton spin density. The k-space points are defined by the temporal integral of the applied magnetic field gradients applied along the appropriate directions:

$$k_x=\frac{\gamma}{2\pi}\int_0^t G_x(t')\mathrm{d}t', \qquad k_y=\frac{\gamma}{2\pi}\int_0^t G_y(t')\mathrm{d}t'.$$

Thus, the observed k-space data, encoded in time, is assumed to be the Fourier transform of the proton spin density weighted by the intra-acquisition decay and

with a phase determined by the magnetic field inhomogeneity. The image-space representation may then be recovered with an inverse Fourier transform. An image of the ideal 128×128 Fourier,Ω , operator, described above and in Rowe et al. [2007b], for an 8×8 image array toy example is shown in Figure 3.1(a). Each column of this operator corresponds to either the real or imaginary part of a voxel of the original 8×8 image array, and each row corresponds to either the real or imaginary part of a voxel of the processed image array. This operator is described as ideal as it does not account for T_2^* orΔ B effects.

However, as the definition of k-space locations suggests, the k-space observation process occurs over a finite duration of time, with each k-space measurement being sampled at a unique time point. Thus, the k-space signal equation may be more appropriately considered as

$$s(k_x, k_y|t) = \int_{-\infty}^{\infty} \int_{-\infty}^{\infty} \rho(x, y) e^{-t/T_2^*(x,y)} e^{i\gamma \Delta B(x,y) t} e^{-i2\pi(k_x x + k_y y)} \mathrm{d}x\mathrm{d}y, \tag{3.6}$$

when the k-space point (k_x, k_y) is sampled at time $t = t(k_x, k_y)$. With the $t(k_x, k_y)$ variable changing for each k-space measurement, image blurring from intra-acquisiton decay and image warping from magnetic field inhomogeneities may occur [Jesmanowicz et al., 1998, Jezzard and Balaban, 1995]. Thus, the Fourier transform operator developed by Rowe et al. [2007b] may be modified to account for non-instantaneous k-space observation in a modified Fourier operator,Ω $_a$. Each row of the operator is modified with exponential terms for $T_2^*(x, y)$ andΔ $B(x, y)$ as described in Appendix D.

The inclusions of these parameters finely alter the structure of Ω to arrive at

Ω_a. Two examples ofΩ_a are shown in Figures 3.1(b) and 3.1(c). Figure 3.1(b) illustrates a Fourier matrix that accounts for a spatially uniform T_2^* decay. The element values tend toward zero in the later portion ofΩ_a because of the exponential decay. Figure 3.1(c) illustrates a Fourier matrix that accounts for a magnetic field gradient in the frequency encoding direction. This array is clearly different from the ideal Fourier array in Figure 3.1(a) and the array including decay in Figure 3.1(b). This Fourier array is essentially a skewed version of the ideal array. In both the cases of intra-acquisition decay and magnetic field inhomogeneity, an external measure of the perturber must be utilized. A $T_2^*(x, y)$ map may be acquired through the consideration of the magnitude of separate scans with varying echo times, and the $\Delta B(x, y)$ map may be acquired through the consideration of the phase of separate scans with varying echo times.

Obtaining s from $\mathcal{S}$

In Equation 3.1, s is assumed to include only the properly ordered k-space observations located on the Cartesian k-space grid. However, as the k-space data is acquired in echo planar imaging (EPI), this is not true of the collected signal. Rather, the collected k-space data, $\mathcal{S}$, is observed as real-imaginary pairs throughout the k-space traversal defined by the pulse sequence. Thus, in addition to including point-wise real-imaginary pairs instead of a column of real observations above a column of imaginary observations, the acquired data includes e extra points acquired during the phase encoding blips and incorrectly ordered observations from the negative frequency encoding lines in echo planar imaging. If the acquired k-space point at row r and column c on the desired k-space grid is denoted as $s_{r,c,R/I}$, where the final R/I index indi-

cates that the observation is real or imaginary, and the extra k-space points acquired during the phase encoding blips are denoted as $E_{r,ep,R/I}$, with ep indexing the extra point number, the actually acquired data is the long vector

$$\mathcal{S} = [s_{1,1,R}, s_{1,1,I}, \ldots, s_{1,n,I}, E_{1,1,R}, \ldots, E_{1,e,I}, s_{2,n,R}, s_{2,n,I}, s_{2,n-1,R}, \ldots, E_{m,e,I}]'.$$

However, the data required for the reconstruction in Equation 3.1 is

$$s = [s_{1,1,R}, s_{1,2,R}, \ldots, s_{m,n,R}, s_{1,1,I}, \ldots, s_{m,n,I}]'.$$

Therefore, points in $\mathcal{S}$ must be censored and its component lines reordered to produce the s required in Equation 3.1. This can be performed in the three steps of censoring extra points, reversing alternating lines, and segregating real and imaginary observations. Censoring may be performed with a censoring matrix, C, row reversal may be performed with a permutation matrix, R, and the separation of real and imaginary data may be performed with another permutation matrix, P_C. The construction of these operators is discussed in Appendix E, and the operators are shown in Figures 3.1(d), 3.1(e), and 3.1(f), respectively.

Thus, the process of converting the acquired data to the required data for Equation 3.1 may be considered as

$$s = P_C R C \mathcal{S}. \tag{3.7}$$

As the operators in Equation 3.7 are censoring and permutation matrices, considering their effects on uncorrelated k-space observations is trivial. In the case of uncorrelated

k-space observations, $\Gamma = \ I_{m(n+e)}$. The covariance between the processed k-space observations,$\Gamma_{\ P_cRC}$, is

$$\begin{aligned} \Gamma_{P_CRC} &= P_CRCI_{m(n+e)}C^TR^TP_C^T \\ \Gamma_{P_CRC} &= I_{mn}. \end{aligned}$$

Thus, the processes of censoring, reversing, and permuting uncorrelated k-space observations does not yield correlated k-space values as it can be shown that $CC^T = I$, $RR^T = I$ and $P_CP_C^T = I$. However, if identity k-space covariance matrix Γ is not assumed, these processes will alter the covariance.

Line Shifting

Unmodeled gradient timing errors and eddy current effects may cause alternating k-space lines to be shifted in EPI acquisitions [Haacke et al., 1999]. This shifting results in the N/2 or Nyquist ghost artifact associated with EPI. An offset term is introduced in the signal equation,

$$s(k_x, k_y|t) = \int\int \rho(x,y)e^{-t/T_2^*(x,y)-i\gamma\Delta B(x,y)t+i(-1)^\ell 2\pi\Delta k_x x}e^{-i2\pi(k_x x+k_y y)}\mathrm{d}x\mathrm{d}y \quad (3.8)$$

where$\Delta\ k_x$ is the effective eddy current k-space shift and ℓ is the frequency encoding line number in Equation 3.8. These shifts can be estimated and corrected to reduce such artifacts in the reconstructed images. Such shifts are often determined through the use of navigator echoes [Jesmanowicz et al., 1993] or reference scans [Bernstein et al., 2004]. Thus, opposite shifts are then applied to the acquired k-space lines to

realign them. The application of these shifts involves the use of the Fourier shift theorem. Each line is Fourier transformed, multiplied by a complex-valued exponential, and then inverse Fourier transformed to the shifted state. Thus, the process of shifting the k-space lines can be considered in several steps: The vector s is re-ordered to group real and imaginary observations from each line together; The lines are Fourier transformed; The transformed lines are multiplied by a complex-valued exponential; The phase altered lines are inverse Fourier transformed into shifted lines; The shifted lines are re-ordered to the original ordering of s. Thus, three operators need to be constructed: a permutation operator, P_R, to convert from s with the reals for the image stacked above the imaginaries for the image to a vector of reals stacked above imaginaries for each row; a row Fourier transform operator,Ω_{row}, to transform each of the rows; and a phase shift operator,Φ , to alter the phase of the transformed rows. Additionally, inverses of the permutation operator, trivially $P_R^{-1} = P_R^T$, and Fourier transform operator,Ω_{row}^{-1}, are needed. The details of these three operators are given in Appendix F, and image representations of them are shown in Figures 3.1(g), 3.1(h), and 3.1(i).

With the permutation, Fourier transform and phase shift operators defined, shifting the acquired k-space lines alternating directions to yield a corrected set of k-space observations simply involves linear algebra:

$$s_{corrected} = P_R^{-1}\ \Omega_{row}^{-1}\ \Phi\ \Omega_{row}\ P_R\ s. \tag{3.9}$$

Thus, when performed on a time series of images, the reconstructed mean and co-

variance are altered by the processes in Equation 3.9 to

$$\mathrm{E}(y) = \Omega\ P_R^{-1}\ \Omega_{row}^{-1}\ \Phi\ \Omega_{row}\ P_R\ s_0 \tag{3.10}$$

and

$$\mathrm{cov}(y) = \left(\Omega\ P_R^{-1}\ \Omega_{row}^{-1}\ \Phi\ \Omega_{row}\ P_R\right) \Gamma \left(P_R^{-1}\ \Omega_{row}^{T}\ \Phi^T\ (\Omega_{row}^{-1})^T\ P_R \Omega^T\right), \tag{3.11}$$

where $s_0 = E(s)$ in Equation 3.10 is the mean k-space observation vector and$\Gamma_{\ 0} = \mathrm{cov}(s)$ in Equation 3.11 is the mean k-space covariance matrix. It should be once again noted that if $\Gamma = I$, then

$$\left(\Omega\ P_R^{-1}\ \Omega_{row}^{-1}\ \Phi\ \Omega_{row}\ P_R\right) \left(P_R^{T}\ \Omega_{row}^{T}\ \Phi^T\ (\Omega_{row}^{-1})^T\ (P_R^{-1})^T\ \Omega^T\right) = I \tag{3.12}$$

because it can be shown that each of the operators in Equation 3.12 multiplied by their transposes yield identity matrices. If$\Gamma \neq I$, the mean, covariance, and correlation will be altered by the operations, leading to the correlation of a voxel with its ghost location.

Symmetric k-space Generation

Symmetric k-space generation relies upon the symmetry of k-space about the origin under complex conjugation when a real-valued object is imaged. This symmetric generation has been used in partial Fourier acquisitions [Jesmanowicz et al., 1998]. In the simplest case the first $m/2 + 1$ lines of k-space are acquired and the final $m/2 - 1$ lines are generated through the symmetry relationship. The partial Fourier

interpolation matrix, H, is described in Appendix G. A graphical representation of H is shown in Figure 3.1(j) for the case of an 8×8 symmetric k-space generation from a 5×8 k-space acquistion.

With this partial Fourier reconstruction matrix, the omitted data is generated using the k-space symmetry relationship with the matrix multiplication $s_S = H\ s$. In the event of a full k-space acquisition, no symmetric data need be generated and $H = I$. Effects of partial Fourier processing on a data set may be considered with the modified reconstructed mean and covariance being

$$\mathrm{E}(y) = \Omega\ H s_0$$

and

$$\mathrm{cov}(y) = \Omega\ H \Gamma_0 H^T \Omega^T. \tag{3.13}$$

Note that $HH^T \neq I$ when a partial k-space acquisition is made. It is seen that partial k-space reconstruction necessarily requires k-space observations to be correlated. Therefore, as the process of reconstruction is linear, image-space observations must exhibit a correlation. Thus, the operator modifies the covariance and correlation. Of course, the reconstruction of an image with fewer points in partial Fourier reconstruction additionally yields increased variance.

Smoothing with k-space Windowing and Image-Space Convolution

Smoothing of the complex-valued data may be performed during apodization, zero-filling, or explicit image smoothing operations. The Fourier convolution theorem allows complex-valued image-space convolution to be considered with k-space

windowing. Thus, zero-filling, k-space apodization, and image-space complex data smoothing may be considered with operators of the same form. Because of the image-space convolution associated with these processes, it is obvious that they have a non-negligible effect on image-space voxel correlations. In Appendix H, we describe a zero filling operator, F, and an apodization operator, A. The apodization operator may include any windowing function, including the usual Fermi, Tukey, Hanning or Gaussian apodization windows. In Appendix H, we also describe an operator, S_m, which may be implemented on magnitude or magnitude squared data to yield image-space smoothing. The zero-filling operator is shown in Figure 3.1(k), the apodization operator in Figure 3.1(l), and the image-space magnitude smoothing operator in 3.1(m).

As it is well known, convolution alters the image mean, covariance, and correlation. Thus, even if $\Gamma = I$, the application of these operators alters the data as it will be shown.

3.3 Operator Implementation

With the above linear operators defined, it is possible to mathematically determine the image-space correlations resulting from applying the operators to k-space data with a covariance matrix, $\mathrm{cov}(\mathcal{S}) = \Gamma$. The image space covariance, $\mathrm{cov}(y)$, after applying an operator, O, to k-space data with a covariance matrix of Γ is defined in Equation 3.4.

Without loss of generality, we describe here the case of applying the operators to uncorrelated k-space data. Thus, Γ is assumed to be the identity matrix. Therefore, Equation 3.4 simplifies to $\mathrm{cov}(y) = OO^T$. It is clear from this that if $OO^T = \delta^2 I$, where $\delta^2 = 1/(m^2n^2)$ is a scalar introduced by the inverse Fourier transform, then

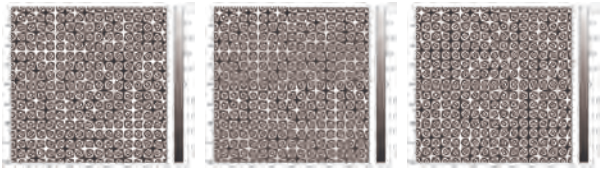

(a) Fourier,Ω (b) Uniform T_2^* Fourier,Ω_a (c) B_0 Gradient Fourier,Ω_a

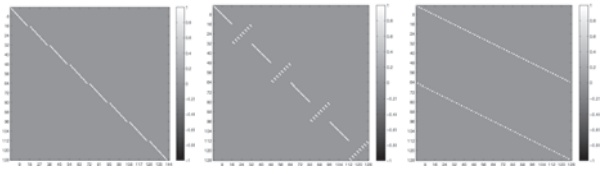

(d) Censoring, C (e) Row Reversal, $\mathcal{R}$ (f) Complex Permutation, P_C

(g) Row Permutation, P_R (h) Row Fourier,Ω_{row} (i) Phase Shift, Φ

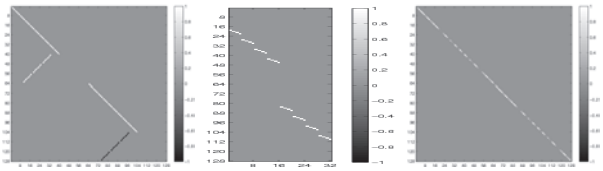

(j) Partial Fourier, H (k) Zero Filling, F (l) Apodization, A

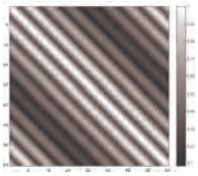

(m) Magnitude Smoothing, S_{mm}

Figure 3.1: Toy example operators.

the resulting image-space observations have scaled identity covariance matrices. With the covariance matrix known, the correlation matrix may be exactly calculated as

$$\mathrm{cor}(y) = D^{-1/2}\mathrm{cov}(y)D^{-1/2}, \tag{3.14}$$

where $D = \mathrm{diag}(\mathrm{cov}(y))$.

As it was mentioned in the description of the operators, the censoring of the k-space observations, row reversal, reordering, and line shifting operators yield no image-space correlations in uncorrelated k-space data as in each case the operator multiplied by its transpose results in an identity matrix. If the k-space covariance matrix is not the identity, the operators will modify the covariance and correlation. More interesting results follow from the application of the operators including anomalies in the Fourier encoding process, partial Fourier reconstruction and k-space windowing or image-space convolution. In the following sections we consider these operators individually and serially in the case of a 96×96 data acquisition.

In the following calculations, physical parameters similar to those in typical fMRI studies were considered. The maps of the physical parameters and apodizers considered are shown in Figure 3.2. The proton spin density, ρ shown in Figure 3.2(a), was assumed to be zero outside of the phantom, and unity within the phantom. The intra-acquisition decay, T_2^* shown in Figure 3.2(b), was considered as a modified Shepp-Logan phantom which was scaled to physically relevant values from 10 to 100 ms. The B field inhomogeneity was considered as a horizontal gradient from 0 to 2.5×10^{-6} T, as shown in Figure 3.2(c). This B field inhomogeneity is significant, but on the order of the inhomogeneity observed in the inferior frontal lobe. The

timing of the k-space observations is shown in Figure 3.2(d), and is representative of a standard EPI pulse sequence with an acquisition matrix of 96×96, bandwidth of 250 kHz, effective echo spacing of 0.96 ms, and echo time of 50 ms. The considered k-space apodization filter, shown in Figure 3.2(e), is a Gaussian window with an image-space representation shown in Figure 3.2(f). The image-space representation has a full width at half maximum of 3 pixels. Partial Fourier reconstruction was considered with 16 overscan lines. When the processes were not considered in the following calculations the parameters for the unconsidered processes are equivalent to: T_2^* as a uniform, infinite map;Δ B as a map of zeroes; and the apodization window as a map of ones.

Calculations were made to examine the intra-acquisition decay, B field inhomogeneity, partial Fourier interpolation, and k-space apodization operators individually. Additionally, the combination of intra-acquisition decay, partial Fourier interpolation and k-space apodization performed serially was evaluated. Results illustrating the processed image means are shown in Figure 3.3, and the correlations for the center pixel in the processed images with all other pixels are shown in Figure 3.4. The first and second columns of Figure 3.3 illustrates the mean magnitude and phase images, while the third and fourth columns respectively illustrate the mean real and imaginary images. Each row of Figure 3.3 illustrates the results on the mean image in light of a different processing pipeline. Figure 3.4 illustrates the correlations for the center pixel for the same processing cases. Additionally, correlation coefficients for the four neighbors of the center pixel are shown in Table 3.1 for several processing pipelines.

3.3.1 Fourier Anomalies

As it has previously been described, intra-acquisition decay yields an increase in the point spread function in the phase encoding direction [Jesmanowicz et al., 1998]. The increase in the point spread function occurs preferentially in the phase encoding direction because of the decreased effective bandwidth in this direction in EPI. This can be seen through the apparent blurring of the edges of the phantom in the magnitude and real images in Figures 3.3(a) and 3.3(c). Nevertheless, slight correlation is noted between voxels in the frequency encoding direction as well in Table 3.1 due to the non-instantaneous acquisition of each k-space line. These correlations are dramatically less in the frequency encoding direction than in the phase encoding direction because of the remarkably higher bandwidth in the frequency encoding direction. Additionally, intra-acquisition decay leads to the appearance of edges in the mean phase and imaginary image in Figures 3.3(b) and 3.3(d). The increased point spread function in the phase encoding direction is clear in the correlation maps in Figures 3.4(a), 3.4(b), 3.4(c), and 3.4(d). The magnitude squared point spread function is less than the real and imaginary point spread functions. Moderate correlation between the real and imaginary data was observed along the phase encoding direction. The observation of the reduced magnitude squared point spread function holds true for each of the considered processing pipelines.

Also as previously described, static B field inhomogeneities lead to image warping and phase generation [Jezzard and Balaban, 1995]. Thus, warping and a bulk shift in the phase encoding direction is apparent in the mean images that include B field inhomogeneities in the Fourier operators in Figures 3.3(e), 3.3(f), 3.3(g), and 3.3(h).

More minor sub-voxel warping also occurs in the frequency encoding direction because of the higher sampling bandwidth in that direction. The phantom appears warped but uniform in Figure 3.3(e) as the magnitude data does not contain phase information, while the horizontally varying phase information is apparent in the phase, real and imaginary data in Figures 3.3(f), 3.3(g) and 3.3(h). Very small correlations are seen from the B field inhomogeneity in Figures 3.4(e), 3.4(f), 3.4(g), and 3.4(h). In fact, as seen in Table 3.1, higher correlation coefficients are observed in the frequency encoding direction than in the phase encoding direction. Such an observation may corroborate the observations of Kriegeskorte et al. [In Press] where correlations in the frequency encoding direction appear to dominate. In this framework with uncorrelated data, B field inhomogeneities do not significantly alter observed variances.

3.3.2 Partial Fourier Reconstruction

In the ideal calculated case, partial Fourier reconstruction does not visually alter the mean reconstructed images in Figures 3.3(i), 3.3(j), 3.3(k), and 3.3(l). As expected with partial Fourier reconstruction, no obvious information is introduced into the phase or imaginary data. However, as described above, partial Fourier interpolation does slightly alter the mean image and correlation structure, even in this ideal case. Negligible correlation results between the real and imaginary data as seen in Figure 3.4(l). Figures 3.4(i), 3.4(j), and 3.4(k) illustrate slight correlations in the phase encode direction. Note that these correlations are less than those associated with intra-acquisition decay. In fact, as previously described by Jesmanowicz et al. [1998], when both partial Fourier reconstruction and intra-acquisition decay are considered, reduced correlation along the phase encoding direction is observed when compared

to full Fourier reconstruction in the presence of intra-acquisition decay. Although Table 3.1 shows slight increases in correlation coefficients in neighboring voxels in the phase encoding direction with partial Fourier reconstruction, the effective point spread function in the phase encoding direction is reduced by partial Fourier reconstruction. It should be further noted that non-zero phase, caused by magnetic field inhomogeneities, exists in experimental data and leads to further alterations of the reconstructed mean images. Partial Fourier reconstruction was found to increase variance in the real and magnitude data while decreasing variance in the imaginary data, as expected.

3.3.3 k-space Windowing and Image-Space Convolution

Apodization with a Gaussian window clearly alters the reconstructed image means. The magnitude mean image in Figure 3.3(m) illustrates that the edge of the phantom is blurred and dilated as a result of convolution of the image-space apodization kernel. The real mean image shows the same result in Figure 3.3(o). As there is ideally no data in the imaginary data, apodization does not introduce significant information into the phase and imaginary mean images in Figures 3.3(n) and 3.3(p), although the noise appears to be smoothed. Correlations resulting from apodization, shown in Figures 3.4(m), 3.4(n), 3.4(o) , and 3.4(p), are as expected through the Fourier convolution theorem. Specifically, the image space-correlations resulting from k-space apodization are related to the image-space convolution with the Fourier transform of the k-space apodization window. As convolution with a real valued kernel does not induce correlations between the real and imaginary data, no correlations are seen in Figure 3.4(p). Apodization was found to decrease variance as expected with spatial

smoothing.

3.3.4 Serial Processes

The results of serially considering intra-acquisition decay, partial Fourier reconstruction, and k-space apodization on the mean images are shown in Figures 3.3(q), 3.3(r), 3.3(s), and 3.3(t). The effects of intra-acquisition decay and apodization appear to dominate the reconstructed mean images. However, the computed image-space correlations, shown in Figures 3.4(q), 3.4(r), 3.4(s), and 3.4(t), are not simply the superposition of the correlations associated with each process. In this result, some of the utility of the theoretical framework is illustrated as the result of a series of complicated processing steps may be easily computed. The effects of smoothing from apodization were found to dominate the processed data variance as it was reduced to the level observed with apodization alone.

3.4 Experimental Illustration

To illustrate the performance of the operators, their application to phantom data was considered. Two experimental data sets were considered. The data sets were acquired on a 3.0 T General Electric Signa LX magnetic resonance imager, with a spherical doped agar phantom with $T_2^* = 40.0$ ms as the subject. Each data set consisted of 1024 images of a single 2.5 mm thick, 24.0 cm field of view slice, with a 96×96 acquisition matrix, minimum full k-space echo time of 50.0 ms, effective echo spacing of 0.96 ms, 2000.0 ms repetition time, and 250 kHz acquisition bandwidth. The proton spins were excited with an 80 degree radio frequency pulse in one data set, and with a zero degree radio frequency pulse in the other data set. The data set with no excitation pulse was acquired to match the condition of pure noise considered in some of the above theoretical computations, while the data set with an excitation pulse more closely matches standard acquisitions.

Data were collected with a custom echo planar imaging pulse sequence, and reconstructed with locally developed software. With control of the entire acquisition and reconstruction pipeline, the confounds of unmodeled data processing are reduced. Nevertheless, some temporal filtering of the k-space acquisitions is performed to subsample the acquired 1 GHz samples to the collected 250 kHz samples. This processing may result in an autocorrelation of k-space observations, although such a correlation structure was not observed and is likely obscured by the noise in the experimental data.

Three navigator echoes of the center line of k-space were acquired to estimate error in the center frequency, and group delay offsets between odd and even k-space lines

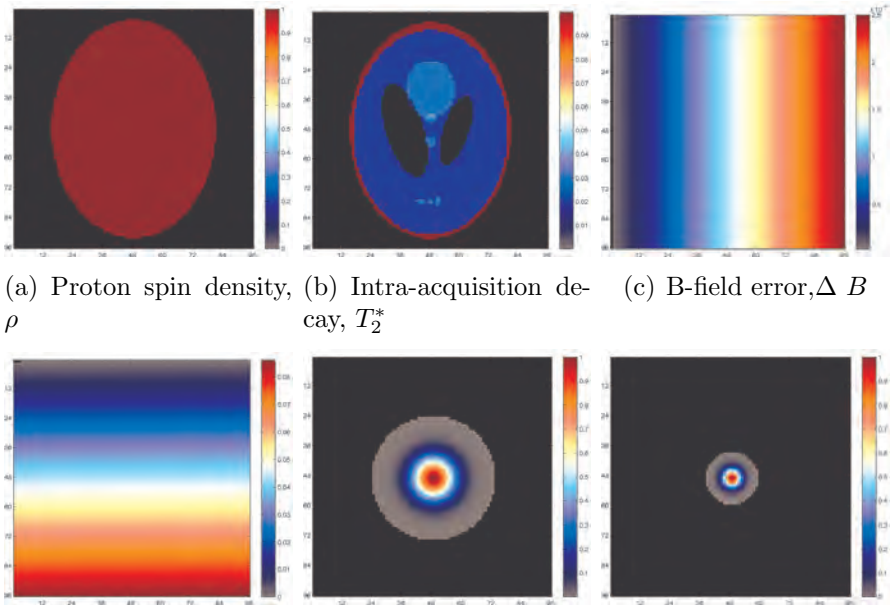

(a) Proton spin density, ρ (b) Intra-acquisition decay, T_2^* (c) B-field error,Δ B

(d) k-space time, t (e) k-space apodization window (f) Image-space apodization window

Figure 3.2: Parameters considered in theoretical calculations.

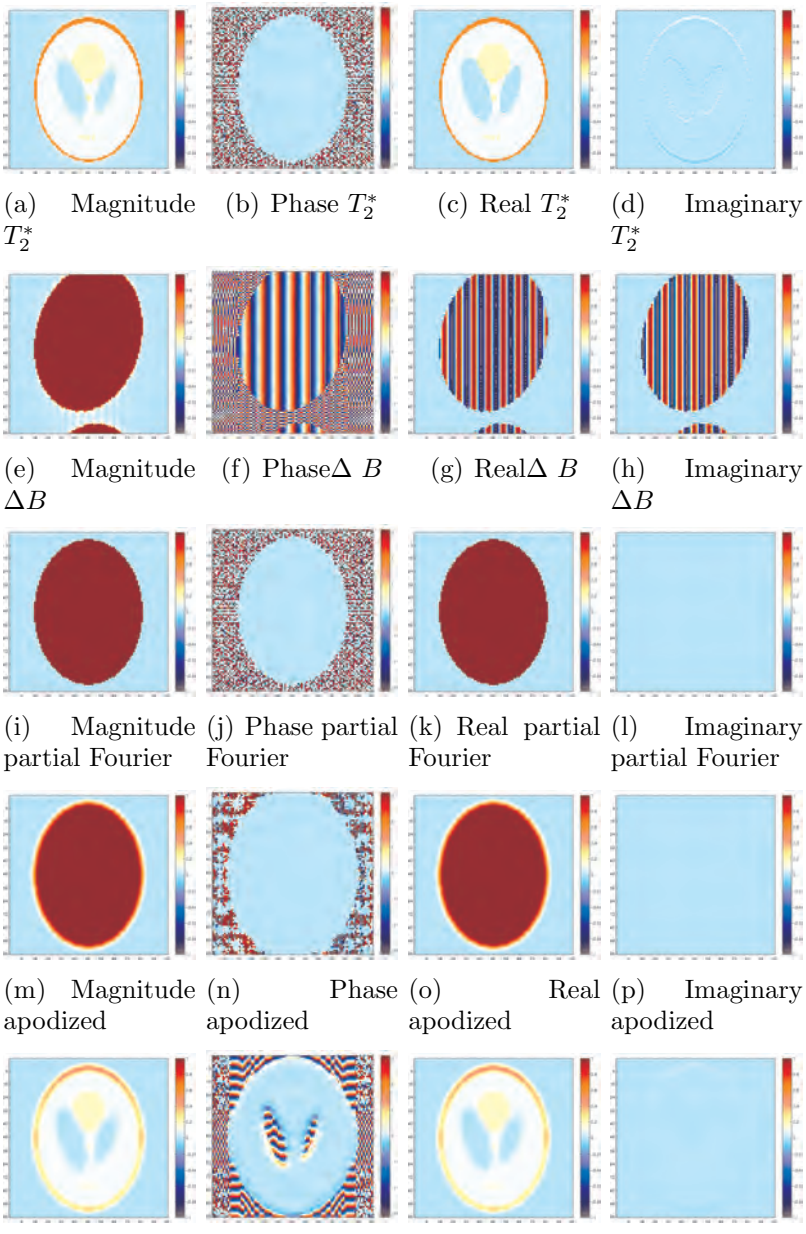

(a) Magnitude T_2^* (b) Phase T_2^* (c) Real T_2^* (d) Imaginary T_2^*

(e) Magnitude ΔB (f) PhaseΔ B (g) RealΔ B (h) Imaginary ΔB

(i) Magnitude partial Fourier (j) Phase partial Fourier (k) Real partial Fourier (l) Imaginary partial Fourier

(m) Magnitude apodized (n) Phase apodized (o) Real apodized (p) Imaginary apodized

(q) Magnitude serial (r) Phase serial (s) Real serial (t) Imaginary serial

Figure 3.3: Reconstructed mean magnitude, phase, real and imaginary signal with various processes included. In each case, only the listed operator was included. In the serial case, T_2^* decay, partial Fourier reconstruction, and k-space apodization were considered.

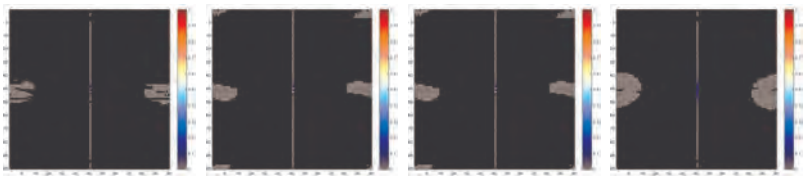

(a) Magnitude T_2^* (b) Real T_2^* (c) Imaginary T_2^* (d) Real / imaginary T_2^*

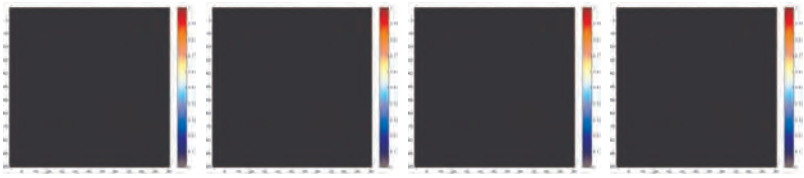

(e) Magnitude ΔB (f) RealΔ B (g) Imaginary ΔB (h) Real / imaginaryΔ B

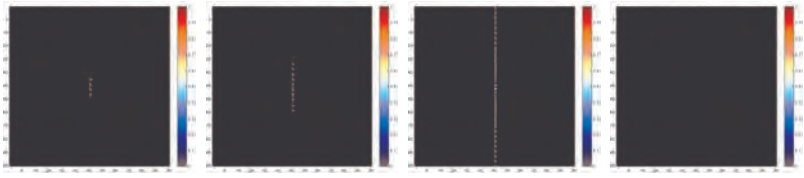

(i) Magnitude partial Fourier (j) Real partial Fourier (k) Imaginary partial Fourier (l) Real / imaginary partial Fourier

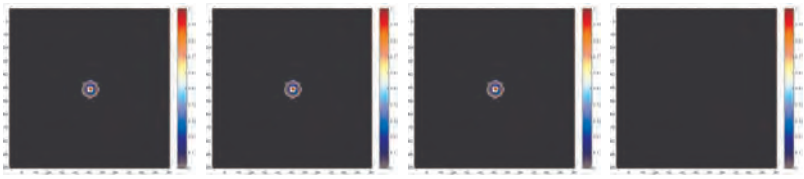

(m) Magnitude apodized (n) Real apodized (o) Imaginary apodized (p) Real / imaginary apodized

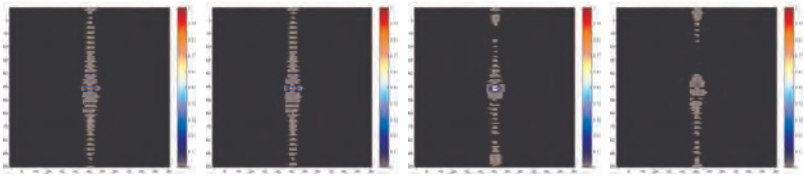

(q) Magnitude serial (r) Real serial (s) Imaginary serial (t) Real / imaginary serial

Figure 3.4: Image-space correlations for the center pixel in magnitude, real, imaginary and real/imaginary data with various processes included. In each case, only the listed operator was included. In the serial case, T_2^* decay, partial Fourier reconstruction, and k-space apodization were considered.

Operation	Left Neighbor Real	Left Neighbor Imaginary	Left Neighbor Real/Imaginary	Left Neighbor Magnitude^2	Right Neighbor Real	Right Neighbor Imaginary	Right Neighbor Real/Imaginary	Right Neighbor Magnitude^2
None	1.3e-16	1.3e-16	4.25e-17	3.3e-17	1.3e-16	1.3e-16	4.25e-17	3.3e-17
Uniform T_2^*	5.6e-8	5.6e-8	3.7e-5	1.2e-8	5.6e-8	5.6e-8	3.7e-5	1.2e-8
Varying T_2^*	4.9e-8	4.9e-8	3.4e-5	1.6e-8	4.9e-8	4.9e-8	3.4e-5	1.2e-8
B-Gradient	5.5e-7	5.5e-7	5.8e-10	7.5e-8	5.5e-7	5.5e-7	6.0e-10	7.7e-10
Partial Fourier	3.8e-5	8.9e-5	8.0e-17	7.0e-6	3.8e-5	8.9e-5	8.0e-17	7.0e-6
Partial Fourier and Uniform T_2^*	5.6e-5	4.0e-3	1.3e-6	1.3e-6	5.6e-5	4.0e-3	1.3e-6	1.3e-6
Partial Fourier and Varying T_2^*	7.7e-5	8.6e-4	9.3e-7	2.3e-6	7.7e-5	8.7e-4	1.3e-6	2.3e-6
Gaussian Smoothing	7.3e-1	7.3e-1	1.3e-16	7.3e-1	7.3e-1	7.3e-1	1.3e-16	7.3e-1
Varying T_2^* Partial Fourier and Smoothing	7.5e-1	7.5e-1	2.2e-4	7.5e-1	7.4e-1	7.4e-1	1.0e-4	7.4e-1
Varying T_2^* B-Gradient and Smoothing	8.2e-1	8.2e-1	2.9e-6	7.0e-1	7.5e-1	7.5e-1	2.7e-6	5.4e-1

Operation	Top Neighbor Real	Top Neighbor Imaginary	Top Neighbor Real/Imaginary	Top Neighbor Magnitude^2	Bottom Neighbor Real	Bottom Neighbor Imaginary	Bottom Neighbor Real/Imaginary	Bottom Neighbor Magnitude^2
None	5.4e-15	5.4e-15	9.2e-15	1.4e-15	5.4e-15	5.4e-15	9.2e-15	1.4e-15
Uniform T_2^*	4.9e-1	4.9e-1	2.0e-1	3.4e-3	4.9e-1	4.9e-1	2.0e-1	2.4e-3
Varying T_2^*	4.9e-1	4.9e-1	1.9e-1	5.2e-3	4.9e-1	4.9e-1	1.9e-1	3.6e-3
B-Gradient	2.7e-16	6.3e-17	8.1e-15	3.6e-17	1.5e-15	6.2e-20	1.1e-14	3.9e-16
Partial Fourier	2.6e-2	5.7e-1	1.0e-5	2.9e-3	2.6e-2	5.7e-1	1.0e-5	2.9e-3
Partial Fourier and Uniform T_2^*	5.3e-1	2.0e-1	1.1e-3	1.2e-1	5.3e-1	2.0e-1	1.1e-3	1.2e-1
Partial Fourier and Varying T_2^*	5.3e-1	1.1e-1	1.3e-3	1.0e-1	5.3e-1	1.1e-1	4.4e-4	1.2e-1
Gaussian Smoothing	7.3e-1	7.3e-1	2.8e-16	7.3e-1	7.3e-1	7.3e-1	2.8e-16	7.3e-1
Varying T_2^* Partial Fourier and Smoothing	3.7e-1	6.1e-1	2.2e-2	3.7e-1	3.3e-1	6.1e-1	1.1e-2	3.3e-1
Varying T_2^* B-Gradient and Smoothing	5.9e-1	5.9e-1	1.4e-1	5.8e-1	5.9e-1	5.9e-9	1.4e-1	5.9e-1

Table 3.1: Calculated correlation coefficients for the center voxel's nearest neighbors under several operations.

[Nencka et al., 2008]. In the data acquired with an excitation pulse a group delay of 5.6 μs (1.4 k-space points) between odd and even lines was observed. Without correction of the group delay, severe Nyquist ghosting existed in the reconstructed data. This resulted in correlations between image voxels and ghost voxels. Correction of the group delay error greatly reduced the Nyquist ghost and resulting image-space correlations. The same group delay error was assumed on the data set acquired without an excitation pulse. No significant image-space correlations were apparent before or after application of the group delay error correction, in agreement with the theoretical result that the even and odd line shifts do not induce correlation in pure noise data. The data acquired with no radio frequency excitation was found to exhibit uncorrelated normally distributed noise in space and time with a mean of zero. Global, temporal phase structure was corrected in the data set acquired with radio frequency excitation to account for field shifts associated with gradient heating and radio frequency phase variation [Hahn et al., 2008]. The data acquired with radio frequency excitation exhibited uncorrelated noise after phase correction. Thus, in both the no radio frequency excitation and the dynamic phase corrected data sets, there are no apparent structured correlations above the background correlations in the unprocessed data. Correlation coefficients in the experimental data for the four-neighbors of the center voxel under multiple processing conditions are shown in Table 3.2.

Smoothing of the noise data yields expected results, in agreement with those which are theoretically computed. The resulting images are shown in Figure 3.5. The similarity between the magnitude squared, real, imaginary, and real/imaginary

correlations in the smoothed noise data in Figures 3.5(a), 3.5(b), 3.5(c), and 3.5(d) and the theoretical cases in Figures 3.4(m), 3.4(n), 3.4(o) , and 3.4(p) supports the validity of the theoretical method. Some residual phase correlation manifests itself in the correlation maps for the radio frequency excited data in Figures 3.5(e), 3.5(f), 3.5(g) and 3.5(h). Nevertheless, these results are similar to the theoretically expected case.

3.5 Discussion

This work extends a line of research which has been briefly mentioned in a paper [Rowe et al., 2007b], and further developed in conference proceedings [Nencka and Rowe, 2007a, 2008]. In that work, the underlying theory for computing image-space correlations based upon k-space processes was developed. We have extended that work by developing multiple operators for common reconstruction processes which are defined in the first part of this chapter. We have studied the results of those operators by theoretically computing image-space correlations associated with relevant implementations. We have examined the validity of the operators and the theoretical image-space correlations by verifying the results in acquired phantom data.

The results presented in this chapter for individual operations may appear obvious, as relatively simple operations were considered. However, the utility of the method is demonstrated when multiple operations are considered at once. With this theoretical framework, the exact image-space point spread function may be computed following a string of processing operations on ideally uncorrelated data. This is useful as often a string of operations are performed on a data set. If all the common processes described here are implemented on a data set, the reconstructed image would be

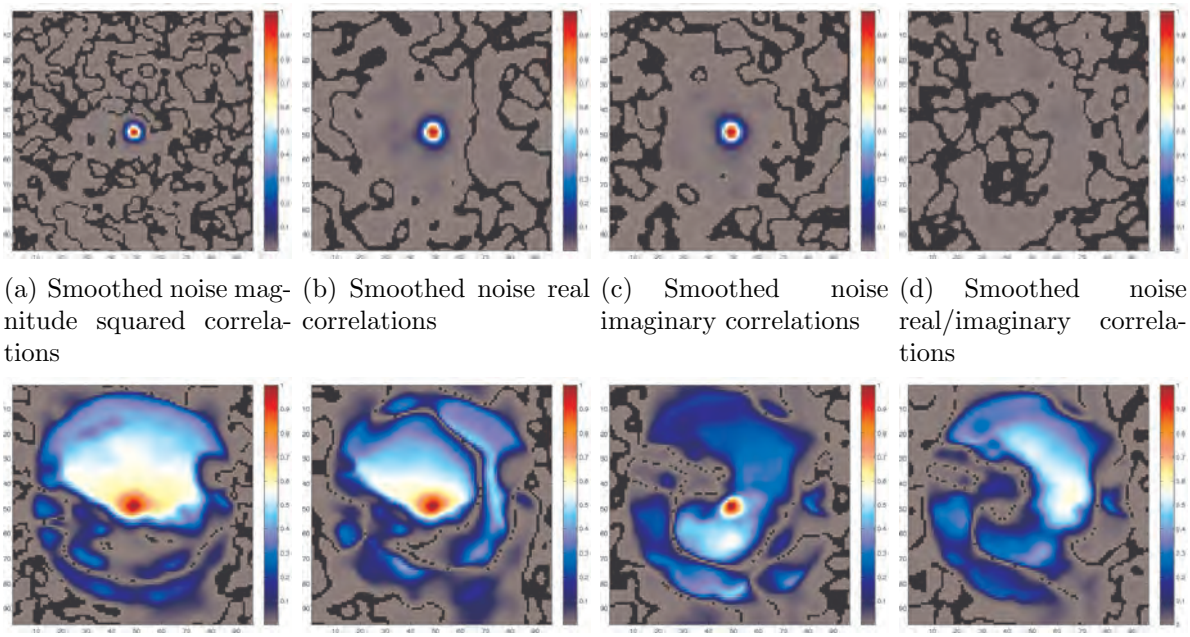

(a) Smoothed noise magnitude squared correlations

(b) Smoothed noise real correlations

(c) Smoothed noise imaginary correlations

(d) Smoothed noise real/imaginary correlations

(e) Smoothed excited dynamic B-field corrected magnitude squared correlations

(f) Smoothed excited dynamic B-field corrected real correlations

(g) Smoothed excited dynamic B-field corrected imaginary correlations

(h) Smoothed excited dynamic B-field corrected real/imaginary correlations

Figure 3.5: Image space correlations for the center voxel in the acquired phantom data with no excitation pulse (noise) and with an excitation pulse (excited) in the magnitude squared, real, imaginary and real/imaginary data after smoothing.

Operation	Left Neighbor Real	Left Neighbor Imaginary	Left Neighbor Real/Imaginary	Left Neighbor Magnitude^2	Right Neighbor Real	Right Neighbor Imaginary	Right Neighbor Real/Imaginary	Right Neighbor Magnitude^2
No RF, No Processing	1.6e-4	5.6e-4	1.4e-5	3.1e-4	1.8e-4	1.3e-4	8.0e-4	4.0e-4
Excitation	2.0e-5	1.2e-3	2.5e-3	2.9e-7	3.7e-4	1.6e-3	6.7e-10	8.3e-4
No RF, Partial Fourier	1.2e-3	2.2e-3	2.2e-3	2.8e-4	2.3e-4	5.0e-4	1.9e-4	1.3e-4
Excitation, Partial Fourier	2.5e-4	1.3e-4	4.4e-3	2.8e-4	1.1e-3	3.6e-4	8.0e-6	9.7e-4
No RF, Smoothing,	9.3e-1	9.3e-1	1.4e-5	8.7e-1	9.3e-1	9.4e-1	4.9e-4	8.7e-1
Excitation, Smoothing	9.8e-1	9.5e-1	1.2e-1	9.8e-1	9.8e-1	9.6e-1	2.3e-1	9.8e-1
Operation	Top Neighbor Real	Top Neighbor Imaginary	Top Neighbor Real/Imaginary	Top Neighbor Magnitude^2	Bottom Neighbor Real	Bottom Neighbor Imaginary	Bottom Neighbor Real/Imaginary	Bottom Neighbor Magnitude^2
No RF, No Processing	6.6e-3	2.1e-3	1.9e-5	1.8e-3	1.3e-4	1.1e-3	1.9e-3	1.1e-5
Excitation	1.4e-4	1.9e-5	3.2e-4	3.2e-4	1.9e-3	2.2e-3	4.1e-5	1.4e-3
No RF, Partial Fouier	1.2e-4	1.7e-3	6.3e-4	3.2e-3	1.0e-3	1.7e-3	5.1e-5	1.1e-7
Excitation, Partial Fourier	8.2e-4	7.4e-5	7.0e-4	7.7e-4	1.2e-3	8.7e-4	1.6e-4	1.3e-3
No RF, Smoothing	9.4e-1	9.3e-1	7.9e-4	8.8e-1	9.4e-1	9.4e-1	4.9e-6	8.8e-1
Excitation, Smoothing	9.7e-1	9.6e-1	1.6e-1	9.8e-1	9.7e-1	9.6e-1	1.6e-1	9.7e-1

Table 3.2: Correlation coefficients for the center voxel's nearest neighbors under several operations in experimental phantom data.

represented as

$$y = S_m \Omega_a A F H P_R^{-1} \Omega_{row}^{-1} \Phi \Omega_{row} P_R P_C R C \mathcal{S}. \tag{3.15}$$

The complicated process including all the described processing steps in Equation 3.15 lends itself well to this analytic mathematical model that is based upon simple linear algebra.

Furthermore, the alterations to an arbitrary covariance structure,Γ , may be examined. By computing the correlation structure following processing procedures on uncorrelated data, a reasonable null hypothesis threshold for experimental correlations may be considered. Thus, the theoretical method described in this chapter and previous abstracts may be used to consider how much spatial processing is too much when considering functional connectivity or fMRI data.

This method may be further expanded with operators for additional processing operations. Operators for parallel acquisition image reconstruction, transmit/receive field inhomogeneities, non-cartesian gridding, masking, and image shifting could easily be developed for the described framework. Additionally, continuing work seeks to further extend this model to include more relevant temporal processing. A time series of images could be considered by stacking k-space observation vectors to create a time series observation vector, and performing Kronecker products between the operators and identity matrices with dimensions equal to the number of time series observations. Under such a parameterization, the effects of temporal processing may also be examined. Operators for dynamic magnetic field correction [Hahn et al., 2008, 2009], motion correction [Jenkinson et al., 2002], slice timing correction [Henson et al., 1999], temporal band-pass and notch filtering, and temporal smoothing

[Gonzalez and Woods, 1992] may be developed by performing the Kronecker product with matrices other than identities. Thus, the full processing pipeline may be appropriately modeled with an extension to the described framework. In light of such a framework, statistical models may appropriately model the acquired data, rather than modeling data which has been preprocessed. Such models may allow scientists to statistically model the underlying physical changes associated with fcMRI and fMRI in more natural data [Rowe and Logan, 2004, 2005, Rowe, 2005a], rather than modeling the observed indirect magnitude signal fluctuations.

Current computational limitations prevent the full implementation of such a statistical model. For a 96×96 k-space acquisition matrix, the described operators are 18432×18432. If all double precision elements are saved to an array, such an array requires over 2.5 gigabytes of memory. In many cases, sparse matrix representations may be considered, but in cases including the Fourier operator or a modified Fourier operator, each element must be computed. As the matrix multiplication required to compute the alteration of a covariance matrix based upon the operation, $O\Gamma O^T = \Sigma$, requires three separate matrices in memory, O,Γ , andΣ , at least 7.5 gigabytes of memory must be addressed. Thus, 64-bit computing is essential. Further, hardware optimized matrix multiplication routines like the BLAS [Dongarra, 2002a,b] are essential for timely computations. If a time series of N images were to be considered, the memory requirements would grow by a factor of N^2 and the time for calculations would likewise grow. As the number of computing cores in personal computers continues to grow, and the availability of memory continues to increase, such calculations for reasonable time series will likely become possible in the relatively near future.

In spite of these technological issues, this chapter presents an exact theoretical means of computing image-space correlations which arise from processing operations, describes the construction of several common operators, presents theoretical results for common image acquisition techniques, and verifies those theoretical results in acquired echo planar data. The results illustrate that processing operations and physical processes affect computed voxel correlations, especially in local neighborhoods of voxels. This has strong implications for methods which consider correlations between nearby voxels, as the choice of processing techniques and the physical properties of the imaging subject may substantially affect computed results.

Chapter 4

Temporal processing

This chapter extends the work of the previous chapter. In the last chapter we described a linear framework for computing the effects of identical spatial processing procedures on all images of a time series. In this chapter we generalize the linear framework to include temporal processes as well as spatial processes. This allows the consideration of common fMRI processing steps including slice timing correction and temporal filtering. Additionally, this allows the consideration of dynamic magnetic field correction, which can be applied to experimental data to reduce the limitations of complex-valued analysis described in Chapter 2. In this chapter, in addition to describing the generalized linear framework and offering examples of common operators, we describe a means of including the effects of the described operators in statistical models. Thus, this framework not only allows researchers to evaluate the possible effects of processing decisions on acquired data, but it also allows researchers to model the data is it is acquired while including processing procedures in the fit model.

4.1 Introduction

Data processing is ubiquitous in functional MRI (fMRI) and functional connectivity MRI (fcMRI). Although processing yields results which are viewed to be improved, the steps of processing may fundamentally alter the signal and noise properties of the data and modify the distributional assumptions which can be made. Previous work has included elaborate Monte Carlo simulations to consider the effects of preprocessing [Della-Maggiore et al., 2002] and empirical studies to select "optimal" preprocessing procedures [LaConte et al., 2003, Shaw et al., 2003]. Such work evaluates the effect of preprocessing on the computed time series statistics to determine the "best" results, while the processing is not included in the statistical model.

Ideal methods for considering the effects of preprocessing on computed statistics should allow the processing to be included in the given statistical model. Such a consideration allows noise assumptions to be more naturally made on the acquired data, and allows the modification of the signal of interest through the inclusion of preprocessing of steps. Recent work from this lab has taken a major step in this direction [Nencka et al., 2009, Nencka and Rowe, 2007a, Rowe and Nencka, 2009]. In that work we developed a framework utilizing linear algebra to model common image processing techniques, including: static magnetic field correction [Jezzard and Balaban, 1995], partial Fourier reconstruction [Jesmanowicz et al., 1998], k-space apodization, zero-filling and image-space smoothing [Bernstein et al., 2004]. Each of these processing techniques were shown to modify the correlation structure of observed data, even if the acquired data was uncorrelated.

In this chapter we further advance the linear algebra framework to include tem-

poral processing of the data. Specifically we develop operators for image registration [Jenkinson et al., 2002], dynamic magnetic field correction [Hahn et al., 2009], slice timing correction [Huettel et al., 2004], and temporal filtering [Huettel et al., 2004]. We then demonstrate the operators with a low dimensional toy example. Finally we illustrate the effects of one operator on an acquired data set as an example.

4.2 Theory

4.2.1 Operator Covariance Modifications

Previous work has shown that the reconstruction process and k-space image processing may be represented through linear algebra [Rowe et al., 2007b, Nencka and Rowe, 2007a, Nencka et al., 2009]. In such cases, the vectorized observed k-space signal for an image of p voxels, $s = (s_1, \ldots, s_p)'$, may be multiplied by a reconstruction and processing operator, O. Thus, if the expected signal is defined by $\mathrm{E}(s) = s_0$ and the covariance matrix of the observed signal isΓ , the expected value of the data after reconstruction and processing is Os_0, and the covariance after reconstruction and processing is $O\Gamma O^T$.

Here we provide an extension to the previous work to allow the consideration of temporal processes in addition to spatial image processes. The vectorized observed k-space time series signal may now be considered as $s_T = (s_{11}, s_{12}, \ldots, s_{1p}, s_{21}, \ldots, s_{np})'$, which is a stack of n k-space signal vectors, with each of the n k-space vectors representing one time point. Spatial and temporal processes may be considered on the vector s_T with premultiplication with operator matrices, O_T. New operators for O_T must thus be constructed to consider the processing of this large time series vector.

4.2.2 Temporal Operators

In the following sections we describe the construction of an important subset of possible operators which may be considered in this framework. The operators which we will describe include: spatial processing of a time series of images, performing temporally dynamic B-field corrections, performing slice timing correction, shifting and rotating images for registration, and performing temporal filtering.

In the following sections, an ideal covariance matrix,Γ , is initially assumed, and all operators are described to act upon the ideal acquired k-space data. Thus, the final operators illustrated in Figure 4.1 are the product of (1) k-space processing operators, K, (2) reconstruction operators, R, (3) image-space operators, I, and (4) time series operators, T. As temporal and spatial domains are considered, some operators include products with permutation matrices to reorder the data. The illustrated operators are the product $O_T = TIRK$. The observed k-space signal is equal to the vectorized spin density multiplied by an encoding operator which includes intra-acquisition decay and B-field inhomogeneities. When only one operation is considered, all other operators are parametrized so that they may be represented by identity matrices. We will describe a subset of the operators below, with example operators shown in Figure 4.1 that have their parameters described in Section 4.3.1. Standard Fourier reconstruction with no other spatial or temporal processes is illustrated in 4.1(a).

Encoding Operators

Intra-acquisition decay and magnetic field inhomogeneities may be modeled as part of a Fourier encoding matrix for standard, Cartesian MRI. A standard forward

Fourier encoding operator has been defined by Rowe et al. [2007b]. To include the effects of T_2^* decay and B-field inhomogeneities, the operator must be modified such that each element is modulated by the appropriate real or imaginary component of the exponential $\exp\left(t(k_x,k_y)\left(-1/T_2^*(x,y)+i\gamma\Delta B(x,y)/\left(2\pi\right)\right)\right)$, where $t(k_x,k_y)$ represents the time at which the k-space point corresponding to the row of the Fourier encoding matrix was acquired, and $T_2^*(x,y)$ and$\Delta\ B(x,y)$ represent the transverse relaxation time and B-field error corresponding to the image-space point that the column of the Fourier encoding matrix represents [Nencka et al., 2009]. The gyromagnetic ratio of the proton is represented by γ. An operator including only modeled intra-acquisition decay in the encoding matrix, E, is shown in Figure 4.1(b).

Generalization of k-space Image Operators

Previous work has shown the effects of processing individual images [Nencka and Rowe, 2007a, Nencka et al., 2009]. In that case, a temporally unchanging image processing operator, O_k, was considered on identical signal images. Operations included: correcting intra-acquisition decay, correcting static B-field error, partial Fourier extrapolation, k-space apodization, k-space zero filling, Fourier reconstruction, and image-space smoothing. To apply such operators to the newly parametrized time series data requires an operator of higher dimensionality. If the same image processing steps are performed on all time points of an acquired k-space time series, the time series image processing operator, K, may be calculated as a Kronecker product between the previously described image processing operator and an identity matrix with dimension matching the number of time series points, $K = I_n \otimes O_k$. The symbol $\otimes$ represents the Kronecker product in which each element of the first matrix multi-

plies the second matrix. If the first matrix is of $a \times b$ dimensionality and the second matrix has dimensions of $c \times d$, the Kronecker product has dimensions of $ac \times bd$. The resulting time series k-space image processing operator, K, is thus block diagonal with each diagonal block corresponding to an instance of the image processing operator. An operator including only k-space apodization is shown in Figure 4.1(c).

Dynamic B-Field Correction

Dynamic B-field correction may be performed with the alteration of the inverse Fourier reconstruction operator, R. The magnetic field to be corrected may be measured through relative field measurements [Hahn et al., 2009] or intra-acquisition measurements [Roopchansingh et al., 2003]. With the field error known, the equivalent of the time segmented B-field correction approach described by Noll et al. [1991], with each k-space point being an individual time segment, may be performed on each acquired k-space data set. For each k-space vector, the corresponding Fourier reconstruction matrix must be multiplied by $\exp(-i\gamma\Delta B(x,y)t(k_x,k_y))$. A real-valued isomorphism of the Fourier array as described by Rowe et al. [2007b] is constructed for the inverse of each time point's B-field error and placed in the diagonal position corresponding to the considered time series point's vector. This is essentially the inverse of the encoding operator which assumes a B-field error. An operator including only dynamic B-field correction is shown in Figure 4.1(d). Likewise, an intra-acquisition decay correction operator may be created based upon separately measured T_2^* properties.

Image Registration

Image registration is performed by shifting each image based upon independently determined motion parameters. Such motion parameters may be determined through software [Cox, 1996, Jenkinson et al., 2002] or through external means [Tremblay et al., 2005]. In a two dimensional case, the image registration operator may be considered as another block diagonal matrix. A more elaborate three dimensional registration operator may be constructed by further generalizing this operator and utilizing three dimensional Fourier transforms. However, in this chapter, we describe the notationally simpler case of in-plane motion correction where the registration may be integrated into the reconstruction operator, R. Each block of the operator multiplies the k-space data with an appropriate phase before Fourier reconstruction to yield a correctional shift in image-space after reconstruction. For an image-space translation of $(\delta x, \delta y)$ and in-plane rotation of θ, the required image-space shift for a voxel at (x, y) in image space is$\Delta\ x = \delta x + x(\cos(\theta) - 1) + y\sin(\theta)$, and$\Delta\ y = \delta y + y(\cos(\theta) - 1) - x\sin(\theta)$. Therefore, for a single image with the above described motion parameters, the row of the Fourier operator representing the image-space point (x, y) must have each element multiplied by $\exp(-i2\pi(\Delta x k_x/p_x + \Delta y k_y/p_y))$, where k_x and k_y are integers representing the k-space indices of the column of the Fourier matrix and p_x and p_y are the number of k-space points in the x and y directions respectively. The complex-valued Fourier matrices may be converted by the real valued isomorphism described in Rowe et al. [2007b]. Each of the n blocks of the block diagonal matrix for the image registration and reconstruction operator can be likewise created using the real-valued Fourier isomorphism with the appropriate $(\delta x, \delta y)$ and

θ for the appropriate slices. An operator including only image registration is shown in Figure 4.1(e).

Slice Timing Correction

Slice timing correction is performed in image-space after spatial processing and registration are performed. In this case, it is useful to perform slice timing correction through the performance of multiple steps. First, one may reorder the vector of reconstructed images to a vector of reconstructed voxel time series through multiplication with a permutation matrix. Then, one may Fourier transform each time series into the temporal frequency domain through a multiplication with a block diagonal matrix where each block is a real-valued isomorphism of a time series Fourier matrix. Each transformed time series may be multiplied by sines and cosines to create additional phase for the time series shift. Inverse Fourier transforming the vectors of temporal frequencies leads to temporally shifted time series, and multiplication with the inverse of the original permutation matrix returns the vector of temporally shifted time series to vector of temporally shifted images.

It should be noted that this process is mathematically identical to the line shifting process described in Nencka et al. [2009] to correct Nyquist ghosts in echo planar imaging. In that case, if uncorrelated data is assumed, it was shown that the shifting of k-space lines does not induce correlations in the acquired data. Likewise, if uncorrelated data is assumed, slice timing correction can be mathematically shown to not modify the correlation in the acquired data, as this operator multiplied by its inverse yields the identity matrix. An operator including only slice timing correction is shown in Figure 4.1(f).

Temporal Filtering

The process of temporal filtering is similar to the process of slice timing correction. Multiplication with a permutation matrix and a real-valued isomorphism of a time series Fourier matrix can transform the image time series vector into a temporal frequency vector. Then multiplication with a diagonal matrix with each diagonal element representing a frequency space weighting for a temporal filter can be performed. Inverse Fourier transformation and inverse permutation will then yield the temporally filtered image time series vector. An operator including only temporal filtering is shown in Figure 4.1(g).

4.2.3 Functional Correlations

With the ideal covariance matrix,Γ , known, one may determine the reconstructed and processed covariance matrix,Σ , through the simple calculation $\Sigma = O_T \Gamma O_T^T$. As described, Σ is a $2pn \times 2pn$ matrix with diagonal blocks which contain the covariance matrices for individual images. In this section we show that the $p \times p$ voxel time series covariance matrix,Σ_ρ, can be estimated from the large, experimental covariance matrix,Σ . It isΣ_ρ which may be converted into a time series correlation matrix, ρ, which is utilized for functional connectivity studies.

Consider the large, processed covariance matrix,Σ . The i, j^{th} element may be calculated as

$$\Sigma_{x_i y_i z_i t_i x_j y_j z_j t_j} = \mathrm{E}\left(\left(y_{x_i y_i z_i t_i} - \bar{y}_{x_i y_i z_i t_i} \right) \left(y_{x_j y_j z_j t_j} - \bar{y}_{x_j y_j z_j t_j} \right) \right),$$

where (x_i, y_i, z_i, t_i) are the spatial and temporal indices for the i^{th} element of the re-

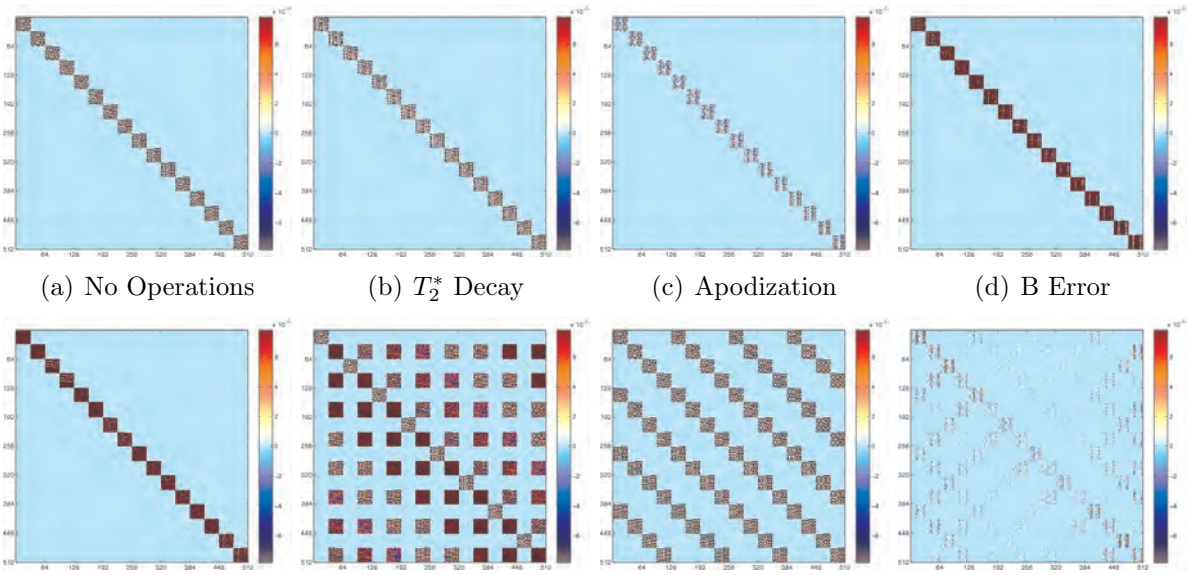

(a) No Operations (b) T_2^* Decay (c) Apodization (d) B Error

(e) Motion Correction (f) Timing Correction (g) Temporal Filtering (h) All Operations

Figure 4.1: Operators for an acquisition of 8 repetitions of a $4 \times 4 \times 2$ voxel region of interest. (a) No operations. (b) Intra-acquisition decay. (c) Apodization. (d) B-field error. (e) Motion Correction. (f) Slice timing correction. (g) Temporal band stop filtering. (h) All operations in series.

constructed and processed vector y, (x_j, y_j, z_j, t_j) are the spatial and temporal indices for the vector's j^{th} element, and $\bar{y}_{x_i y_i z_i t_i}$ is the mean measurement of voxel (x_i, y_i, z_i) at time point t in repeated acquisitions. Expanding the product, the element may be considered as

$$\Sigma_{x_i y_i z_i t_i x_j y_j z_j t_j} = \mathrm{E}\left(y_{x_i y_i z_i t_i} y_{x_j y_j z_j t_j} - y_{x_i y_i z_i t_i} \bar{y}_{x_j y_j z_j t_j} - y_{x_j y_j z_j t_j} \bar{y}_{x_i y_i z_i t_i} + \bar{y}_{x_i y_i z_i t_i} \bar{y}_{x_j y_j z_j t_j}\right).$$

Similarly, the voxel time series covariance matrix,Σ_{ρ}, may be considered on an element by element basis

$$\Sigma_{\rho_{ij}} = \mathrm{E}\left(\left(y_{x_i y_i z_i} - \bar{y}_{x_i y_i z_i}\right)\left(y_{x_j y_j z_j} - \bar{y}_{x_j y_j z_j}\right)\right),$$

where $\bar{y}_{x_i y_i z_i}$ is the temporal mean of the voxel (x_i, y_i, z_i) over the course of a time series acquisition. In a time series with n points,Σ_{ρ} may be calculated as

$$\begin{aligned}
\Sigma_{\rho_{ij}} &= \frac{1}{n-1}\sum_{t=1}^{n}\left(\left(y_{x_i y_i z_i t} - \bar{y}_{x_i y_i z_i}\right)\left(y_{x_j y_j z_j t} - \bar{y}_{x_j y_j z_j}\right)\right) \\
&= \frac{1}{n-1}\sum_{t=1}^{n}\left(y_{x_i y_i z_i t} y_{x_j y_j z_j t} - y_{x_i y_i z_i t} \bar{y}_{x_j y_j z_j} - y_{x_j y_j z_j t} \bar{y}_{x_i y_i z_i} + \bar{y}_{x_i y_i z_i} \bar{y}_{x_j y_j z_j}\right).
\end{aligned}$$

WithΣ_{ρ} in mind, consider the average of the diagonal blocks of the large, processed

covariance matrix,Σ . Specifically, let

$$\begin{aligned}
\Sigma_{R_{ij}} &= \frac{1}{n-1}\sum_{t=1}^{n}\Sigma_{x_iy_iz_it_t,x_jy_jz_jt_t} \\
&= \frac{1}{n-1}\sum_{t=1}^{n}\mathrm{E}\left(y_{x_iy_iz_it}y_{x_jy_jz_jt_t} - y_{x_iy_iz_it_t}\bar{y}_{x_jy_jz_jt_t} - y_{x_jy_jz_jt_t}\bar{y}_{x_iy_iz_it_t} + \bar{y}_{x_iy_iz_it_t}\bar{y}_{x_jy_jz_jt_t}\right) \\
&= \mathrm{E}\left(\frac{1}{n-1}\sum_{t=1}^{n}y_{x_iy_iz_it}y_{x_jy_jz_it_t} - y_{x_iy_iz_it_t}\bar{y}_{x_jy_jz_jt_t} - y_{x_jy_jz_jt_t}\bar{y}_{x_iy_iz_it_t} + \bar{y}_{x_iy_iz_it_t}\bar{y}_{x_jy_jz_jt_t}\right).
\end{aligned}$$

Assuming that the voxel mean does not change over time, as should be the case in a resting state study of a stationary subject in a stable scanner, $\bar{y}_{xyzt}$ is equal to $\bar{y}_{xyz}$. In light of this, it is apparent that the average of the diagonal blocks of the large, processed covariance matrix,Σ , is the expected value of the voxel time series covariance matrix,$\Sigma_{\ \rho}$

$$\begin{aligned}
\Sigma_{R_{ij}} &= \mathrm{E}\left(\frac{1}{n-1}\sum_{t=1}^{n}y_{x_iy_iz_it}y_{x_jy_jz_jt_t} - y_{x_iy_iz_it_t}\bar{y}_{x_jy_jz_j} - y_{x_jy_jz_jt_t}\bar{y}_{x_iy_iz_i} + \bar{y}_{x_iy_iz_i}\bar{y}_{x_jy_jz_j}\right) \\
\Sigma_{R_{ij}} &= \mathrm{E}\left(\Sigma_{\rho_{ij}}\right).
\end{aligned}$$

Thus, the voxel time series covariance matrix may be computed as the average of the diagonal blocks of the large, processed covariance matrix.

4.2.4 Functional Activations

As stated above, with the ideal covariance matrix,Γ , known, one may calculate the reconstructed and processed covariance matrix,Σ , through the simple calculation $\Sigma = O_T\Gamma O_T^T$. As described, Σ is a $2pn \times 2pn$ matrix with diagonal blocks of dimension $2p \times 2p$ which contain the covariance matrices for individual images. Thus, although

the large covariance matrix Σ contains the components necessary to compute one voxel's time series covariance matrix,Σ_v, Σ must be reordered. The permutation operator described above which reorders the reconstructed data from a vector of n vectors of p observations stacked above themselves to the reconstructed time series vector of p vectors of n observations stacked above themselves may be used. If that permutation matrix is P, the reordered covariance matrix is calculated as $P\Sigma P^T$. The p diagonal blocks of this covariance matrix are theΣ_v covariance matrices for the p individual voxels.

With the voxel time series covariance matrices,Σ_v, known, it is possible to consider a generalized least squares approach to the complex-valued general linear model for functional activations. Several instances of the complex-valued general linear model have been described in previous work from this group [Rowe and Logan, 2004, 2005, Rowe, 2005a,b].

The complex data model is:

$$\begin{pmatrix} y_R \\ y_I \end{pmatrix} = \begin{pmatrix} CX\beta \\ SX\beta \end{pmatrix} + \begin{pmatrix} \eta_R \\ \eta_I \end{pmatrix}, \qquad \begin{pmatrix} \eta_R \\ \eta_I \end{pmatrix} \sim N\left(0, \sigma^2\Sigma_v\right),$$

where y_R and y_I are n-element vectors of the real and imaginary processed time series, C is a diagonal matrix with the cosine of each time point's modeled voxel phase angle as the diagonal elements, S is a diagonal matrix with the sine of each time point's modeled phase angle as the diagonal elements, X is the experimental design matrix, β is the vector of unknown magnitude regression coefficients, and η_R and η_I are the time series of the real and imaginary noise with a correlation matrix

which is modified by the data processing. The above parameterization extends the originally described complex data models by allowing a non-identityΣ_v [Rowe and Logan, 2004, 2005, Rowe, 2005a]. For simplicity, the constant phase method [Rowe and Logan, 2004] is considered in this chapter although the same methodology can be used to consider other complex data models. In the constant phase model, each time point voxel phase is modeled by a constant phase over the time series. Thus, C and S are identity matrices scaled by the cosine and sine of the voxel's constant temporal phase.

A likelihood ratio test statistic can be computed to consider functional activations under this model. This statistic considers the estimated variances under the null hypothesis that there is no task related cortical activity, and under the alternative hypothesis that there is cortical signal which may be modeled as being related to task.

Least squares estimates of β, σ^2, and θ under the unconstrained alternative hy-

pothesis may be computed on a voxelwise basis as described in Appendix I to be:

$$\begin{aligned}\hat{\beta} = &\left(2X'\hat{C}'\Sigma_A\hat{C}X + 2X'\hat{S}'\Sigma_C\hat{C}X + 2X'\hat{C}'\Sigma_B\hat{S}X + 2X'\hat{S}'\Sigma_D\hat{S}X\right)^{-1} \\ &\times \left(2y_R'\Sigma_A\hat{C}X + y_I'\Sigma_C\hat{C}X + X'\hat{S}'\Sigma_C y_R + \right. \\ &\left. y_R'\Sigma_B\hat{S}X + X'\hat{C}'\Sigma_B y_I + 2y_I\Sigma_D\hat{S}X\right) \end{aligned} \tag{4.1}$$

$$\begin{aligned}\hat{\alpha} = &y_R'\Sigma_A y_R - 2y_R\Sigma_A\hat{C}X\hat{\beta} + \hat{\beta}'X'\hat{C}'\Sigma_A\hat{C}X\hat{\beta} + \\ &y_I'\Sigma_C y_R - y_I'\Sigma_C\hat{C}X\hat{\beta} - \hat{\beta}'X'\hat{S}'\Sigma_C y_R + \hat{\beta}'X'\hat{S}'\Sigma_C\hat{C}X\hat{\beta} + \\ &y_R'\Sigma_B y_I - y_R'\Sigma_B\hat{S}X\hat{\beta} - \hat{\beta}'X'\hat{C}'\Sigma_B y_I + \hat{\beta}'X'\hat{C}'\Sigma_B\hat{S}X\hat{\beta} + \\ &y_I'\Sigma_D y_I - 2y_I\Sigma_D\hat{S}X\hat{\beta} + \hat{\beta}'X'\hat{S}'\Sigma_D\hat{S}X\hat{\beta} \end{aligned} \tag{4.2}$$

$$\hat{\sigma}^2 = \frac{\hat{\alpha}}{2n} \tag{4.3}$$

$$\hat{\theta} = \arctan\left(\frac{1/n\sum_{t=1}^{n}\sin(\hat{\theta}_t)}{1/n\sum_{t=1}^{n}\cos(\hat{\theta}_t)}\right) \tag{4.4}$$

$$\hat{\theta}_t = \arctan\left(y_{It}/y_{Rt}\right) \tag{4.5}$$

$$\Sigma_v^{-1} = \begin{pmatrix} \Sigma_A & \Sigma_B \\ \Sigma_C & \Sigma_D \end{pmatrix} \tag{4.6}$$

$$\Sigma_v = \begin{pmatrix} \Sigma_r & \Sigma_{ri} \\ \Sigma_{ir} & \Sigma i \end{pmatrix} \tag{4.7}$$

$$\Sigma_A^{-1} = \left(\Sigma_r - \Sigma_{ri}\Sigma_i^{-1}\Sigma_{ir}\right)^{-1} \tag{4.8}$$

$$\Sigma_B^{-1} = \Sigma_r^{-1}\left(-\Sigma_{ri}\left(\Sigma_i - \Sigma_{ir}\Sigma_r^{-1}\Sigma_{ri}\right)^{-1}\right) \tag{4.9}$$

$$\Sigma_C^{-1} = \Sigma_i^{-1}\left(-\Sigma_{ir}\left(\Sigma_r - \Sigma_{ri}\Sigma_i^{-1}\Sigma_{ir}\right)^{-1}\right) \tag{4.10}$$

$$\Sigma_D^{-1} = \left(\Sigma_i - \Sigma_{ir}\Sigma_r^{-1}\Sigma_{ri}\right)^{-1} \tag{4.11}$$

where $\hat{C} = \cos(\hat{\theta})I_n$ and $\hat{S} = \sin(\hat{\theta})I_n$.

Least squares estimates of β, σ^2, and θ under the constrained null hypothesis where $V\beta = \delta$ may be computed on a voxelwise basis as described in Appendix J to be:

$$\begin{aligned}
\tilde{\psi} = & \left[V\left(2X'\tilde{C}'\Sigma_A\tilde{C}X + 2X'\tilde{S}'\Sigma_C\tilde{C}X + 2X'\tilde{C}'\Sigma_B\tilde{S}X + 2X'\tilde{S}'\Sigma_D\tilde{S}X\right)^{-1}V'\right]^{-1} \\
& \times \left[V\left(2X'\tilde{C}'\Sigma_A\tilde{C}X + 2X'\tilde{S}'\Sigma_C\tilde{C}X + 2X'\tilde{C}'\Sigma_B\tilde{S}X + 2X'\tilde{S}'\Sigma_D\tilde{S}X\right)^{-1}\right. \\
& \times \left(2y_R'\Sigma_A\tilde{C}X + y_I'\Sigma_C\tilde{C}X + X'\tilde{S}'\Sigma_C y_R + \right. \\
& \left.\left. y_R'\Sigma_B\tilde{S}X + X'\tilde{C}'\Sigma_B y_I + 2y_I'\Sigma_D\tilde{S}X\right) - \delta\right] \qquad (4.12) \\
\tilde{\beta} = & \left(2X'\tilde{C}'\Sigma_A\tilde{C}X + 2X'\tilde{S}'\Sigma_C\tilde{C}X + 2X'\tilde{C}'\Sigma_B\tilde{S}X + 2X'\tilde{S}'\Sigma_D\tilde{S}X\right)^{-1} \\
& \times \left(2y_R'\Sigma_A\tilde{C}X + y_I'\Sigma_C\tilde{C}X + X'\tilde{S}'\Sigma_C y_R + \right. \\
& \left. y_R'\Sigma_B\tilde{S}X + X'\tilde{C}'\Sigma_B y_I + 2y_I'\Sigma_D\tilde{S}X - \tilde{\psi}'V\right) \qquad (4.13) \\
\tilde{\alpha} = & y_R'\Sigma_A y_R - 2y_R\Sigma_A\tilde{C}X\tilde{\beta} + \tilde{\beta}'X'\tilde{C}'\Sigma_A\tilde{C}X\tilde{\beta} + \\
& y_I'\Sigma_C y_R - y_I'\Sigma_C\tilde{C}X\tilde{\beta} - \tilde{\beta}'X'\tilde{S}'\Sigma_C y_R + \tilde{\beta}'X'\tilde{S}'\Sigma_C\tilde{C}X\tilde{\beta} + \\
& y_R'\Sigma_B y_I - y_R'\Sigma_B\tilde{S}X\tilde{\beta} - \tilde{\beta}'X'\tilde{C}'\Sigma_B y_I + \tilde{\beta}'X'\tilde{C}'\Sigma_B\tilde{S}X\tilde{\beta} + \\
& y_I'\Sigma_D y_I - 2y_I\Sigma_D\tilde{S}X\tilde{\beta} + \tilde{\beta}'X'\tilde{S}'\Sigma_D\tilde{S}X\tilde{\beta} \qquad (4.14) \\
\tilde{\sigma}^2 = & \frac{\tilde{\alpha} + \tilde{\psi}'\left(V\tilde{\beta} - \delta\right)}{2n} \qquad (4.15) \\
\tilde{\theta} = & \arctan\left(\frac{1/n\sum_{t=1}^{n}\sin(\tilde{\theta}_t)}{1/n\sum_{t=1}^{n}\cos(\tilde{\theta}_t)}\right) \qquad (4.16) \\
\tilde{\theta}_t = & \arctan\left(y_{It}/y_{Rt}\right). \qquad (4.17)
\end{aligned}$$

In the case of a baseline, linear trend and task response being modeled, β is a three

element vector, $\beta = (\beta_0, \beta_1, \beta_2)'$. In this vector, β_0 is the baseline regression coefficient, β_1 is the linear trend regression coefficient, and β_2 is the task related regression coefficient. In the restricted case described here, $V = (0, 0, 1)'$, and $\delta = 0$. In the estimators under the null hypothesis,$\Sigma_{A}, \Sigma_B, \Sigma_C$, and$\Sigma_{D}$ are the same as those computed in Equations 4.8, 4.9, 4.10, and 4.11 under the alternative hypothesis.

As it has been previously mentioned, the maximum likelihood estimators can be used to test for the significance of β_2 utilizing a likelihood ratio statistic with a large sample χ^2 distribution under the null hypothesis:

$$-2 \log \lambda_{CP} = n \log \frac{\hat{\sigma}^2}{\tilde{\sigma}^2}.$$

This statistic may be transformed into a z-statistic for standard fMRI analysis when V has one row, as in Rowe and Logan [2004].

4.3 A Computational Example

The above described operators have been implemented and have been used to consider processing induced alterations in acquired data with both an identity covariance matrix and with a voxel-wise autocorrelated time series (AR(1) with an autocorrelation factor of 0.5) covariance matrix to more closely match acquired data.

4.3.1 Methods

Several linear operators have been deployed in Matlab for their consideration on uncorrelated and autocorrelated ideal data sets. Operators have been implemented for: permuting the acquired real/imaginary pairs into image-wise sets of real and

imaginary data; Fourier encoding an ideal proton spin density with aberrations from intra-acquisition T_2^* decay, motion, and Δ B-field errors; Fourier reconstructing the encoded image; permuting the image-wise sets of real and imaginary data into voxel time series sets of real and imaginary data; Fourier transforming the voxel time series sets into and back from temporal frequency space, applying temporal filters to the Fourier transformed voxel time series; and applying temporal shifts to the Fourier transformed voxel time series. Such linear operators can be of very large dimensionality. However, individual k-space image processing operators have shown great effect in only the local neighborhood of considered voxels [Nencka et al., 2009]. Thus, the considered operators have been developed to observe alterations in the correlation structure within a neighborhood of a considered voxel to reduce the problem's dimensionality. A censoring or masking matrix consisting of an identity matrix with rows deleted for unconsidered points mathematically describes this reduction to a region of interest. Operators were considered for a masked 4×4 voxel region of interest in two consecutive slices in a time series of 8 repetitions. As the considered linear operators are a real-valued isomorphism of the complex valued operations, this yields operators which are of dimension 6400×6400. As the series of operators shuffle the rows and columns of the several block diagonal linear operators, it was found that sparse matrix representations were not beneficial as compound operators including several operations do not share the sparseness of the individual operators.

Each operator was considered individually, and all of the operators were considered in series. Assumed acquisition parameters included a repetition time of 2000.0 ms, echo time of 50.0 ms, and effective echo planar echo spacing time of 1.0 ms.

When included, the intra-acquisition decay was modeled as exponential with T_2^* values defined by a modified Shepp-Logan phantom [Jain, 1989] scaled from 1×10^{-6} to 0.1 s inside the head and 1×10^6 s oustside head, where the proton spin density was assumed to be zero, to avoid division by zero. When not explicitly included, the intra-acquisition decay was assumed to be exponential with $T_2^* = 1 \times 10^6$ s. When included, the magnetic field inhomogeneity was modeled as a linear gradient, ranging from -5×10^{-6} T to 5×10^{-6} T, along a direction which varied linearly over the time series acquisition from being horizontal to vertical. When not included, the magnetic field inhomogeneity was modeled as 0.0 T. Motion was modeled as a cumulative shift of one pixel in the horizontal direction, one pixel in the vertical direction, and in-plane rotation of 2 degrees over the course of the time series when included, and modeled as no shift or rotation when not included. Temporal filtering was considered with a band rejection filter, with cut off frequencies of 0.1250 Hz and 0.1875 Hz when included, and as a full spectrum pass filter when not included. Temporal shifting was modeled as a shift of the second slice by one half of the repetition time when included, and as no shift when not included. Spatial smoothing was considered as Gaussian smoothing with a kernel with an image-space full width at half maximum of three pixels, and as convolution with a delta function when not considered.

4.3.2 Results

Figure 4.1 shows the deployed operators, and Figure 4.2 includes the calculated correlation matrices after applying the operators to uncorrelated and autocorrelated data. Figure 4.3 shows the resulting image series correlation matrices for the center voxel, as described in section 4.2.3, and Figure 4.4 shows the resulting time series

correlation matrices for one voxel as described in section 4.2.4. The correlation matrices with no processing are shown in Figures 4.2(a), 4.2(i), 4.3(a), 4.3(i), 4.4(a), and 4.4(i).

We have found that a Fourier encoding operator, modified to account for intra-acquisition decay or B-field inhomogeneities, matched with a standard Fourier reconstruction operator yields the same results as a standard Fourier encoding operator matched with a Fourier reconstruction operator, modified to account for the same effects. Figures 4.2(b), 4.2(j), 4.3(b), 4.3(j), 4.4(b), and 4.4(j) illustrate the results of intra-acquisition decay when considered in such a way. The results illustrate the effects of the process when it is not corrected in processing. Thus, as previously described by Jesmanowicz et al. [1998] and illustrated by the AMMUST-k method for individual images [Nencka et al., 2009], intra-acquisition decay yields spatial correlation along the phase encoding direction without altering time series autocorrelation.

The image operator of apodization, previously described as an AMMUST-k method, also yields identical results under this AMMUST-T generalization. Specifically, as seen in Figures 4.2(c), 4.2(k), 4.3(c), 4.3(k), 4.4(c) and 4.4(k), apodization yields increased correlation of a voxel with its neighbors while not altering time series autocorrelation.

Temporally varying B-field errors lead to image-space correlations which vary over time. Spatial correlations associated with image warping are seen in Figures 4.3(d) and 4.3(l). Such altered correlation matrices are used in functional connectivity studies. Thus, dynamically changing B-field errors can lead to time series correlations which are not of interest in the acquired data. The matrices in Figures 4.3(d) and

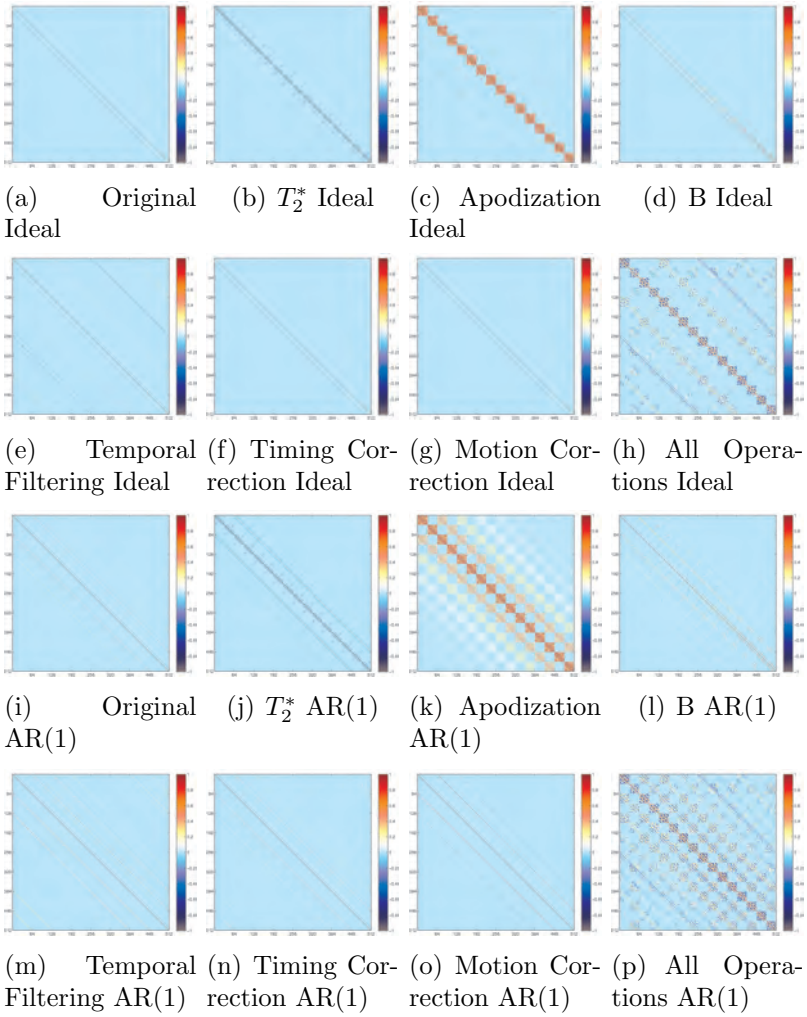

(a) Original Ideal (b) T_2^* Ideal (c) Apodization Ideal (d) B Ideal

(e) Temporal Filtering Ideal (f) Timing Correction Ideal (g) Motion Correction Ideal (h) All Operations Ideal

(i) Original AR(1) (j) T_2^* AR(1) (k) Apodization AR(1) (l) B AR(1)

(m) Temporal Filtering AR(1) (n) Timing Correction AR(1) (o) Motion Correction AR(1) (p) All Operations AR(1)

Figure 4.2: Correlation matrices resulting from the considered operators acting upon uncorrelated (ideal) data (a-h) and autocorrelated (AR(1)) data (i-p). The results of no operations (a and i), intra-acquisition decay (b and j), k-space apodization (c and k), dynamic B-field correction (d and l), temporal band block filtering (e and m), slice timing correction (f and n), motion correction (g and o), and all processes in series (h and p) are shown.

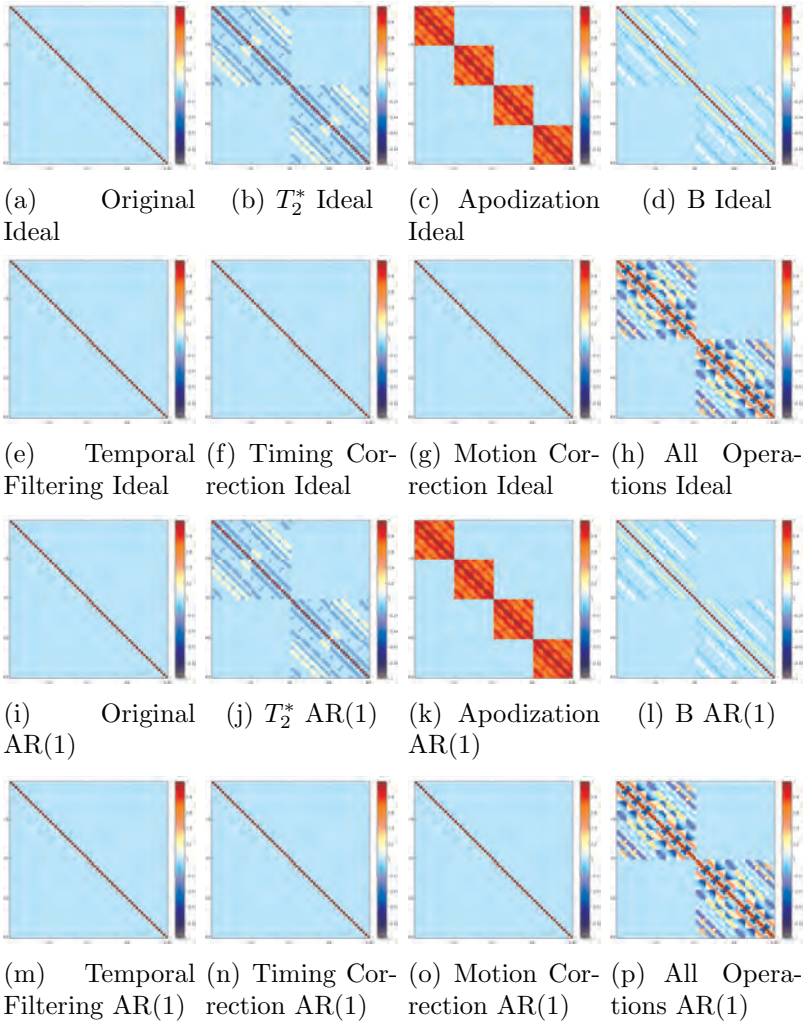

(a) Original Ideal (b) T_2^* Ideal (c) Apodization Ideal (d) B Ideal

(e) Temporal Filtering Ideal (f) Timing Correction Ideal (g) Motion Correction Ideal (h) All Operations Ideal

(i) Original AR(1) (j) T_2^* AR(1) (k) Apodization AR(1) (l) B AR(1)

(m) Temporal Filtering AR(1) (n) Timing Correction AR(1) (o) Motion Correction AR(1) (p) All Operations AR(1)

Figure 4.3: Image time series correlation matrices derived from the computed large correlation matrices. These matrices represent correlation matricies which would be considered in fcMRI studies. Uncorrelated (ideal, a-h) and correlated (AR(1), i-p) original data were considered with no operations (a and i), intra-acquisition decay (b and j), k-space apodization (c and k), dynamic B-field correction (d and l), temporal band block filtering (e and m), slice timing correction (f and n), motion correction (g and o), and all processes in series (h and p).

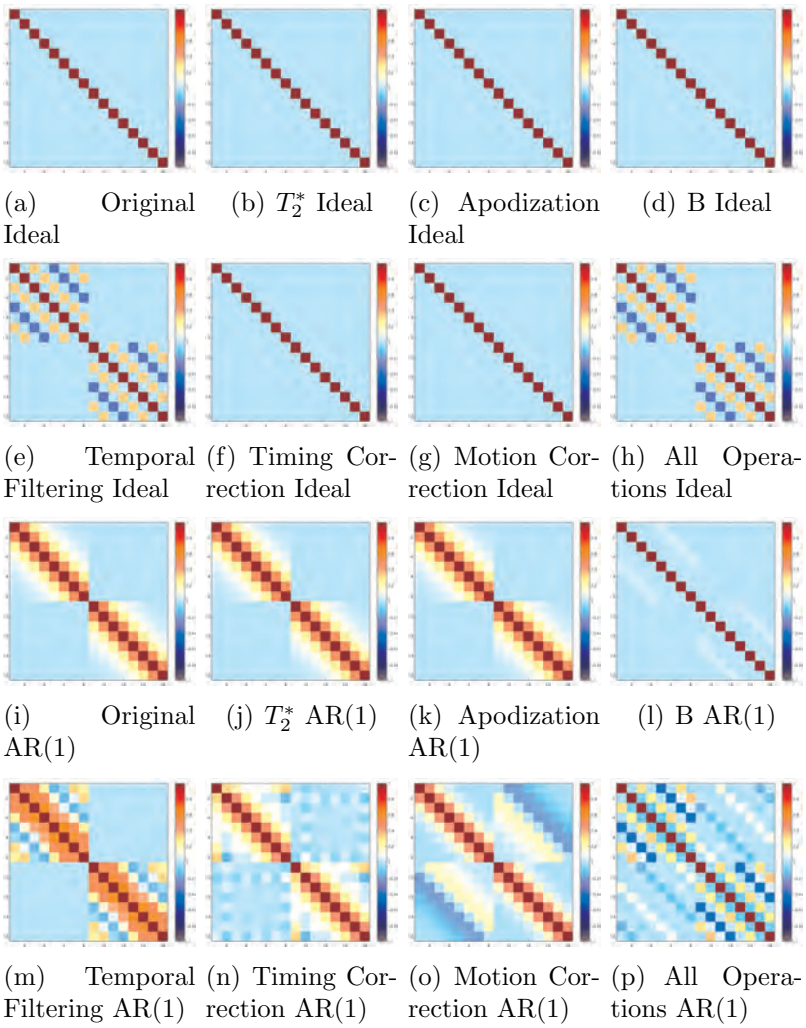

(a) Original Ideal (b) T_2^* Ideal (c) Apodization Ideal (d) B Ideal

(e) Temporal Filtering Ideal (f) Timing Correction Ideal (g) Motion Correction Ideal (h) All Operations Ideal

(i) Original AR(1) (j) T_2^* AR(1) (k) Apodization AR(1) (l) B AR(1)

(m) Temporal Filtering AR(1) (n) Timing Correction AR(1) (o) Motion Correction AR(1) (p) All Operations AR(1)

Figure 4.4: Voxel time series correlation matrices derived from the computed large correlation matrices. These matrices represent correlation matrices which would be considered in fMRI studies for adjusted regression coefficient estimates. Uncorrelated (ideal, a-h) and correlated (AR(1), i-p) original data were considered with no operations (a and i), intra-acquisition decay (b and j), k-space apodization (c and k), dynamic B-field correction (d and l), temporal band block filtering (e and m), slice timing correction (f and n), motion correction (g and o), and all processes in series (h and p).

4.3(l) are averages of the multiple time point correlation maps, represented by the diagonal blocks of the correlation matrices shown in Figures 4.2(d) and 4.2(l). Thus, correlations from time points with extreme B-field errors are attenuated by correlations from time points with more minor B-field errors. Voxel time series correlations, seen in Figures 4.4(d) and 4.4(l), are altered by the dynamic B-field errors only if non-identity correlations originally exist. If non-identity correlations do exist, the dynamic B-field errors yield altered correlations within the real and imaginary data as well as altered correlations between the real and imaginary data, as seen in Figures 4.2(l) and 4.4(l).

Temporal filtering does not alter spatial correlations as seen in Figures 4.2(e), 4.2(m), 4.3(e) and 4.3(m). This result is expected as the process is purely temporal. As seen in Figures 4.2(e), 4.2(m), 4.4(e) and 4.4(m), alterations arise in the voxel time series correlation matrix structure with temporal filtering, be there initial correlation or not. Such altered correlations arise from the convolution of the temporal filter kernel with the voxel time series. The process alters correlations within the real and imaginary data, but negligibly alters correlations between the real and imaginary data.

As with temporal filtering, the temporal process of slice timing correction does not significantly alter spatial correlations as seen in Figures 4.2(f), 4.2(n), 4.3(f) and 4.3(n). As seen in Figures 4.2(f), 4.2(n),4.4(f) and 4.4(n), the effect of the slice timing correction process depends upon the structure of the original voxel time series correlation matrix. If no correlation exists within the voxel time series, negligible alterations are observed in Figures 4.2(f) and 4.4(f) from the correlation matrix with

the time shifting process. This is analogous to line shifting to reduce Fourier ghosting, as described in Nencka et al. [2009]. As shown in that work, if no correlation is assumed between observations, this shifting can be mathematically shown to yield no change in correlation. However, if a correlation does exist, the sinc interpolation associated with the temporal shifting yields slightly altered correlation, as seen in Figures 4.2(n) and 4.4(n).

As modeled in these calculations, motion correction yields negligible alterations on the final correlation matrices. Figures 4.2(g), 4.2(o), 4.3(g), 4.3(o), 4.4(g), and 4.4(o) are nearly identity matrices. Off diagonal elements are zero within round off error. This is a result of the assumption of no spatial correlation in both calculations. If spatial correlation is assumed to be the identity matrix, the image shifting operator multiplied by its transpose is the identity matrix.

Finally, Figures 4.2(h), 4.2(p), 4.3(h), 4.3(p), 4.4(h), and 4.4(p) illustrate the effects of each of the described processes being considered in series. In each case, although the final correlation structure may appear to be dominated by individual processes, the correlation map is not a simple superposition of the individual processes. Herein lies an advantage of the described computational method. Exact correlation matrices resulting from a series of processing steps may be computationally determined without the need of empirical simulations.

4.4 Experimental Analysis

A representative phantom acquisition is considered in light of the above described framework.

4.4.1 Methods

To verify the performance of the operators, their application to phantom data was considered. Two previously published experimental data sets were considered [Nencka et al., 2009]. The data sets were acquired for a doped agar phantom with $T_2^* = 40.0$ ms on a 3.0 T General Electric Signa LX magnetic resonance imager. One slice of a $240 \times 240 \times 2.5$ mm^3 volume was imaged 1024 times, with a 96×96 acquisition matrix, effective echo planar echo spacing of 0.96 ms, minimum full k-space echo time of 50.0 ms, 2000.0 ms repetition time, and 250 kHz acquisition bandwidth. An 80 degree radio frequency pulse was used for excitation in one data set, and no excitation pulse was used in the other data set. The data set with the excitation follows standard acquisition parameters, and, to match the condition of pure noise in the above calculations with uncorrelated data, the data set with no excitation pulse was acquired.

Data were collected with a custom echo planar imaging pulse sequence, and reconstructed with locally developed software. With control of the entire acquisition and reconstruction pipeline, the confounds of unmodeled data processing are reduced. Nevertheless, some temporal filtering of the k-space acquisitions is performed to subsample the acquired 1 GHz samples to the collected 250 kHz samples. This processing may result in an autocorrelation of k-space observations, although such a correlation structure was not observed and is likely obscured by the noise in the experimental data.

Three navigator echoes of the center line of k-space were acquired to estimate error in the center frequency, and group delay offsets between odd and even k-space lines

[Nencka et al., 2008]. In the data acquired with an excitation pulse a group delay of 5.6 μs (1.4 k-space points) between odd and even lines was observed. Without correction of the group delay, severe Nyquist ghosting existed in the reconstructed data. This resulted in correlations between image voxels and ghost voxels. Correction of the group delay error greatly reduced the Nyquist ghost and resulting image-space correlations. The same group delay error was assumed on the data set acquired without an excitation pulse. No significant image-space correlations were apparent in the noise data before or after application of the group delay error correction, as previously described [Nencka et al., 2009]. The data acquired with no radio frequency excitation was found to exhibit uncorrelated normally distributed noise in space and time.

4.4.2 Results

Figure 4.5 includes the real and imaginary image-space correlations for the center pixel in the data with no excitation in Figures 4.5(a), and 4.5(b), with an excitation pulse in Figures 4.5(c), and 4.5(d). The results for the noise data acquired without an excitation pulse are consistent with the assumptions of the above calculations which included an identity correlation matrix. In the acquired data, the offdiagonal elements of the correlation matrix are near zero, with deviations from zero resulting from the thermal noise in the acquired data. Thus, the correlation maps for the center voxel in the real (Figure 4.5(a)) and imaginary (Figure 4.5(b)) data acquired with no radio frequency excitation show negligible correlations with other voxels.

The results for the data with an excitation pulse indicate correlation arising from an encoding anomaly described above. Slight fluctuations in the shim current over

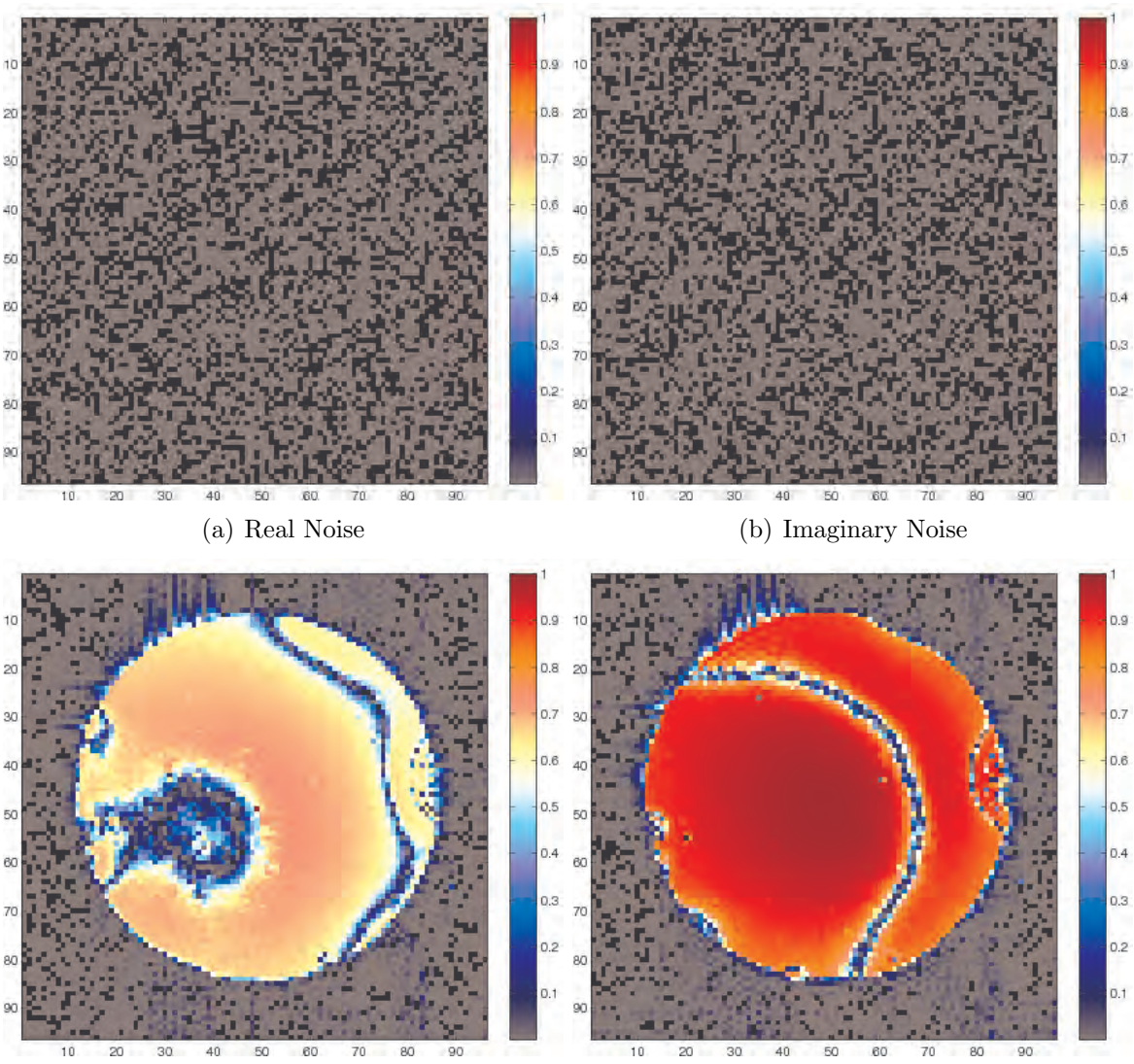

(a) Real Noise

(b) Imaginary Noise

(c) Real Excited

(d) Imaginary Excited

Figure 4.5: Unprocessed correlation maps for the center voxel in the real and imaginary data acquired with no radio frequency excitation (a and b) and with radio frequency excitation (c and d).

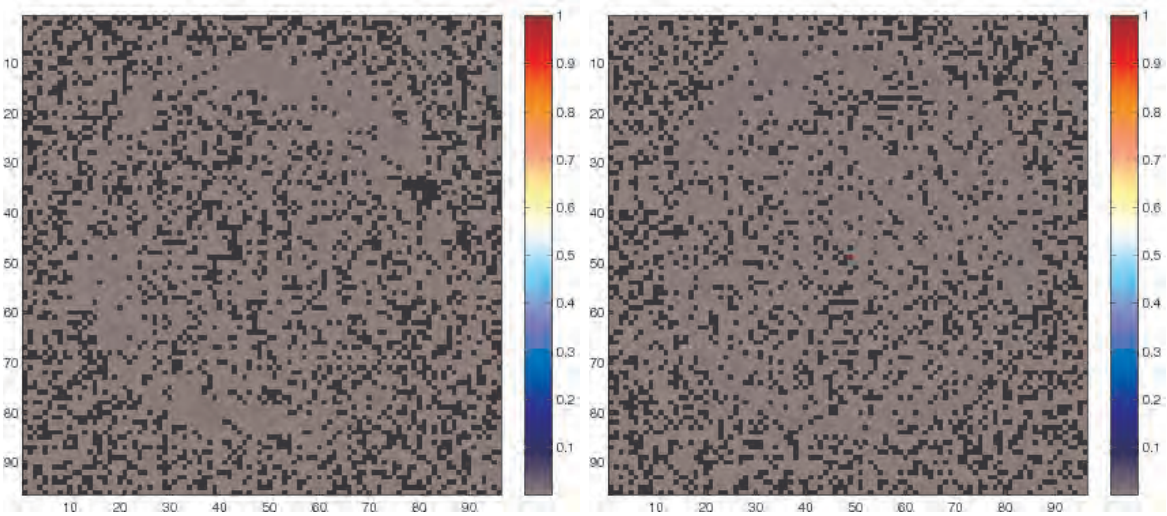

(a) Dynamic B Corrected Excited Real (b) Dynamic B Corrected Excited Imaginary

Figure 4.6: Processed correlation maps for the center voxel in the real and imaginary data acquired with radio frequency excitation. Artifactual global correlations observed in Figures 4.5(c) and 4.5(d) are corrected with the application of the dynamic B-field operator.

the time series acquisition lead to global correlations in the complex-valued data as the phase of the imaged isochromats varies in time. With the developed operators, the inverse B-field error operator may be applied to the data. With this dynamic B-field correction implemented, it can be seen in Figure 4.6 that the correlation may be markedly reduced in both the real (Figure 4.6(a)) and imaginary (Figure 4.6(b)) data.

Furthermore, if the constant phase model is fit to the acquired data the effects of the processing considerations are notable. In the above illustrated phantom data, the complex constant phase model was fit with a baseline and linear trend for the center voxel. Without consideration of the dynamically changing B-field, the regression coefficients were 31493 and 0.9166, with a residual standard deviation of 3488.99. When the dynamically changing B-field was included in the model as described above, the regression coefficients were calculated to be 31685 and 0.0370, and the residual standard deviation was greatly reduced to 571.436. Thus, it is clear through this experimental data that the consideration of corrupting effects in fcMRI and fMRI data models can yield a substantial change in computed statistical quantities. Furthermore, these results correspond to the results which were theoretically obtained in the above computational methods.

4.5 Discussion

In this work an analytic method has been described to model the effects of time series processing on observed image and time series correlations. This work advances previous work which modeled the effects of temporally constant image processing on observed voxel correlations [Nencka et al., 2009]. Linear operators have been con-

structed to reconstruct, spatially process, and temporally process vectors of acquired signal measurements. As the processing operations have been described as linear operators, their effects on means, variances, covariances and correlations of the acquired measurements may be computed through linear algebra. With the ability to calculate large covariance arrays for the acquired signal vector, we derived methods to extract the analytically useful individual voxel time series covariance matrices and image time series covariance matrices. Such matrices are useful for the consideration of functional connectivity studies and task related functional studies. In both cases, operators may be constructed to evaluate the effects of a physical process on acquired data, and inverse operators may be constructed to model the correction of the processes in the calculation of connectivity maps and regression coefficients.

Several processing operations were implemented as linear operators in light of this framework. Operators which are simple extensions of previously described operations [Nencka et al., 2009], including temporally constant apodization and temporally stable intra-acquisition decay, yield results which correspond to the previous findings. Purely temporal operators, including temporal filtering and slice timing correction, yield expected correlations in time series data. These operators have been shown to yield varying correlations based upon the assumed original correlation. Other operators which model spatial and temporal effects, including operators like dynamic B-field correction and motion correction, also yield varying correlations based upon the correlation structure assumed in the acquired data.

The developed operators are of very high dimensionality. An operator for a standard acquisition with an acquisition matrix of 64×64, 23 slices, and 125 repetitions

would be of dimension $23,552,000 \times 23,552,000$, and the calculation of the results from multiple operations in series would require the consideration of multiple non-sparse matrices of this dimensionality. When considering even floating point precision, the dimensionality of such calculations becomes prohibitive on most computers. We have addressed this issue by focusing upon a region of interest to lower the problem's dimensionality. Future studies are necessary to ease this restriction through advanced computational algorithms and memory management. In spite of the current restriction, the above results illustrate the utility of the analytic method.

Acquired phantom data was considered in light of the developed operators. Correlations within the reconstructed real and imaginary data were observed as a result of slightly varying shim fields. Such correlations led to artificial voxel correlations in functional connectivity maps in the complex-valued data, and improper regression coefficients and variance estimates in complex constant phase statistical modeling. By effectively applying the inverse of the dynamic B-field error operator, we showed that the global image correlations in the complex-valued data could be greatly reduced and that the regression coefficients of the constant phase model could be improved to greatly reduce residual error.

Although the above description only considered complex-valued data, the results can be used to compute correlations observed in the traditionally considered magnitude data. A conversion from the complex-valued covariance matrix to a magnitude squared covariance matrix has been previously described by Nencka et al. [2009]. The covariances in magnitude squared data asymptotically approach the covariances of magnitude data, and an analytical solution for the conversion from complex to mag-

nitude squared data was determined. In the previously published work, magnitude correlations were found to have similar structure to the complex-valued correlations.

With the described linear algebra framework, researchers may analytically prospectively evaluate the effects of a selected data processing pipeline. Thus, the optimal ordering of data processing steps may be determined. Also, researchers may prospectively evaluate an acceptable degree of processing based upon resulting covariance structures. Furthermore, with the developed linear operators and external measures of corrupting physical processes, inverse operators may be retrospectively calculated and applied to acquired data as a part of the statistical data model. Thus the presented work provides a foundation upon which an analytical evaluation of many processing strategies may be built.

Chapter 5

Temporal processing through dynamic B-field correction

With the linear framework for data processing developed, we return to the realm of processing experimental, human data. We have shown the improvement of the complex constant phase model in block designed fMRI studies with dynamic magnetic field correction processing elsewhere [Hahn et al., 2009]. In this chapter, we consider the processing step of dynamic magnetic field correction in fcMRI. We find that this processing technique can reduce global correlations as predicted by the developed linear model in Chapter 4. Specifically, in simulation and illustrative experimental human data, we show that dynamic magnetic field correction can reduce artifactual correlations between unrelated cortical regions and increase correlations between functionally related cortical regions.

5.1 Introduction

Functional connectivity magnetic resonance imaging (fcMRI) identifies functionally related cortical regions by finding regions of the brain with correlated blood oxygenation level dependent (BOLD) signals [Biswal et al., 1995]. As the BOLD signal is related to underlying neuronal activity [Logothetis, 2003], regions with temporally correlated BOLD signal are believed to have temporally correlated underlying neuronal activity. However, correlations from artefactual sources may additionally be introduced into the data. Such artefactual correlations are likely out of phase with, and may be at different frequencies than, the traditionally considered low frequency fluctuations in fcMRI. Thus, artefactual correlations can serve to both decrease correlations between functionally connected voxels, and increase correlations between functionally disconnected voxels.

Much work has yielded significant advances to the field in the last several years. External measures of periodic physiologic fluctuations have been used as nuisance regressors. The retrospective image-based correction of physiological motion artifacts (RETROICOR) method regresses signal correlated with respiration and cardiac motion from the data [Glover et al., 2000]. A refinement of the method additionally regresses the respiration volume per time (RVT) from the data [Birn et al., 2006]. Further methods have regressed the pulse rate from the data [Shmueli et al., 2007], and have dynamically shimmed the magnetic field based upon the phase of the respiratory cycle [Bianciardi et al., 2009]. All of these methods have shown improvement in the quality of the acquired data, with more localized regions of connectivity and higher correlation coefficients between connected regions. Each of these methods re-

lies upon the acquisition of physiologic data through external means, with data from a respiratory bellows, pulse oxymeter, and/or electrocardiograph being required. The use of such equipment introduces additional points of failure into the imaging system, increases subject preparation time, decreases subject comfort, and may slightly increase the risk of subject injury. Additionally, the requisite equipment is not available at all imaging sites.

Additional work has been performed to utilize other nuisance regressors. Signals from the global average of white matter, gray matter, and cerebrospinal fluid voxels have been regressed from the acquired data. Additionally, the global signal has been regressed from acquired time series. Such methods have proven empirically beneficial. However, recent work has questioned the validity of such processing, as it may shift the baseline of the observed correlations [Murphy et al., 2008].

The bulk of the processes which introduce artefactual correlations in fcMRI data have been modeled to produce magnetic field changes at the imaging plane [Pfeuffer et al., 2002]. It is based upon this assumption that we consider post-acquisition methods to account for dynamic magnetic field changes in post-processing. In this manuscript we examine correction of fcMRI data through phase nuisance regression [Menon, 2002], dynamic center frequency offset correction [Jesmanowicz et al., 1993, 1995], and dynamic B-field correction through temporal off-resonance alignment of single echo time series (TOAST)[Hahn et al., 2009]. We examine the methods through an extensive simulation, and we illustrate the methods in an acquired human resting state experiment.

5.2 Theory

We will first review the effects of magnetic field inhomogeneities on echo planar images, and then describe the considered correction methods of phase regression, center frequency offset correction, and dynamic field correction through TOAST.

The signal equation of gradient recalled echo, echo planar imaging is

$$\begin{aligned} s(t) &= \int\int \rho(x,y)\frac{\sin(\alpha)}{1-\cos(\alpha)e^{-\frac{TR}{T_1}}}\left(1-e^{-\frac{TR}{T_1(x,y)}}\right)e^{-\frac{t}{T_2^*(x,y)}}e^{i\gamma\Delta B(x,y)t} \\ &\quad \times e^{-i2\pi\left(x\int_0^t G_x(t')\mathrm{d}t'+y\int_0^t G_y(t')\mathrm{d}t'\right)}\mathrm{d}x\mathrm{d}y, \end{aligned}$$

where $s(t)$ is the signal acquired at time t, $\rho(x,y)$ is the proton spin density at the point (x,y), TR is the pulse sequence repetition time, $T_1(x,y)$ is the longitudinal relaxation rate at the point (x,y), $T_2^*(x,y)$ is the transverse relaxation rate at the point (x,y) (assuming exponential T_2^* decay), γ is the gyromagnetic ratio of the proton,$\Delta\ B(x,y)$ is the magnetic field error at point (x,y), $G_x(t')$ is the applied imaging magnetic field gradient in the x direction at time t', and $G_y(t')$ is the applied imaging gradient in the y direction. It is apparent from this that the magnetic field error can lead to a spatially varying phase error of $\gamma\Delta B(x,y)t$. Thus, each image space point yields a slightly different k-space trajectory due to the magnetic field inhomogeneity. As shown by Jezzard and Balaban [1995], this spatially varying k-space trajectory leads to warping of the reconstructed image. Because of the relatively low receiving bandwidth in the phase encoding direction of echo planar imaging, this warping may be considered to occur exclusively in the phase encoding direction, with

voxels being shifted by

$$\delta y = \gamma \Delta B(x, y) N_y eesp,$$

where δy is the shift in the phase encoding direction in units of voxels, N_y is the number of observations in the phase encoding direction, and $eesp$ is the effective echo spacing of the echo planar imaging readout. Thus, changes in the magnetic field over the course of a time series acquisition may vary the warping of the images over time. Even if the warping is on a sub-voxel scale, this may produce significant partial volume differences in imaged voxels and cause signal intensity variations which are correlated with the temporally varying magnetic field error.

Beyond the warping associated with magnetic field errors, intra-voxel dephasing may occur with strong magnetic field gradients. The signal from a voxel may be considered as the spatial integral of the magnetization isochromats which it contains,

$$\vec{M}_v = \int \int \int \vec{m}(x, y, z) \mathrm{d}x \mathrm{d}y \mathrm{d}z.$$

As isocromats at different locations have different resonant frequencies resulting from the spatially varying magnetic field, they may destructively interfere in the integration due to their varying phases. Substantial changes in the magnetic field over the course of a time series acquisition may thus alter the intra-voxel dephasing, and thus signal intensity. As with the geometric distortions associated with magnetic field changes, the intra-voxel dephasing associated with gross magnetic field changes may also cause temporal changes in the observed voxel signal which are correlated with the temporally varying magnetic field.

5.2.1 Phase Regression

Phase regression is a method which includes the acquired phase time series as a nuisance regressor on the observed magnitude time series. This method was originally developed to attenuate the contribution of the draining vasculature to BOLD functional studies [Menon, 2002] and has been more recently applied to attenuate the effects of out of field of view motion [Martin et al., 2004]. Magnetic field changes lead to alterations of the phase at an imaged location as$\Delta\ \phi = \gamma \Delta B\ TE$, assuming a temporally constant$\Delta\ B$ over the course of the echo planar readout. The phase regressor method models observed magnitude changes as a linear function of observed phase changes, assuming that above described magnetic field inhomogeneity effects on the magnitude images are linearly related to the change in phase resulting from the change in field, as shown in this equiation

$$m(t) = \alpha\phi(t) + m_0$$

where $m(t)$ is the magnitude observation of a voxel at time t, α is the regression coefficient of phase, $\phi(t)$ is the phase observation of a voxel at time t, and m_0 is the base magnitude of the voxel. To reduce the probability of phase wrap, the phase may be centered so that the magnitude is modeled as a function of deviations from the mean phase [Nencka and Rowe, 2007b],

$$\phi(t) = \arg\left(I(t) \sum_{i=1}^{n} \frac{I^*(i)}{\mathrm{abs}(I(i)n)} \right)$$

where $I(t)$ is the complex valued voxel observation at time point t, n is the number of observations in a time series, arg is a function which returns the angle of a complex-valued argument, abs is a function which returns the magnitude of a complex-valued argument, and * denotes complex conjugation. With the magnitude as a function of phase model fit, a phase-based estimate of magnitude is subtracted from each observed magnitude in an attempt to reduce magnetic field associated magnitude changes in the data,

$$m_c(t) = m(t) - \alpha\phi(t)$$

where $m_c(t)$ is the corrected magnitude time series. The corrected magnitude time series is then used for the analysis of the MRI data. As this method empirically relates magnitude fluctuations to the effects of magnetic field changes, both warping and dephasing effects may be addressed by this method.

5.2.2 Center Frequency Offset Correction

Although the imaging volume may be corrupted by quite intricate magnetic field inhomogeneities, barring extensive subject motion, temporal magnetic field changes resulting from minor out of field of view motion primarily affect the bulk magnetic field at the imaging slice. A global magnetic field shift leads to a global phase shift which manifests itself as a shift of the image in the phase encoding direction. Thus, two similar methods exist to correct global magnetic field shifts: rigid body registration [Jenkinson et al., 2002], and navigator echo correction [Jesmanowicz et al., 1993, 1995].

Rigid body registration is a step of fcMRI processing which is nearly universally

employed, as small scale physical translation and rotation of the subject's head generally occurs over the course of a several minute time series acquisition. Registration is performed by determining the shifts and rotations which minimize the difference between an acquired image volume and a reference volume.

If position or global magnetic field offsets change substantially over the course of a volume acquisition, volume-wise image registration will fail to obtain an ideal correction. With this limitation of registration, the estimation and correction of global field shifts utilizing navigator echoes is preferred. The negligible cost of acquiring navigator echoes is the increase of scan readout time of one to two milliseconds. If three navigator echoes are acquired, it can be shown that the center frequency offset is

$$\Delta\omega_0 = \frac{bw}{2} \arg\left(N_3 \cdot N_1^*\right)$$

whereΔ ω_0 is the center frequency offset, bw is the receiver bandwidth, arg is a function which returns the phase angle of the complex-valued argument, N_3 is the third navigator echo signal, and N_1^* is the complex conjugate of the first navigator echo signal. TheΔ ω_0 correction may be applied by demodulating the acquired k-space data with the determined frequency offset [Nencka et al., 2008]. As methods to account for global field shifts only correct image translations, signal changes associated with intra-voxel dephasing are not addressed by these methods.

5.2.3 Dynamic Magnetic Field Correction

Recently a method for correcting dynamic alterations of the magnetic field over the course of a time series acquisition has been developed [Hahn et al., 2009]. This

method is a refinement of the DORK method [Pfeuffer et al., 2002] as the phase is registered to a temporal mean of the phase images in place of a single reference image. This improves the effective signal-to-noise ratio of the fit magnetic field offset. The magnetic field offset may be calculated as

$$\Delta B(x,y) = \frac{\arg\left(I_t(x,y)\sum_{i=1}^{n}\frac{I_i^*(x,y)}{\mathrm{abs}(I_i(x,y))n}\right)}{\gamma TE}$$

where $I_t(x,y)$ is the complex-valued image value of point (x,y) at time t, * denotes complex conjugation, abs is a function which returns the magnitude of the complex-valued argument, and n is the number of time points in the acquired time series.

With the relative magnetic field error calculated, it may be corrected with a time segmented correction method Noll et al. [1991]. In the implemented correction method, each phase encoding line is treated as an individual time point acquired at the time when the $k_x = 0$ point is acquired. This process consists of four steps. The initial, warped, reconstructed image, $I(x,y)$, is point-wise multiplied with a phase map corresponding to the phase correction associated with the considered time segment, t,

$$I_{temp}(x,y) = I(x,y)e^{-i\gamma\Delta B(x,y)t}.$$

The corrected time segment image is then Fourier transformed to k-space, $K_{temp}(k_x,k_y)$,

$$K_{temp}(k_x,k_y) = \mathcal{F}\left(I_{temp}(x,y)\right).$$

The k-space line corresponding to the considered time segment is then extracted and

placed into a corrected k-space array, K_{cor},

$$K_{cor}(1 : N_{k_x}, t) = K_{temp}(1 : N_{k_x}, t),$$

where N_{k_x} is the number of frequency encoding points in the acquired data set. Finally, the described process is repeated for each time segment and the final image is reconstructed through a standard inverse Fourier transform to the corrected image, $I_{cor}(x, y)$,

$$I_{cor}(x, y) = \mathcal{F}^{-1}\left(K_{cor}(k_x, k_y)\right).$$

For dynamic B-field correction using the TOAST implementation, the above described method is applied to each image in the time series, effectively registering the phase, and thus image warping, to the time series mean image. As with the correction of the global frequency offset, this method does not account for intra-voxel dephasing associated with gross magnetic field changes.

5.3 Simulation

5.3.1 Methods

The above described methods were considered in a simulation. Simulated data were generated in Matlab, utilizing a simplified MRI signal equation:

$$s(k_x, k_y|t) = \int\int \rho(x, y) \exp\left(i\gamma\Delta B(x, y)t\right) \exp\left(-i2\pi(k_x x + k_y y)\right) \mathrm{d}x\mathrm{d}y,$$

where $\rho(x, y)$ is the ideal image-space representation at the point (x, y),$\Delta\ B(x, y)$ is the magnetic field error at the point (x, y), t is the time at which the k-space point (k_x, k_y) is acquired, and the k-space indexes are as traditionally defined as $k_x = \int_0^t G_x(t')\mathrm{d}t'$ and $k_y = \int_0^t G_y(t')\mathrm{d}t'$, with G_x and G_y being the applied imaging gradients in the x and y directions. This signal equation is simplified to incorporate intra-acquistion decay effects and T_1 effects in $\rho(x, y)$, as these effects do not significantly alter observed phase of the reconstructed image [Nencka et al., 2009].

The base 64×64 $\rho(x, y)$ map was a contrast modified Shepp-Logan phantom [Jain, 1989], with low frequency fluctuations added to the leftmost regions of interest shown in Figure 5.1. The low frequency fluctuation was modeled as a 0.02 Hz cosine wave with a 0.1 contrast ratio to the underlying $\rho(x, y)$ map. The low frequency fluctuation was added to the 5 voxel ROIs 1 and 2, shown in Figure 5.1. The$\Delta\ B(x, y)$ field was generated for each time point by randomly assigning values to the center 3×3 elements of a 64×64 element array, and scaling the maximum value of its Fourier transform to a B-field value of 100 nT. Three hundred time points were generated in a resting state time series for one simulation iteration. Simulated data was reconstructed through standard Fourier reconstruction [Rowe et al., 2007b]. The complex-valued, reconstructed simulated data was corrupted with normally distributed noise in the real and imaginary channels such that a magnitude temporal signal to noise ratio of 10 was achieved.

The data was then processed as experimental fcMRI data sets. Four copies of the data set were created with one left "unprocessed," one processed through phase nuisance regression, one processed through global center frequency correction, and

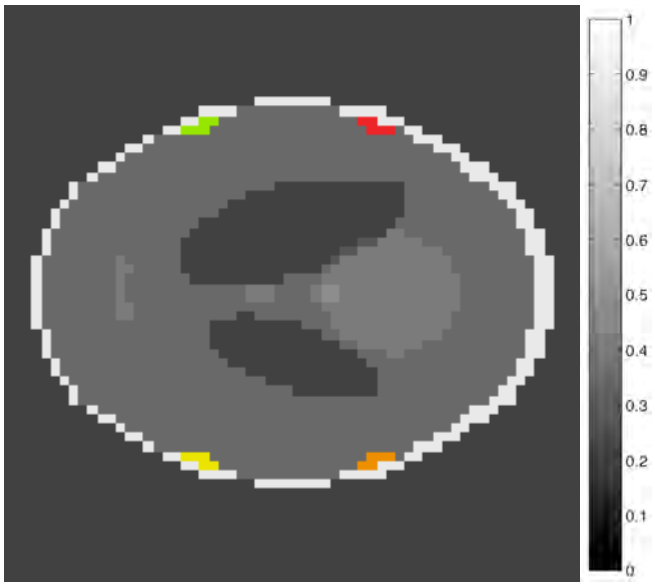

Figure 5.1: The base $\rho(x, y)$ map of the simulation with the considered regions of interest. The two leftmost regions of interest were modeled to be functionally connected with the inclusion of a low amplitude low frequency cosine signal. From the top left, the regions of interest are numbered 1 to 4 in a counter-clockwise direction.

one processed through TOAST. The processed data was written to AFNI data sets and further processed using that software suite [Cox, 1996]. The data were motion corrected and an ideal low frequency band pass filter was applied in temporal frequency space with cutoff frequencies of 0.005 Hz and 0.10 Hz. The average signal from each of the four regions of interest in Figure 5.1 was computed. The correlation matrix from the four averaged signals was computed and saved. This process was repeated for one hundred iterations. As cases of strong negative correlations and strong positive correlations between unconnected ROIs were found to result from simulated B-field changes, nonparametric Wilcoxon signed rank tests were performed for the differences of the absolute values of the correlation coefficients for each method.

5.3.2 Results

The average correlation matrices between the four regions of interest are shown in Figure 5.2. This figure includes the average correlation coefficients on the lower triangular portions. The upper triangular regions display the results of a nonparametric Lilliefors test for normality [Lilliefors, 1967]. Regions of interest which were determined to have correlation coefficients with their absolute values normally distributed with $p < 0.05$ are marked with 1, while those found to be not normally distributed are marked with 0. The non-normality of several sets of simulated correlation coefficients illustrates the need for the nonparametric Wilcoxon test when comparing the methods. The diagonals have the variances displayed. This data indicates that both phase regression and dynamic B-field correction favorably return the distribution of correlation coefficients to the normal distribution.

The mean pairwise differences of the absolute value of the correlation coefficients

for each method are shown in Figure 5.3. Along the lower triangular regions are the mean pairwise differences in the absolute values of the correlation coefficients for the listed methods. As stated previously, the absolute values of the correlation coefficients were used as a change in correlation between two simulated unconnected regions from 0.7 to 0.1 is equally beneficial as a change from -0.7 to -0.1. The upper triangular regions include the p-values determined from Wilcoxon [Wilcoxon, 1945] and paired t-tests [Student, 1908] for the differences between the absolute values of the correlation coefficients from the methods. As illustrated in Figure 5.2, the normality assumption of the t-test is violated in several ROI combinations when no processing and center frequency offset correction are performed, while the normality assumptions hold when phase regression and dynamic B-field correction are performed. Thus, the first listed p-values are more reliable when considering every combination except dynamic B-field correction and phase regression. In that case, the Wilcoxon test p-values may be set artificially high. Example correlation maps generated with the mean time series from ROI 2 for one iteration of the simulation are shown in Figure 5.4.

With no processing, shown in Figure 5.2(a), ROIs 1 and 2 have a relatively large correlation coefficient of 0.39, while ROIs 1 and 3 have a strong negative correlation of -0.73 caused by the modeled B-field correlations. As seen in Figure 5.4(a), the dynamically changing B-field yields dispersed regions of correlation, while correlation between ROIs 1 and 2 are present but weak.

The process of center frequency correction slightly alters the correlation coefficients in a favorable but non-significant manor as seen in Figures 5.2(b) and 5.3(a). Further, as seen in Figure 5.4(b), although the center frequency correction may re-

duce dispersed correlations and non-significantly increase correlations between the simulated connected regions, the method performs suboptimally.

Phase regression significantly improves computed correlations. As seen in Figures 5.2(c) and 5.3(b), the phase regressor method yields significantly increased correlation coefficients between simulated connected regions in ROIs 1 and 2. In functionally uncorrelated regions, the phase regressor method yields significantly reduced correlations between ROIs 1 and 3, ROIs 1 and 4, ROIs 2 and 3, and ROIs 2 and 4, and effectively unchanged correlation coefficients between ROIs 3 and 4. As seen in Figure 5.4(c), the spatial distribution of computed correlations more closely matches the simulated data, with clear correlations between ROIs 1 and 2, and no large regions of dispersed correlations as seen in the unprocessed and center frequency correlation maps. Further, as seen in Figure 5.3(f), the phase regressor method performs superiorly to the center frequency correction method, with similar results as when compared to the no processing case.

Dynamic B-field correction also significantly improves computed correlations. Figures 5.2(d) and 5.3(c) illustrate that the dynamic B-field correction method yields significantly increased correlation coefficients between the simulated connected regions in ROIs 1 and 2. Similar to the phase regressor method, the dynamic B-field correction method increased correlations between simulated connected regions and either decreased or left unchanged correlation coefficients between simulated unconnected regions. Furthermore, as with the phase regressor method, the dynamic B-field correction method proved superior to the center frequency correction method, as shown in Figure 5.3(d). When compared to the phase regressor method, the dynamic B-

field correction method yields significantly stronger correlations between simulated connected regions, while the two methods perform similarly in all other cases, as shown in Figure 5.3(e). The dynamic B-field correction method yields slight, but significant, decreases in the correlation coefficients between some simulated, unconnected regions. In the example data set, shown in Figure 5.4(d), the dynamic B-field correction method yields a correlation map which closely corresponds to the ideal generated correlation map.

5.4 Experimental Illustration

5.4.1 Methods

Experimental data was acquired on a General Electric 3.0 T system with a standard echo planar pulse sequence. Complex-valued data were reconstructed offline with custom software, utilizing three navigator echoes to correct the Nyquist ghost [Nencka et al., 2008]. Scan parameters included: 64×64 matrix, 19.2×19.2 cm^2 field of view, 11 slices, 3 mm slice thickness, 1 mm inter-slice gap, 125 kHz acquisition bandwidth, 26.0 ms echo time, 1000.0 ms repetition time, 45° flip angle, and 460 repetitions. The subject was at rest for the first 300 repetitions, and was visually cued to perform a block designed, bilateral finger tapping task for the final 160 repetitions. Functional regions of interest in the left and right motor cortices, as well as in the functionally unconnected parietal lobe were defined using the final 160 repetitions. Each region of interest consisted of five voxels and is shown in Figure 5.6(a). The data set was then truncated to the first 300 repetitions for the resting state analysis. Data was considered in 4 separate cases: no processing, center frequency offset correction,

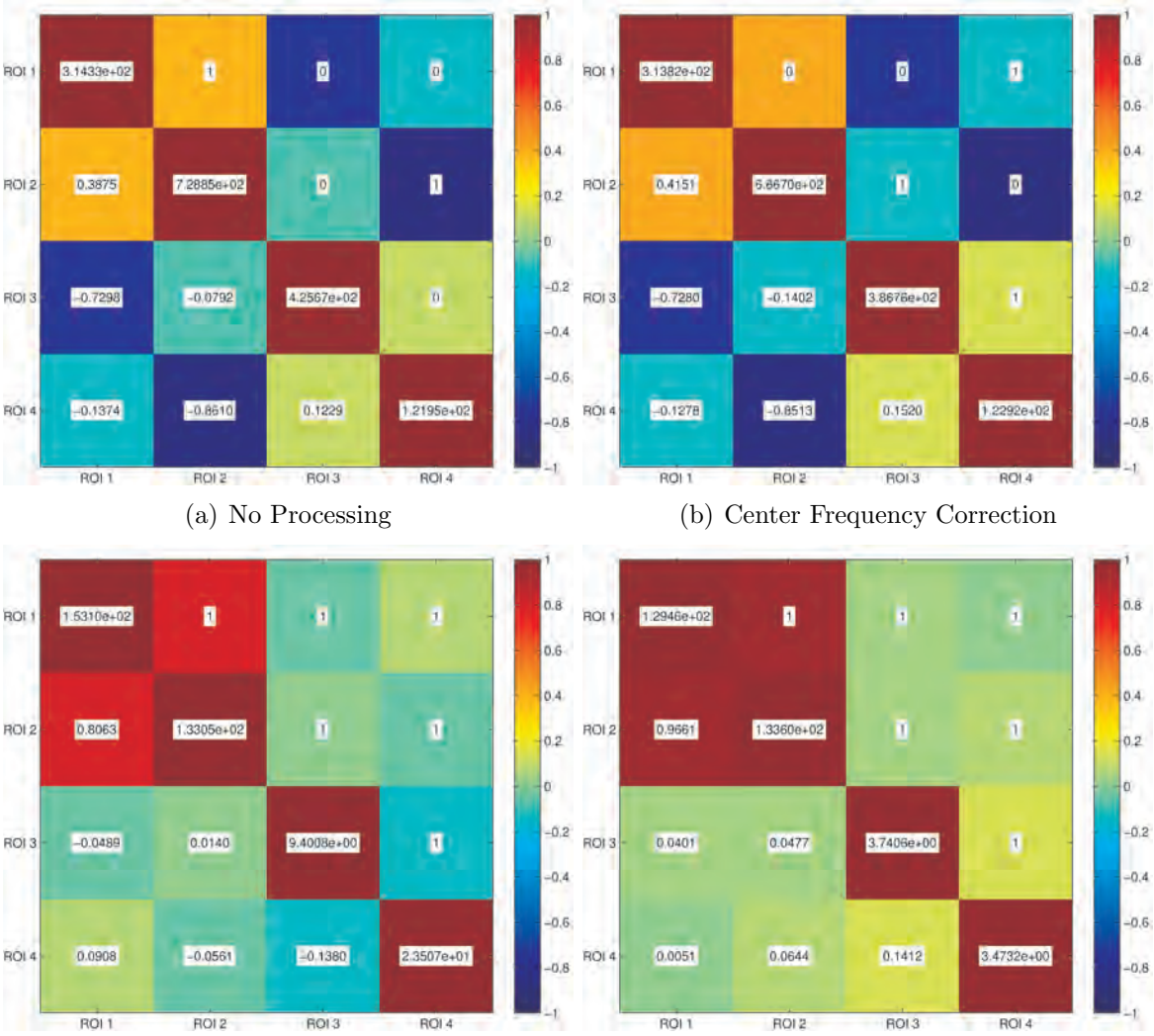

(a) No Processing (b) Center Frequency Correction

(c) Phase Regression (d) Dynamic B Correction

Figure 5.2: Correlation matrices between the four regions of interest. The matrices are shown with no processing (a), phase regression (b), global center frequency correction (c), and TOAST correction (d). Correlation coefficients are numerically shown on the lower triangular region of the symmetric matrices, and the results of a Lilliefors test for normality are shown on the upper triangular region, with 1 representing normality with $p < 0.05$. Computed variances are shown along the diagonal.

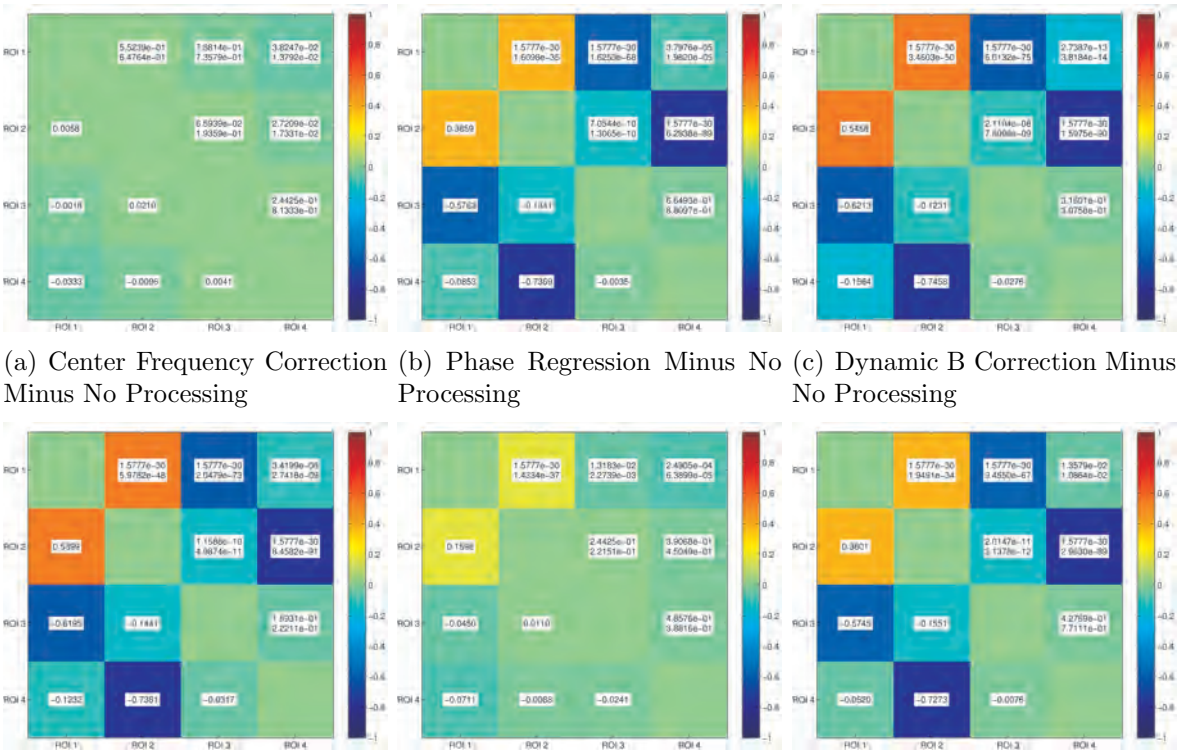

(a) Center Frequency Correction Minus No Processing

(b) Phase Regression Minus No Processing

(c) Dynamic B Correction Minus No Processing

(d) Dynamic B Correction Minus Center Frequency Correction

(e) Dynamic B Correction Minus Phase Regression

(f) Phase Regression Minus Center Frequency Correction

Figure 5.3: Difference between the correlation matrices under different processing conditions. Differences in correlation coefficients are shown in the lower triangular region of the symmetric matrices while p-values from non-parametric Wilcoxon tests (top) and paired t-tests (bottom) are shown in the upper triangular region. The diagonal values are identically zero. Differences between center frequency corrected and unprocessed data (a), phase regression processed and unprocessed data (b), dynamic B-field corrected and unprocessed data (c), dynamic B-field corrected and center frequency corrected data (d), dynamic B-field corrected and phase regression processed data (e), and phase regression processed and center frequency corrected data (f) are shown.

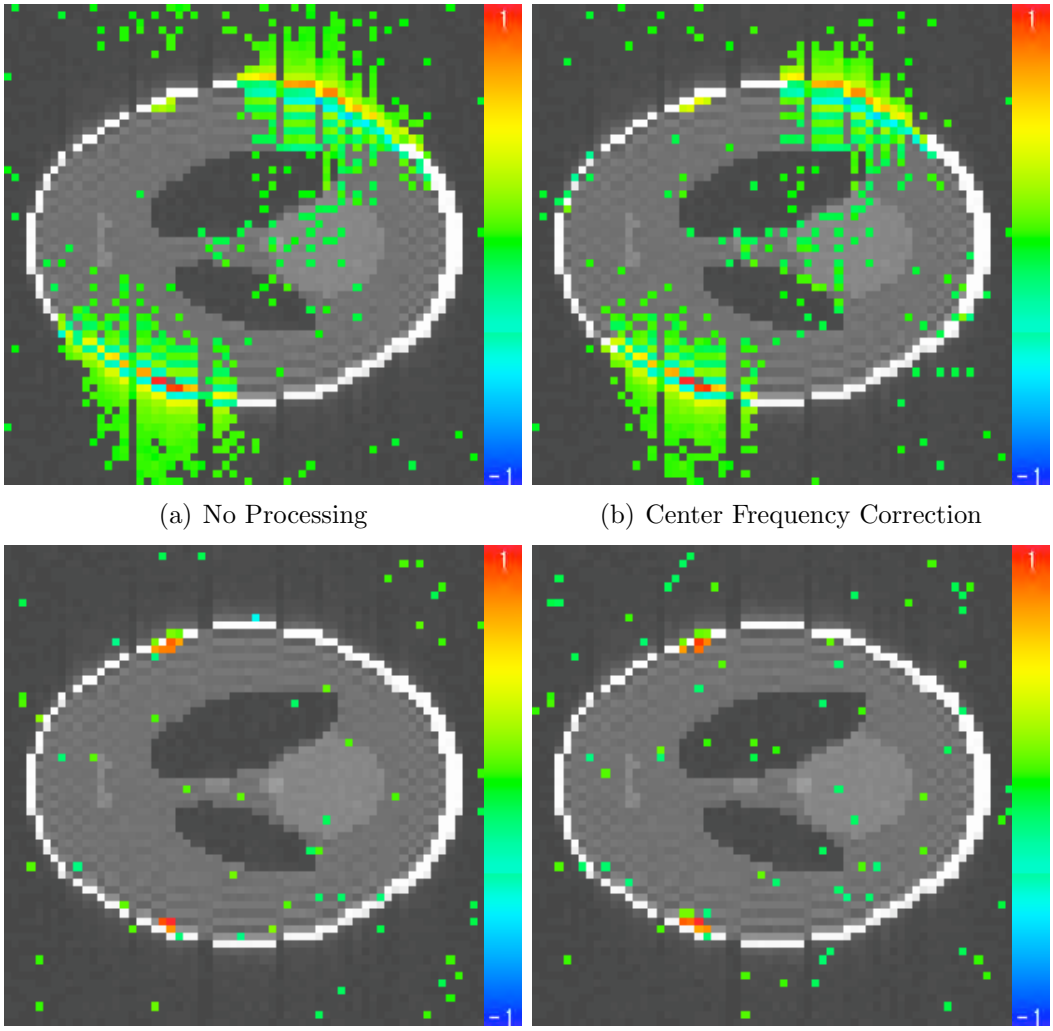

(a) No Processing (b) Center Frequency Correction

(c) Phase Regression (d) Dynamic B Correction

Figure 5.4: Correlation maps from a representative simulation iteration. Correlations with the mean time series of ROI 2 are shown with no processing (a), center frequency offset correction (b), phase regression (c), and dynamic B-field correction (d).

phase regression, and dynamic B-field correction. Slice timing correction was applied, utilizing temporal sinc interpolation to shift each slice to the same temporal phase. As in the above simulation, data were motion corrected and a low temporal frequency bandpass filter with cutoff frequencies of 0.005 Hz and 0.10 Hz was applied to each processed data set. No other processing was performed. Mean magnitude time series were extracted from each region of interest, and correlation coefficients between the mean time series were computed.

5.4.2 Results

Figure 5.5 contains the computed correlation matrices between the considered regions of interest under each of the processing conditions. The experimental results generally agree with the simulated results. The correlation between the functionally connected left and right motor cortices was found to be higher after processing with all methods. This suggests that physiologic correlation was obscured in part by shifts at other frequencies and phases associated with magnetic field changes. The correlation coefficients between the right motor cortex and the functionally unconnected parietal lobe were also found to decrease in magnitude with each of the processing methods. This suggests that the magnetic field modulation induced correlations between functionally unconnected regions that were corrected by these methods. As seen in Figures 5.5(c) and 5.5(d), the phase regressor method and dynamic B-field correction methods perform similarly to each other and superiorly to the cases of no processing and center frequency correction, as seen in Figures 5.5(a) and 5.5(b).

Figure 5.6 shows the computed correlation maps, thresholded at a correlation coefficient of 0.4, with center frequency offset correction in Figure 5.6(b), phase regression

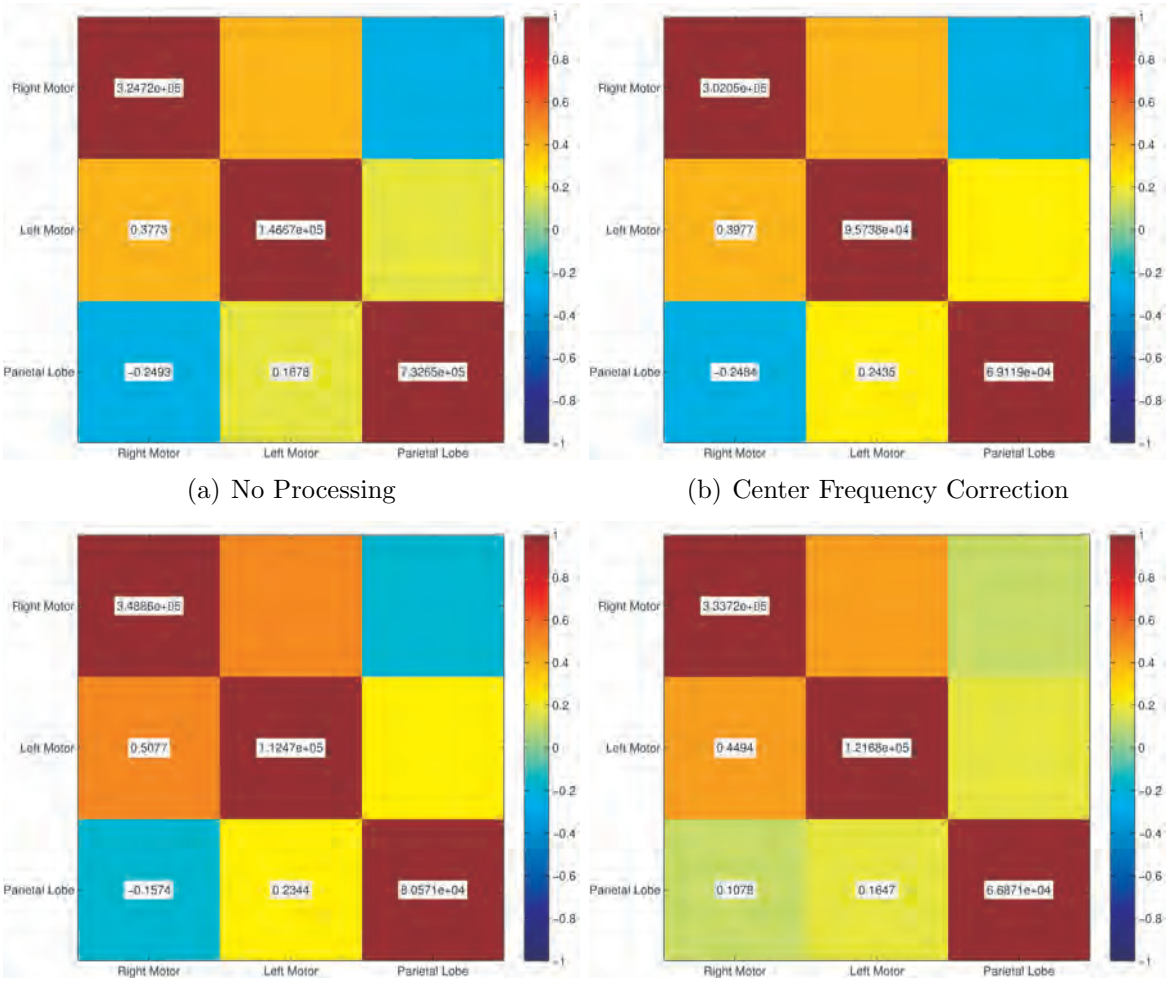

(a) No Processing

(b) Center Frequency Correction

(c) Phase Regression

(d) Dynamic B Correction

Figure 5.5: Computed correlation matrices from experimental data with no processing (a), center frequency offset correction (b), phase regression (c), and dynamic B-field correction through the TOAST method (d). Correlation coefficients are numerically shown on the lower triangular region of the symmetric matrices and the variances are shown on the diagonals of the matrices.

in Figure 5.6(c), and dynamic B-field correction in Figure 5.6(d). Results after no processing are not visually distinct from the center frequency offset corrected results, and are thus not shown. As found in the simulation, the correlation coefficients in the motor cortices are elevated after phase regression and dynamic B-field correction. Additionally, as found in the simulation, regions of correlation are substantially more focally located with dynamic B-field correction, and are generally found to be a subset of the center frequency offset corrected correlations.

5.5 Discussion

Much work has been performed over the past several years to improve the quality of fcMRI data. Such work has included the beneficial regression of several nuisance regressors from the acquired data, including cardiac and respiratory signals [Glover et al., 2000], the respiratory volume per time [Birn et al., 2006], and the pulse rate [Shmueli et al., 2007]. Regression of other nuisance regressors, including the global mean signal, have recently gained much attention with respect to the possible introduction of processing induced correlations [Murphy et al., 2008, Chang and Glover, 2009, Weissenbacher et al., 2009]. Additional recent work has examined the importance of individual nuisance regressors when considering spontaneous BOLD signal fluctuations and has used dynamic shimming to address temporally varying B-field inhomogeneities [Bianciardi et al., 2009]. In general, these studies have found that significant sources of non-neuronal correlations exist in fcMRI data and that accounting for non-neuronal sources of correlation yields higher correlations between functionally connected regions and reduced correlations between functionally unconnected regions.

One potential source of significant non-neuronal correlations in fcMRI data is

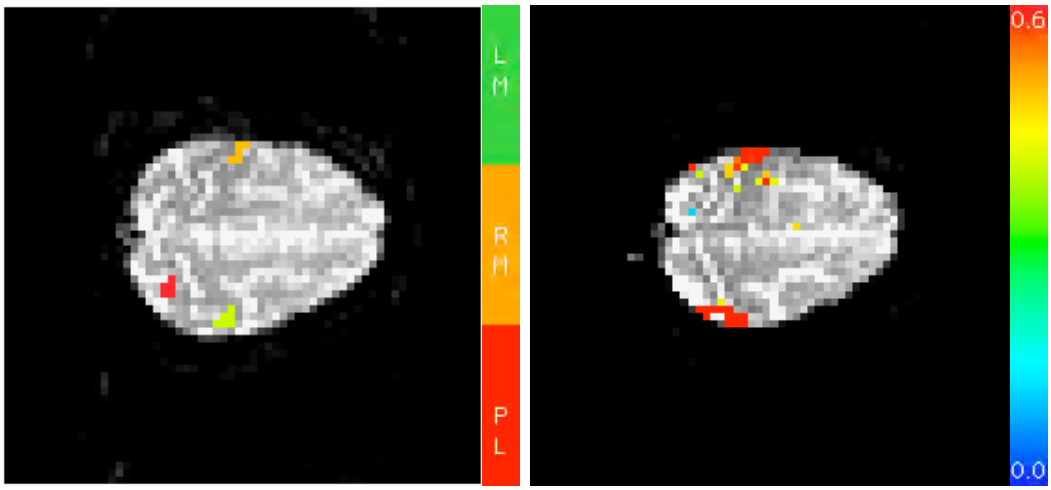

(a) Regions of Interest (b) Center Frequency Correction

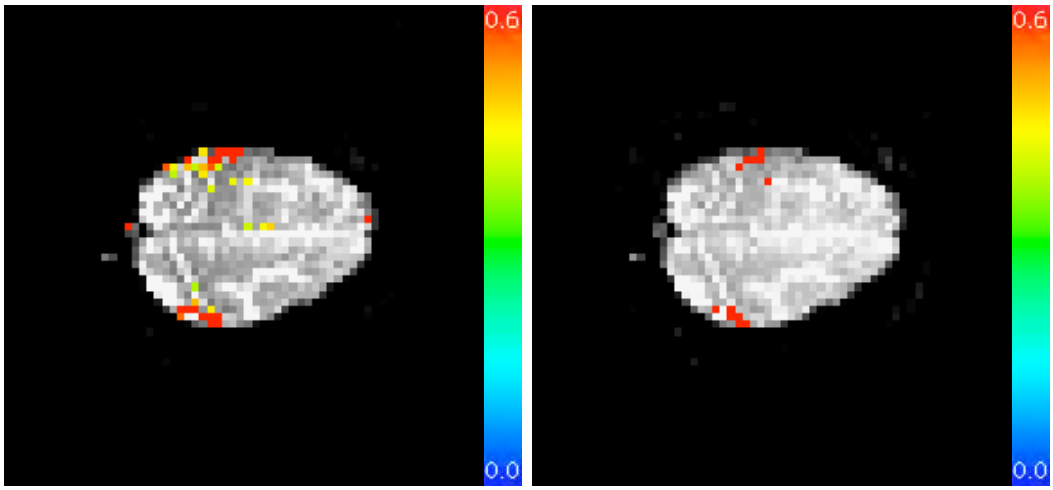

(c) Phase Regression (d) Dynamic B Correction

Figure 5.6: Illustrative experimental data. The regions of interest are shown in (a). The connectivity maps in a superior slices resulting from the mean time series from the right motor cortex region of interest with center frequency correction (b), phase regression (c), and dynamic B-field correction (d).

signal fluctuation associated with temporal magnetic field fluctuations. Such fluctuations may arise from out of field of view motion [Pfeuffer et al., 2002], and scanner hardware instability. Magnetic field fluctuations can lead to varying image warping [Jezzard and Balaban, 1995] and varying intra-voxel spin dephasing [Haacke et al., 1999]. Multiple methods have been described to directly, and indirectly, address the results of such magnetic field fluctuations. Some groups have modified pulse sequences to dynamically shim the imager based upon the phase of the subject's respiratory cycle [Bianciardi et al., 2009]. Other groups have utilized regressors associated with out of field of view motion, including the signal from a respiratory bellows [Glover et al., 2000, Birn et al., 2006].

In this study, we considered purely post-processing methods for addressing dynamic B-field fluctuations. These methods do not require the modification of the utilized pulse sequence, and they do not require the acquisition of physiologic data from external sources. Thus, the considered methods may be retrospectively applied to any acquired data set where the complex-valued data has been saved. The methods we studied included center frequency offset correction [Jesmanowicz et al., 1993, 1995], phase nuisance regression [Menon, 2002], and dynamic B-field correction [Hahn et al., 2009].

In simulated data and in illustrative experimental data, the results of standard motion correction and center frequency offset correction were found to yield non-significant improvements in artifacts associated with magnetic field fluctuations. As it has been previously described, although out of field of view motion can cause global field shifts in the imaging plane, more structure exists than a zeroth order correction

may address [Hahn et al., 2009].

Voxelwise phase regression and dynamic B-field correction methods proved to be superior in simulated and illustrative experimental data. These methods were found to reduce dispersed correlations associated with dynamic magnetic field alterations. Both processing techniques were found to yield significantly increased correlation coefficients between functionally connected regions and significantly reduced or unchanged correlation coefficients between functionally unconnected regions in simulated data. This observation was supported in the experimental data.

The dynamic B-field correction method was found to perform marginally better than the phase regressor method in the simulated data. While both methods yielded similar reduction in correlation between ideally uncorrelated regions, the dynamic B-field correction method yielded significantly higher correlation between simulated connected regions. Additionally, in the experimental data, the dynamic B-field correction method yielded a functional connectivity map which more focally localized correlated regions. With these results, and with the theoretical advantage of physically modeling the magnetic field rather than empirically modeling the magnitude as a function of phase, we find the dynamic B-field correction method to be the preferred method for post acquisition correction of magnetic field fluctuations in fcMRI data.

Additionally, the B-field correction method has been parameterized in other work as a linear operator which acts upon the acquired k-space data [Nencka et al., 2009]. With the ability to consider this processing as the result of a linear operator, processing induced alterations in the acquired data mean, covariance, and correlation structures from this process can be exactly computed. Furthermore, the framework

described by Nencka et al. [2009] allows one to consider the effects of a series of processing operations on acquired data. The results of this work highlight the need for researchers to consider the effects of the implemented processing pipeline on experimental data.

Further consideration of the dynamic B-field correction and phase regression methods is needed in future studies. As it has previously stated, the regression of physiologic waveforms from external monitoring equipment including respiratory bellows, electrocardiographs, and pulse oximeters have been been utilized to address the effects of out of field of view motion. It was not considered in this study if such physiologic nuisance regressors have the same action pathway as the considered data-based B-field fluctuation correction strategies. Studies with dynamic B-field shimming have found improvements with the inclusion of such nuisance regressors [Bianciardi et al., 2009], and thus, it may be found that the methods considered in this manuscript are complimentary to the use of such physiologic regressors.

Chapter 6

Conclusion

6.1 Summary of Presented Work

With the consideration of dynamic B-field correction in fcMRI in the last chapter, we have essentially returned to the issues discussed about the experimental data in Chapter 2. In that work, we attempted to use physiologic information, encoded in the phase of the MRI signal, to elucidate the vascular origin of the observed BOLD fMRI signal. We found that the phase regressor and the complex constant phase statistical methods perform differently when task related phase changes occur in acquired fMRI data. Specifically, we found the phase regressor method to exhibit a strong bias against finding voxels to be active when moderate to large task related phase changes occur, but to yield an inordinate number of false positives by over-correcting the magnitude signal when phase noise corrupted the regression. The complex constant phase method was, conversely, found to be overly sensitive to yielding false negatives. Any phase variation, task related or not, was found to increase the residual variance of the fit constant phase model, thereby reducing activation statistics.

Thus, while differences between the models were highlighted, the need for improved processing of complex-valued fMRI data to address the issue of phase stability was made abundantly clear.

In light of the need for improved complex-valued data processing, we set forth to develop a mathematical method for both processing complex-valued data, and analytically modeling the effects of such modeling. In Chapter 3, we extended our previous linear implementation of Fourier reconstruction to allow for temporally constant image processing. We considered standard reconstruction processes, utilized to ensure artifact free reconstructed images, as well as standard physical processes including intra-acquisition decay and static magnetic field inhomogeneities. The developed linear framework was implemented through simulation and shown, though the consideration of individual operators, to yield results which concur with previous findings. Furthermore, with the linear representation of processing operators, their effects on the mean, covariance, and correlation structures of the observed k-space data may be easily computed. The power of the framework was then further illustrated by analytically examining the effects of several processes, performed in series on one data set. The results illustrate that the bulk effect of multiple processes is more complicated than the summation of the results from the individual processes. Thus, with this framework, it is possible to linearly process complex-valued k-space data and keep track of the effects of the processing steps on the observed noise structure.

With the ability to model temporally constant processes on observed complex-valued data developed in Chapter 3, we extended the model to the temporal domain in Chapter 4. More common temporal processes like slice timing correction, motion

correction, and temporal filtering were implemented in this framework. Additionally, a dynamic B-field error correction operator was described, to address the issues observed in the experimental data of Chapter 2. Once again, the ability to model the effects of the processes on the mean, covariance, and correlation of the observed k-space data was illustrated, and the effects of multiple processes in series were found to differ from the simple summation of the individual processes. Furthermore, the processing modified covariance matrix was shown to contain the information necessary to compute voxel covariance matrices and image covariance matrices. Thus, the effects of time series processing may be included in statistical models for fMRI and fcMRI. One may effectively evaluate the ordering of implemented processing steps, and evaluate what level of processing yields an acceptable covariance structure.

In light of the operators described in Chapter 4, we moved on to consider fMRI and fcMRI data. In other work, we considered the effects of dynamic B-field correction in fMRI data, and found that it significantly improved the performance of complex data models [Hahn et al., 2009]. In the work in this dissertation, we chose to evaluate the effects of the dynamic B-field correction operator in simulated and acquired fcMRI data. We evaluated this operator, along with phase regression and center frequency offset correction, in data where temporally dynamic B-field fluctuations corrupt acquired fcMRI data. In simulation it was found that the dynamic B-field correction method and the phase regressor method both favorably improved fcMRI measurements. Specifically, it was found that the dynamic B-field correction method yielded significantly increased correlation coefficients between simulated connected regions when compared to all other methods, and reduced correlation coefficients between

simulated disconnected regions. Along with these results, the ability of the dynamic B-field correction method to be considered with the linear framework from Chapters 3 and 4, and the fact that the dynamic B-field correction method physically models the magnetic field rather than relying upon the empirical fit of magnitude as a function of phase, we believe that the dynamic B-field correction method is the preferred method for addressing B-field fluctuation artifacts in fcMRI data.

Thus, the body of work presented in this dissertation represents a progression of our technological development in our consideration of complex-valued data. We first considered complex-valued data to gain further insight into the nature of acquired fMRI data. We found that the complex-valued data suffered from artifacts which needed to be addressed through further processing of the data. We developed methods for applying common image processing techniques to acquired complex-valued data, and produced a framework through which the effects of the processes could be considered on the resulting statistical measurements. Further, we developed a method within this framework to address the effects of dynamically changing B-fields, which lead to the phase instability which corrupted the initially described data. We have since applied that method to fMRI and fcMRI data to find improvements in the consideration of the data.

6.2 Future Work

As with all developmental work, the results from our work indicate directions for future consideration.

The initial use of phase to address the macrovascular source of the BOLD signal may face additional challenges. As with all bulk magnetic susceptibility contrast

methods, the geometric orientation of the magnetic field perturbers can alter the magnetic fields which the observed spins experience. Thus, as stated in Chapter 2, the orientation of the vasculature may prevent the observation of phase shifts with activations in the draining vasculature. Further work needs to be done to consider this phenomenon. Recent work has suggested that the observed phase shift with fMRI may be from a bulk magnetic susceptibility effect of the vascularized tissue, rather than the vasculature itself [Feng et al., 2008, 2009]. Further biophysical modeling to elucidate the spatial regimes of phase contrast in fMRI is needed. Specifically, the phase hemodynamic response function must be studied both at voxel and sub-voxel spatial scales so that complex-data models may appropriately model the functional phase response.

As mentioned in Chapter 3, the dimensionality of image processing operators can grow to be prohibitive, even when considering moderately sized data sets. The described spatial operators are well represented as sparse matrices, but the combination of spatial and temporal processes described in Chapter 4 yields matrices with high rank. Thus, the issue of high dimensional matrices becomes more significant when considering linear temporal and spatial processes. At this point, we have addressed the problem by focusing upon a small region of interest when considering the operators, ignoring the possible long spatial distance effects of the operations. Further work in the field of computer science is needed to lift this dimensionality restriction. As it currently stands, the large dimensionality of the considered operators lead to memory management issues, as well as computational time restrictions. The optimization of the algorithms utilizing the described linear framework to use general

purpose graphical processing unit computations and to parallelize the calculations across multiple nodes may bring the theoretical framework to the realm of utility for clinical researchers.

Furthermore, several operations are applied to acquired data in processing steps which are not described in Chapters 3 and 4. Specifically, parallel acquisition image reconstruction techniques are well suited to consideration in light of the described framework. In such cases, correlations exist between the signals acquired from the multiple channels, and the processing effects on those non-identity correlations could prove to be significant and interesting.

Additionally, the processing techniques described in Chapter 5 to reduce artifactual correlations associated with magnetic field fluctuations must be considered in series with other, now common, nuisance regression techniques. As the methods aim to alleviate artifacts from similar processes, the colinearity between the B-field corrections and the other regressors may be quite high, making their serial use less effective. However, as dynamic B-field shimming has suggested, the different techniques may address artifactual correlations through different action mechanisms [Bianciardi et al., 2009].

Finally, our work in this dissertation advances the general goal of our lab. We have been seeking to work back from the statistical modeling of reconstructed magnitude images in fMRI to the physical processes which yield the functional BOLD contrast. Lab members have considered the statistical thresholding of activation statistics [Logan and Rowe, 2004], and have worked to develop statistical models of the complex valued data [Rowe and Logan, 2004, 2005, Rowe, 2005a]. We have de-

veloped a mathematical framework to include the effects of necessary data processing upon the acquired data, including image reconstruction, in the statistical evaluation of fMRI and fcMRI data. Additionally, we have worked to obtain further information through the modeling of the complex valued data, as we have used the complex constant phase method in attempts to attenuate delocalized BOLD activations. Our continuing aim is to work farther back in the data acquisition process, accounting for other acquisition based processes on the acquired data. The ultimate goal is to develop the statistical model so that activation statistics and correlation studies may be described in terms of physical parameters, including changes in T_2^*, or changes in blood oxygenation, flow, and volume, while including the effects of each data processing step along the way.

Appendix A

Menon's Complex Phase Regressor (PR) Method

Unlike the traditional magnitude-only method, a two step method developed by Menon [2002] utilizes phase information in an attempt to bias against magnitude activations in voxels with associated task related phase changes. Using the standard Fourier reconstruction method, complex-valued images are formed and are converted into unique pairs of magnitude and phase images with the following standard transformations for magnitude and phase:

$$m_t = \sqrt{r_t^2 + i_t^2} \ , \tag{A.0.1}$$

$$\phi_t = \arctan\left(\frac{i_t}{r_t}\right). \tag{A.0.2}$$

In these equations, m_t is the calculated magnitude of the t^{th} time point of a voxel time series, ϕ_t is the calculated phase of the t^{th} time point, and r_t and i_t are

the reconstructed real and imaginary observations at the t^{th} time point, respectively. The phase and magnitude time series for each voxel are then considered. To reduce task related changes in the magnitude in voxels with task related phase changes, a least squares linear regression of magnitude values as a function of phase is computed for each voxel to create an estimated magnitude image:

$$m_{est} = \hat{B} + \hat{A}\phi \tag{A.0.3}$$

$$\hat{A} = \frac{-(S_{\phi\phi} - \frac{\hat{\sigma}_\phi^2}{\hat{\sigma}_m^2} S_{mm}) + \sqrt{\left(S_{\phi\phi} - \frac{\hat{\sigma}_\phi^2}{\hat{\sigma}_m^2} S_{mm}\right)^2 + 4\frac{\hat{\sigma}_\phi^2}{\hat{\sigma}_m^2} S_{\phi m}^2}}{2\frac{\hat{\sigma}_\phi^2}{\hat{\sigma}_m^2} S_{\phi m}} \tag{A.0.4}$$

$$\hat{B} = \bar{m} - \hat{A}\bar{\phi} \tag{A.0.5}$$

where $\bar{m}$ is the arithmetic mean of the magnitude time series, and $\bar{\phi}$, $S_{\phi\phi}$, S_{mm}, and $S_{\phi m}$ are defined to be:

$$\bar{\phi} = \arctan\left(\frac{\frac{1}{n}\sum_{t=1}^{n}\sin\phi_t}{\frac{1}{n}\sum_{t=1}^{n}\cos\phi_t}\right) \quad \text{(A.0.6)}$$

$$\Delta\phi = \arctan\left(\frac{\Im\left(\frac{r_t+i_t}{\bar{m}\exp i*\bar{\phi}}\right)}{\Re\left(\frac{r_t+i_t}{\bar{m}\exp i*\bar{\phi}}\right)}\right) \quad \text{(A.0.7)}$$

$$S_{\phi\phi} = \sum_{t=1}^{n}(\Delta\phi)^2 \quad \text{(A.0.8)}$$

$$S_{mm} = \sum_{t=1}^{n}(m_t-\bar{m})^2 \quad \text{(A.0.9)}$$

$$S_{\phi m} = \sum_{t=1}^{n}(\Delta\phi)(m_t-\bar{m}). \quad \text{(A.0.10)}$$

In these formulae, $\hat{B}$ and $\hat{A}$ are determined through a least squares regression with normally distributed errors in both m and ϕ [Casella and Berger, 1990]. The $\Re$ and $\Im$ symbols indicate taking the real and imaginary components of the complex-valued element. The estimated variances, $\hat{\sigma}_\phi^2$ and $\hat{\sigma}_m^2$, are determined individually for each voxel by taking the FT of the time series, setting the task frequency and its first four harmonics to zero, and then calculating the variance of the filtered time series after taking the IFT [Menon, 2002]. Because the phase time series can wrap around, circular statistics were implemented to determine the average phase, $\bar{\phi}$, and difference in phase,$\Delta\ \phi$, without the need to unwrap the phase time series [Jammalamadaka and SenGupta, 2001]. Using the phase image time series, estimated magnitude image time series are created using the above described linear regression. The phase estimated magnitude ($m_{\phi t} = \hat{A}\phi_t$) is then subtracted from the observed magnitude, ideally leaving corrected magnitude time series with no magnitude changes in vox-

els with TRPCs. The same general linear model used in the magnitude activation method is then used to compute cortical activations for the corrected magnitude time series. This model was introduced with an empirical linear fit of the phase's effect on magnitude observations. However, it is not clear that a linear fit is optimal, as some data suggests a more complicated relationship [Klassen and Menon, 2005].

Appendix B

Rowe and Logan's Complex Constant Phase (CP) Method

The Rowe-Logan complex constant phase method [Rowe and Logan, 2004] is different from the previous method in that it directly utilizes the information in the complex-valued reconstructed images to compute magnitude activations. This both avoids the large signal-to-noise ratio assumption of normally distributed noise for the Ricean noise in the magnitude-only images, and utilizes twice as many data points to compute the maximum likelihood estimators, leading to a theoretically improved power of determining true activations [Rowe, 2005b]. The model for data in this case is:

$$\begin{pmatrix} R \\ I \end{pmatrix} = \begin{pmatrix} X & 0 \\ 0 & X \end{pmatrix} \begin{pmatrix} \beta\cos\theta \\ \beta\sin\theta \end{pmatrix} + \eta,\eta \qquad \sim N(0,\sigma^2 I_{2n}). \tag{B.0.1}$$

In this equation, the left hand side is the vector of observed real data ($R = (r_1...r_n)'$) stacked on top of the vector of imaginary data ($I = (i_1...i_n)'$); X is the same design matrix as in the magnitude-only activation method; β is the same vector of regression coefficients as in the magnitude-only activation method; and θ is the fixed but unknown phase angle of the data which is estimated on a voxel-wise basis. As with the other methods, hypothesis tests which consider the value of β_2 are used to determine the activation statistics for each voxel. In this activation method, the phase angle θ is assumed to be temporally constant, and is thus represented by its maximum likelihood estimator in both the unrestricted alternative hypothesis and in the restricted null hypothesis. The maximum likelihood estimators for the unrestricted case, $\beta_2 \neq 0$, can be shown to be:

$$\widehat{\beta} = \widehat{\beta}_R \cos\widehat{\theta} + \widehat{\beta}_I \sin\widehat{\theta} \tag{B.0.2}$$

$$\widehat{\sigma}^2 = \frac{1}{2n}\left[\begin{pmatrix} R \\ I \end{pmatrix} - \begin{pmatrix} X\widehat{\beta}\cos\widehat{\theta} \\ X\widehat{\beta}\sin\widehat{\theta} \end{pmatrix}\right]' \left[\begin{pmatrix} R \\ I \end{pmatrix} - \begin{pmatrix} X\widehat{\beta}\cos\widehat{\theta} \\ X\widehat{\beta}\sin\widehat{\theta} \end{pmatrix}\right] \tag{B.0.3}$$

$$\widehat{\theta} = \frac{1}{2}\arctan\left[\frac{\widehat{\beta}_I'(X'X)\widehat{\beta}_R}{\left(\widehat{\beta}_R'(X'X)\widehat{\beta}_R - \widehat{\beta}_I'(X'X)\widehat{\beta}_I\right)/2}\right] \tag{B.0.4}$$

$$\widehat{\beta}_R = (X'X)^{-1}X_R'R \tag{B.0.5}$$

$$\widehat{\beta}_I = (X'X)^{-1}X_I'I. \tag{B.0.6}$$

The maximum likelihood estimators for the null hypothesis, $\beta_2 = 0$, or more generally $C\beta = 0$ with $C = (0, 0, 1)$ in this case, can be shown to be:

$$\Psi = (X'X)^{-1}\left[(X'X) - C'(C(X'X)^{-1}C')^{-1}C\right] \quad \text{(B.0.7)}$$

$$\widetilde{\beta} = \Psi\left[\widehat{\beta}_R\cos\widetilde{\theta} + \widehat{\beta}_I\sin\widetilde{\theta}\right] + (X'X)^{-1}C'\left[C(X'X)^{-1}C'\right]^{-1} \quad \text{(B.0.8)}$$

$$\widetilde{\sigma}^2 = \frac{1}{2n}\left[\begin{pmatrix} R \\ I \end{pmatrix} - \begin{pmatrix} X\widetilde{\beta}\cos\widetilde{\theta} \\ X\widetilde{\beta}\sin\widetilde{\theta} \end{pmatrix}\right]'\left[\begin{pmatrix} R \\ I \end{pmatrix} - \begin{pmatrix} X\widetilde{\beta}\cos\widetilde{\theta} \\ X\widetilde{\beta}\sin\widetilde{\theta} \end{pmatrix}\right] \quad \text{(B.0.9)}$$

$$\widetilde{\theta} = \frac{1}{2}\arctan\left[\frac{\widehat{\beta}_R'\Psi(X'X)\widehat{\beta}_I}{\left(\widehat{\beta}_R'\Psi(X'X)\widehat{\beta}_R - \widehat{\beta}_I'\Psi(X'X)\widehat{\beta}_I\right)/2}\right]. \quad \text{(B.0.10)}$$

As with the magnitude-only method, these maximum likelihood estimators can be used to test for significance of β_2 utilizing a likelihood ratio statistic with a large sample χ^2_d distribution under the null hypothesis, where d is once again the full row rank of C or the degrees of freedom:

$$-2\log\lambda_{CP} = n\log\frac{\widehat{\sigma}^2}{\widetilde{\sigma}^2}. \quad \text{(B.0.11)}$$

In this case, the χ^2 statistics can be manipulated to approach F or t statistics asymptotically for large samples. In this paper, large sample z-statistics are considered through the transformation of:

$$Z_{CP} = \text{sign}(C\hat{\beta})\sqrt{-2\log(\lambda_{CP})} \quad \text{(B.0.12)}$$

The activation statistics can then be thresholded to determine activations.

This complex constant phase method has also been argued to remove voxels de-

clared active as the result of TRPCs associated with draining veins [Nencka and Rowe, 2005, Rowe and Nencka, 2006]. While not explicitly relying upon a mathematical model of the phase behavior, this method assumes that θ is fixed to be temporally constant but unknown in each voxel, while varying from voxel-to-voxel. By assuming that the angle θ is represented by its maximum likelihood estimator for the voxel time series, a constant phase condition is assumed in the individual voxel time series. When this condition is not met as a voxel exhibits task related phase changes, the assumptions of the model are not satisfied, making the fit constant phase suboptimal. This results in larger residual variances in the model, $\hat{\sigma}^2$, and thus lower activation statistics. It is this reduced fit, not the explicit modeling of the phase response, that has been claimed to reduce draining vein contributions. Therefore, the complex constant phase activation method theoretically biases against declaring such voxels active. It should be noted that allowing the angle θ to be estimated at each time point has been shown to remove any phase dependence in the model, yielding the magnitude-only activation method [Rowe and Logan, 2005]. Further, in a more general activation method the phase angle θ_t has been modeled in a linear fashion along with the magnitude [Rowe, 2005a].

Appendix C

Magnitude Squared Covariance

Consider two magnitude squared variables

$$\begin{aligned} y_1 &= x_{1R}^2 + x_{1I}^2, \\ y_2 &= x_{2R}^2 + x_{2I}^2, \end{aligned} \tag{C.0.1}$$

where x_{1R} and x_{2R} are the real components of the first and second observations while x_{1I} and x_{2I} are the imaginary components. For the sake of this derivation, let

$$\begin{aligned} \mathrm{E}(x_{1R}) &= \rho_1 \cos\theta_1, \quad \mathrm{var}(x_{1R}) = \sigma_{1R}^2, \quad \mathrm{cor}(x_{1R}, x_{2I}) = \Gamma_{RI}, \\ \mathrm{E}(x_{1I}) &= \rho_1 \sin\theta_1, \quad \mathrm{var}(x_{1I}) = \sigma_{1I}^2, \quad \mathrm{cor}(x_{1I}, x_{2I}) = \Gamma_{II}, \\ \mathrm{E}(x_{2R}) &= \rho_2 \cos\theta_2, \quad \mathrm{var}(x_{2R}) = \sigma_{2R}^2, \quad \mathrm{cor}(x_{1R}, x_{2R}) = \Gamma_{RR}, \\ \mathrm{E}(x_{2I}) &= \rho_2 \sin\theta_2, \quad \mathrm{var}(x_{2I}) = \sigma_{2I}^2, \quad \mathrm{cor}(x_{1I}, x_{2R}) = \Gamma_{IR}, \\ & \qquad\qquad\qquad\qquad\quad \mathrm{cor}(x_{1R}, x_{1I}) = \Gamma_{1}, \\ & \qquad\qquad\qquad\qquad\quad \mathrm{cor}(x_{2R}, x_{1I}) = \Gamma_{2}, \end{aligned} \tag{C.0.2}$$

where ρ represents an observation's magnitude and θ represents an observation's phase. The magnitude and phase may be obtained from the reconstructed image. Note that the Γ and variance values may be obtained from the complex correlation matrix.

The covariance between the magnitude squared variables assuming normally distributed noise is thus:

$$\begin{aligned}
\mathrm{cov}(y_1, y_2) &= \mathrm{E}(y_1 y_2) - \mathrm{E}(y_1)\mathrm{E}(y_2) \\
&= E(x_{1R}^2 x_{2R}^2) + E(x_{1R}^2 x_{2I}^2) + E(x_{1I}^2 x_{2R}^2) + E(x_{1I}^2 x_{2I}^2) - \\
&\quad \left(E(x_{1R}^2) + E_(x_{1I}^2)\right)\left(E(x_{2R}^2) + E(x_{2I}^2)\right) \\
&= 2\left(\Gamma_{RR}^2\sigma_{1R}^2\sigma_{2R}^2 + \Gamma_{RI}^2\sigma_{1R}^2\sigma_{2I}^2 + \Gamma_{IR}^2\sigma_{1I}^2\sigma_{2R}^2 + \Gamma_{II}^2\sigma_{1I}^2\sigma_{2I}^2\right) + \\
&\quad 4\left(\Gamma_{RR}\sigma_{1R}\sigma_{2R}\rho_1\cos(\theta_1)\rho_2\cos(\theta_2) + \right. \\
&\qquad \Gamma_{RI}\sigma_{1R}\sigma_{2I}\rho_1\cos(\theta_1)\rho_2\sin(\theta_2) + \\
&\qquad \Gamma_{IR}\sigma_{1I}\sigma_{2R}\rho_1\sin(\theta_1)\rho_2\cos(\theta_2) + \\
&\qquad \left.\Gamma_{II}\sigma_{1I}\sigma_{2I}\rho_1\sin(\theta_1)\rho_2\sin(\theta_2)\right).
\end{aligned} \tag{C.0.3}$$

By letting $x_1 = (x_{1R}, x_{1I})'$, $x_2 = (x_{2R}, x_{2I})'$, $\mathrm{E}(x_1) = \mu_1$, $\mathrm{E}(x_2) = \mu_2$, $\mathrm{cov}(x_1) = \Sigma_1$, $\mathrm{cov}(x_2) = \Sigma_2$, and $\mathrm{cov}(x_1, x_2) = \Sigma_{12}$, one can compactly write:

$$\begin{aligned}
\mathrm{E}(y_j) &= \mathrm{tr}(\Sigma_j) + \mu_j'\mu_j, & j = 1, 2, \\
\mathrm{var}(y_j) &= 2\mathrm{tr}(\Sigma_j'\Sigma_j) + 4\mu_j'\Sigma_j\mu_j, & j = 1, 2, \\
\mathrm{cov}(y_1, y_2) &= 2\mathrm{tr}(\Sigma_{12}'\Sigma_{12}) + 4\mu_1'\Sigma_{12}\mu_2,
\end{aligned} \tag{C.0.4}$$

where $\mathrm{tr}(\cdot)$ denotes the trace operation.

Appendix D

Fourier Anomalies

The standard Fourier operator,Ω , is described in Equation 3.2.1. This operator may be modified to include anomalies in the Fourier encoding procedure, produced by T_2^* decay and B-field inhomogeneity. Each anomaly introduces time dependent exponential terms to the signal equation as shown in Equation 3.6. The exponential terms for T_2^* andΔ B, denoted as $\mathcal{E}(k_x, k_y, x, y)$, may be considered with their real and imaginary components through the Euler identity,

$$\begin{aligned} \mathcal{E}(k_x, k_y, x, y) &= e^{-t(k_x,k_y)/T_2^*(x,y)} e^{i\gamma\Delta B(x,y)t(k_x,k_y)} && \text{(D.0.1)} \\ &= e^{-t(k_x,k_y)/T_2^*(x,y)} \cos(\gamma\Delta B(x,y)t(k_x,k_y)) \\ &\quad + ie^{-t(k_x,k_y)/T_2^*(x,y)} \sin(\gamma\Delta B(x,y)t(k_x,k_y)). && \text{(D.0.2)} \end{aligned}$$

These multiplicative terms may be included in the Fourier matrix with encoding anomalies as

$$\Omega_a = \Omega. * \begin{pmatrix} \Re(\mathcal{E}(1,1,1,1)) & \cdots \Re & (\mathcal{E}(m,n,1,1)) & -\Im(\mathcal{E}(1,1,1,1)) & \cdots -\Im & (\mathcal{E}(m,n,1,1)) \\ \vdots & \ddots & \vdots & \vdots & \ddots & \vdots \\ \Re(\mathcal{E}(1,1,m,1)) & \cdots \Re & (\mathcal{E}(m,n,m,1)) & -\Im(\mathcal{E}(1,1,m,1)) & \cdots -\Im & (\mathcal{E}(m,n,m,1)) \\ \Re(\mathcal{E}(1,1,1,2)) & \cdots \Re & (\mathcal{E}(m,n,1,2)) & -\Im(\mathcal{E}(1,1,1,2)) & \cdots -\Im & (\mathcal{E}(m,n,m,2)) \\ \vdots & \ddots & \vdots & \vdots & \ddots & \vdots \\ \Re(\mathcal{E}(1,1,m,n)) & \cdots \Re & (\mathcal{E}(m,n,m,n)) & -\Im(\mathcal{E}(1,1,m,m)) & \cdots -\Im & (\mathcal{E}(m,n,m,n)) \\ \Im(\mathcal{E}(1,1,1,1)) & \cdots \Im & (\mathcal{E}(m,n,1,1)) & \Re(\mathcal{E}(1,1,1,1)) & \cdots \Re & (\mathcal{E}(m,n,1,1)) \\ \vdots & \ddots & \vdots & \vdots & \ddots & \vdots \\ \Im(\mathcal{E}(1,1,m,n)) & \cdots \Im & (\mathcal{E}(m,n,m,n)) & \Re(\mathcal{E}(1,1,m,n)) & \cdots \Re & (\mathcal{E}(m,n,m,n)) \end{pmatrix}, \quad \text{(D.0.3)}$$

where $.*$ indicates point-wise multiplication of the matrices. Clearly the form of T_2^* andΔ B are dependent upon the physical system being imaged.

Appendix E

Censoring and Reordering Acquired Data

As acquired, the EPI k-space data is not in a format appropriate for the developed Fourier operators. Extra data must be censored, data acquired with negative frequency encoding gradients must be reversed, and the real data must be segregated from the imaginary data.

First, the extra points acquired during the phase encoding blips must be censored. A binary censoring matrix of dimension $2mn \times 2m(n+e)$ is used to multiply $\mathcal{S}$. The censoring matrix is an identity matrix with the rows corresponding to the extra acquired points omitted. Mathematically, this can be described using the Kronecker product. Thus, the censoring matrix, C, is the Kronecker product of an identity matrix with a non-square matrix which includes an identity matrix and an $2n \times 2e$ matrix of zeros denoted by $Z(2n, 2e)$:

$$C = I_m \otimes [I_{2n}, Z(2n, 2e)]. \tag{E.0.1}$$

Thus, the extraneous points acquired during the phase encoding blips are removed

through the use of the censoring matrix, $\mathcal{S}_C = C\mathcal{S}$. A toy example of a censoring matrix for an 8×8 array of k-space measurements with 1 point acquired during the phase encoding blips is shown in Figure 3.1(d).

With the removal of the points acquired during the phase encoding blips, $\mathcal{S}_C$ contains only the k-space observations that are on the k-space grid. The second step is to re-order the alternating lines where the data is collected with negative frequency encoding gradients. This is slightly more complicated than simply reversing the data as it is still in real-imaginary pairs which would be swapped to imaginary-real pairs if only row reversal was performed. Again, a Kronecker product is used to construct the row reversal operator, $\mathcal{R}$. To construct $\mathcal{R}$, a Kronecker product between $\mathcal{I}$, a "reverse identity" matrix, to reverse the row, and an identity matrix, to preserve the real-imaginary pairs, is used:

$$\mathcal{R} = \mathcal{I}_n \otimes I_2. \tag{E.0.2}$$

To apply this row reversal to only even lines, an alternating row reversal matrix, R, must be constructed. This is the Kronecker product between an identity matrix and a block, B, which preserves one row and reverses one row. Thus, the block is defined to be

$$B = \begin{pmatrix} I_{2n} & Z(2n, 2n) \\ Z(2n, 2n) & \mathcal{R} \end{pmatrix}, \tag{E.0.3}$$

and the alternating row reversal matrix is thusly

$$R = I_{m/2} \otimes B. \tag{E.0.4}$$

Note that this assumes an acquisition with reversed even rows, although an acquisition with reversed odd rows would require the trivial change of switching the positions of I_{2n} and $\mathcal{R}$ in B. With the alternating row reversal matrix constructed, the alternating row reversal can be easily performed: $\mathcal{S}_{RC} = R\mathcal{S}_C$. A toy example of an alternating row reversal matrix for an 8×8 k-space data set is shown in Figure 3.1(e).

The final step of converting $\mathcal{S}$ to s involves reordering $\mathcal{S}_{\mathcal{RC}}$ to include the real observations stacked above the imaginary observations. This operation is performed by a permutation matrix, P_C, which can be constructed by interleaving the columns of two non-square matrices. These matrices include $P_{C1} = [I_{mn}; Z(mn, mn)]$ and $P_{C2} = [Z(mn, mn); I_{mn}]$. The columns of these matrices are interleaved to produce P_C by taking the first column of P_{C1} followed by the first column of P_{C2} and so on. This real-imaginary reordering can be performed through matrix multiplication to yield the data ordering required in Equation 3.1, $s = P_C\mathcal{S}_{RC}$. An example assuming an 8×8 k-space acquisition is shown in Figure 3.1(f).

Appendix F

Nyquist Ghost Correction

Even and odd lines may be shifted in opposite directions to correct for the Nyquist ghost introduced from eddy current effects in EPI. This may be performed through the use of the Fourier shift theorem. The three operators which are described in this section reorder the data into sets of real and imaginary data for each row, Fourier transform each row, and apply a phase shift to the Fourier transformed row.

The permutation matrix is a binary matrix which can be constructed by interleaving blocks of columns of two non-square matrices to create a square matrix. The two matrices to be interleaved are $P_{R1} = [I_{mn},\ Z(mn, mn)]$ and $P_{R2} = [Z(mn, mn),\ I_{mn}]$. The permutation matrix, P_R, results from taking the first n columns of P_{R1} followed by the first n columns of P_{R2}, and so on. The signal is thus re-ordered to a column vector of the reals stacked above the imaginaries for each row through multiplication with P_R. As this is a permutation matrix, its inverse is simply its transpose. A graphical representation of P_R for an 8×8 k-space acquisition is shown in Figure 3.1(g).

The row Fourier transform matrix is the Kronecker product of an identity matrix with the Fourier transform matrixΩ_x, as defined earlier,$\Omega_{row} = I_m \otimes \Omega_x$. A graphical representation ofΩ_{row} for an 8×8 k-space acquisition is shown in Figure 3.1(h).

The phase shift operator is the final necessary operator for performing a line shift. This operator multiplies the complex-valued Fourier transform of the line by a complex-valued exponential to implement the Fourier shift theorem. For a shift of ϕ, the j^{th} element of the row must be multiplied by $\exp(-i2\pi\phi j/n)$, or equivalently $\cos(2\pi\phi j/n) - i\sin(2\pi\phi j/n)$. Thus, the real component of the phase shifted j^{th} element is $\Re(f_j)\cos(2\pi\phi j/n) - \Im(f_j)\sin(2\pi\phi j/n)$, where f_j is the j^{th} element of the Fourier transformed row. Similarly, the imaginary component of the phase shifted j^{th} element is $\Re(f_j)\sin(2\pi\phi j/n) + \Im(f_j)\cos(2\pi\phi j/n)$. Thus, for a row, this phase shift matrix operator is

$$\zeta = \begin{pmatrix} \cos(2\pi\phi 1/n) & \cdots & 0 & -\sin(2\pi\phi 1/n) & \cdots & 0 \\ \vdots & \ddots & \vdots & \vdots & \ddots & \vdots \\ 0 & \cdots & \cos(2\pi\phi n/n) & 0 & \cdots- & \sin(2\pi\phi n/n) \\ \sin(2\pi\phi 1/n) & \cdots & 0 & \cos(2\pi\phi 1/n) & \cdots & 0 \\ \vdots & \ddots & \vdots & \vdots & \ddots & \vdots \\ 0 & \cdots & \sin(2\pi\phi n/n) & 0 & \cdots & \cos(2\pi\phi n/n) \end{pmatrix}. \qquad \text{(F.0.1)}$$

Shifting a row to the right by ϕ pixels is denoted by ζ^+ while shifting a row to the left by ϕ pixels is denoted by ζ^-. With this representation, the phase shifting of lines in alternating directions is denoted by $\Phi = I_{m/2} \otimes [\zeta^+,\ Z(2n,2n); Z(2n,2n),\ \zeta^-]$. A graphical representation of $\Phi$with $\phi = 0.5$ and an 8×8 acquisition matrix is shown in Figure 3.1(i).

Appendix G

Partial Fourier Interpolation

Conjugate symmetry ideally exists about the origin in k-space, as the reconstructed image is expected to be real-valued. This symmetry allows half of k-space to be generated without being acquired. Thus the acquired data array, s, only requires $2(m/2+1)n$ elements while the symmetrically generated data array, s_S, is $2mn$ elements. For the sake of consistency in notation, we assume that the remaining $2(m/2-1)n$ elements in s are set to zero with the last $(m/2-1)n$ real observations being zero and the last $(m/2-1)n$ imaginary observations being zero. An equivalent symmetric k-space generation operator can be constructed which does not include these zero elements thereby reducing the operator size. However, in the considered case a square matrix, H, can be used for partial Fourier reconstruction. For the acquired real and imaginary points, the partial Fourier operator returns the observed values. For the generated point $(k_x,\ k_y)$, the partial Fourier operator returns the complex conjugate of the observed point at $(-k_x,\ -k_y)$. This partial Fourier operator multiplies the uncollected points by zero, so the values originally substituted

into these points are irrelevant. The partial Fourier operator is thusly a $2mn \times 2mn$ matrix. This matrix which includes identity, I, "reverse identity," $\mathcal{I}$, and zero, Z, matrices is:

$$H = \begin{pmatrix} I_{(m/2+1)n} & Z((m/2+1)n, (m/2-1)n) & Z((m/2+1)n, mn) \\ Z((m/2-1)n, n) & \mathcal{I}_{(m/2-1)n} & Z((m/2-1)n, \frac{3}{2}mn) \\ Z((m/2-1)n, mn) & I_{(m/2+1)n} & Z((m/2+1)n, (m/2-1)n) \\ Z((m/2-1)n, (m+1)n) & -\mathcal{I}_{(m/2-1)n} & Z((m/2-1)n, \frac{m}{2}n) \end{pmatrix}. \quad \text{(G.0.1)}$$

A graphical representation of H is shown in Figure 3.1(j) for the case of an 8×8 symmetric k-space.

Appendix H

Convolution

We will first describe the zero filling operator, F, and then describe the apodization operator, A, which includes the typical Fermi apodization window and Gaussian smoothing window as specific cases. We will finally describe the image-space magnitude smoothing operator.

Zero-filling is often performed to yield an increase in apparent reconstructed resolution and to create an array which has dimensions of an integer power of two for fast Fourier transform routines [Gonzalez and Woods, 1992]. In zero-filling, zeros are appended to the acquired k-space observations at higher spatial frequencies than are observed. It is well known that zero-filling is equivalent to image-space convolution with a sinc kernel. The zero-filling is done symmetrically to preserve the location of the k-space origin in the zero-filled array at $(m/2+1, n/2+1)$. The zero filling matrix is a binary matrix containing blocks of zero and identity matrices. This parameterization of the zero-filling operator assumes that an even number of phase encode points, $\mathscr{P}$, and an even number of frequency points, $\mathscr{F}$, are to be added to

the acquired data. The zero-filling operator is denoted as

$$F = I_2 \otimes \begin{pmatrix} F_{\mathscr{P}} \\ I_m \otimes F_{\mathscr{F}} \\ F_{\mathscr{P}} \end{pmatrix} \tag{H.0.1}$$

where

$$F_{\mathscr{P}} = Z(\mathscr{P}/2, mn) \tag{H.0.2}$$

and

$$F_{\mathscr{F}} = \begin{pmatrix} Z(\mathscr{F}/2, n) \\ I_n \\ Z(\mathscr{F}/2, n) \end{pmatrix}. \tag{H.0.3}$$

Thus, zeros are appended symmetrically around the acquired k-space matrix. It should be noted that this changes the dimensionality of s, and subsequent operators must be appropriately adjusted. An example of F is shown in Figure 3.1(k) for zero filling a 4×4 k-space data set to an 8×8 data set.

Apodization and filtering can be considered with the Fourier convolution theorem, where convolution with a kernel in image space is simply point-wise multiplication of the Fourier transform of the original kernel in k-space. Thus, any processing step which involves the point-wise multiplication of k-space observations with a kernel or the image-space convolution of the complex-valued image with a kernel can be considered with the apodization operator presented here. This apodization operator, A, is a diagonal matrix in which the non-zero elements correspond to the values of the k-space kernel for those points. If the values of the k-space kernel, K, are indexed

across rows such that the first element of the first row is 1, the last element of the first row is n, the first element of the second row is $n + 1$, and so on, the elements of A are easily defined such that $A_{j,j} = K(j)$. An example of A is shown in Figure 3.1(l) for the case of a simple 8×8 Hanning k-space window.

Explicit image smoothing is often performed on the reconstructed magnitude data. Such a process is different from smoothing the complex data [Lai et al., 1996] and is a non-linear process. However, with the magnitude squared covariance matrix known from the complex-valued covariance matrix, an operator, S_{mm}, may be developed to consider smoothing magnitude squared data. The first row of the operator consists of the kernel weights for each magnitude squared data point for the first smoothed magnitude squared data point. The second row includes the weights for the second point, and so on. An operator for smoothing an 8×8 data set with a Gaussian kernel with a 3 voxel FWHM is shown in Figure 3.1(m). If image-space smoothing of the complex-valued data were preferred over k-space apodization, a complex-data smoothing operator, S_m could be constructed as a block diagonal operator where the two diagonal blocks are filled with S_{mm}.

Appendix I

Estimators for the Alternative Hypothesis

The maximum likelihood estimators for the alternative hypothesis may be derived by maximizing the probability distribution. We consider the model in a given voxel with n real and n imaginary observations

$$\begin{pmatrix} y_R \\ y_I \end{pmatrix} = \begin{pmatrix} CX\beta \\ SX\beta \end{pmatrix} + \begin{pmatrix} \eta_R \\ \eta_I \end{pmatrix}, \qquad \begin{pmatrix} \eta_R \\ \eta_I \end{pmatrix} \sim N\left(0, \sigma^2\Sigma_v\right).$$

The probability distribution for this model is

$$L = (2\pi\sigma^2)^{-2n/2}|\Sigma_v|^{-1/2} \exp\left[-\frac{1}{2\sigma^2}\begin{pmatrix} y_R - CX\beta \\ y_I - SX\beta \end{pmatrix}' \Sigma_v^{-1} \begin{pmatrix} y_R - CX\beta \\ y_I - SX\beta \end{pmatrix}\right].$$

Maximizing the logarithm of the probability distribution maximizes the probability distribution while simplifying the mathematics. The logarithm of the probability

distribution is

$$LL = \frac{-2n}{2}\log(2\pi\sigma^2) - \frac{1}{2}\log(|\Sigma_v|) + \left[-\frac{1}{2\sigma^2} \begin{pmatrix} y_R - CX\beta \\ y_I - SX\beta \end{pmatrix}' \Sigma_v^{-1} \begin{pmatrix} y_R - CX\beta \\ y_I - SX\beta \end{pmatrix} \right].$$

Following the notation of the manuscript, letΣ_v^{-1} be partitioned into four $n \times n$ matrices

$$\Sigma_v^{-1} = \begin{pmatrix} \Sigma_A & \Sigma_B \\ \Sigma_C & \Sigma_D \end{pmatrix}.$$

This inverse matrix may be determined by solving$\Sigma_v \Sigma_v^{-1} = I$ to yield the values shown in Equations 4.8, 4.9, 4.10, and 4.11. For simplicity in notation, let the matrix product be represented by α

$$\begin{aligned} \alpha &= \begin{pmatrix} y_R - CX\beta \\ y_I - SX\beta \end{pmatrix}' \Sigma_v^{-1} \begin{pmatrix} y_R - CX\beta \\ y_I - SX\beta \end{pmatrix} \\ &= y_R'\Sigma_A y_R - 2y_R'\Sigma_A CX\beta + \beta' X'C'\Sigma_A CX\beta + \\ &\quad y_I'\Sigma_C y_R - y_I'\Sigma_C CX\beta - \beta' X'S'\Sigma_C y_R + \beta' X'S'\Sigma_C CX\beta + \\ &\quad y_R'\Sigma_B y_I - y_R'\Sigma_B SX\beta - \beta' X'C'\Sigma_B y_I + \beta' X'C'\Sigma_B SX\beta + \\ &\quad y_I'\Sigma_D y_I - 2y_I'\Sigma_D SX\beta + \beta' X'S'\Sigma_D SX\beta. \end{aligned}$$

Thus, the logarithm of the probability distribution may be written more concisely as

$$LL = -\frac{2n}{2}\log(2\pi\sigma^2) - \frac{1}{2}\log(|\Sigma_v|) + \left(-\frac{\alpha}{2\sigma^2}\right).$$

Differentiating the the logarithm of the probability distribution with respect to β yields

$$\begin{aligned}\frac{\partial LL}{\partial \beta} &= \frac{1}{2\sigma^2}\frac{\partial \alpha}{\partial \beta} \\ &= \frac{1}{2\sigma^2}\left(-2y_R'\Sigma_A CX + 2X'C'\Sigma_A CX\beta - \right. \\ &\quad y_I'\Sigma_C CX - X'S'\Sigma_C y_R + 2X'S'\Sigma_C CX\beta - \\ &\quad y_R'\Sigma_B SX - X'C'\Sigma_B y_I + 2X'C'\Sigma_B SX\beta - \\ &\quad \left. 2\, y_I'\Sigma_D SX + 2X'S'\Sigma_D SX\beta\right)\end{aligned}$$

Setting this equal to zero and solving for β yields the maximum likelihood estimator for β

$$\begin{aligned}\hat{\beta} = &\left(2\hat{C}'X'\Sigma_A X\hat{C} + 2\hat{S}'X'\Sigma_C X\hat{C} + 2\hat{C}'X'\Sigma_B X\hat{S} + 2\hat{S}'X'\Sigma_D X\hat{S}\right)^{-1} \\ &\times \left(2y_R'\Sigma_A X\hat{C} + y_I'\Sigma_C X\hat{C} + \hat{S}'X'\Sigma_C y_R + \right. \\ &\left. y_R'\Sigma_B X\hat{S} + \hat{C}'X'\Sigma_B y_I + 2y_I\Sigma_D X\hat{S}\right)\end{aligned}$$

Differentiating the logarithm of the probability distribution with respect to σ^2 yields

$$\frac{\partial LL}{\partial \sigma^2} = -\frac{n}{\sigma^2} + \frac{\alpha}{2\sigma^4}.$$

Setting this equal to zero and solving for σ^2 yields the maximum likelihood estimator for σ^2

$$\hat{\sigma}^2 = \frac{\hat{\alpha}}{2n}.$$

Following the notation of the manuscript,

$$\begin{aligned} \hat{C} &= \cos(\hat{\theta}) I_n \\ \hat{S} &= \sin(\hat{\theta}) I_n, \end{aligned}$$

and $\hat{\theta}$ may be estimated with the method of moments

$$\hat{\theta} = \arctan\left(\frac{1/n \sum_{t=1}^{n} \sin(\hat{\theta}_t)}{1/n \sum_{t=1}^{n} \cos(\hat{\theta}_t)} \right).$$

Appendix J

Estimators for the Null Hypothesis

The maximum likelihood estimators for the null hypothesis under which $V\beta = \delta$ may be derived by maximizing the probability distribution with a Lagrange multiplier. The function to be maximized is thus

$$\begin{aligned} h &= LL - \frac{1}{2\sigma^2}\psi'\left(V\beta - \delta\right) \\ &= -n\log(2\pi\sigma^2) - \frac{1}{2}\log(|\Sigma_v|) - \frac{1}{2\sigma^2}\left(\alpha + \psi'\left(V\beta - \delta\right)\right), \end{aligned}$$

where α is as defined in Appendix I. Differentiating h with respect to ψ yields

$$\frac{\partial h}{\partial \psi} = \frac{\delta - V\beta}{2\sigma^2}$$

Setting the above equation equal to zero and solving for ψ produces the maximum likelihood estimator for ψ under the null hypothesis

$$\begin{aligned}\tilde{\psi} = & \left[V\left(2X'\tilde{C}'\Sigma_A\tilde{C}X + 2X'\tilde{S}'\Sigma_C\tilde{C}X + 2X'\tilde{C}'\Sigma_B\tilde{S}X + 2X'\tilde{S}'\Sigma_D\tilde{S}X\right)^{-1}V'\right]^{-1} \\ & \times \left[V\left(2X'\tilde{C}'\Sigma_A\tilde{C}X + 2X'\tilde{S}'\Sigma_C\tilde{C}X + 2X'\tilde{C}'\Sigma_B\tilde{S}X + 2X'\tilde{S}'\Sigma_D\tilde{S}X\right)^{-1}\right. \\ & \times \left(2y_R'\Sigma_A\tilde{C}X + y_I'\Sigma_C\tilde{C}X + X'\tilde{S}'\Sigma_C y_R + \right. \\ & \left.\left. y_R'\Sigma_B\tilde{S}X + X'\tilde{C}'\Sigma_B y_I + 2y_I'\Sigma_D\tilde{S}X\right) - \delta\right].\end{aligned}$$

Differentiating h with respect to β yields

$$\frac{\partial h}{\partial \beta} = \frac{1}{2\sigma^2}\left(\frac{\partial \alpha}{\partial \beta} + \psi' V\right).$$

Setting the above equation equal to zero and solving for β produces the maximum likelihood estimator for β under the null hypothesis

$$\begin{aligned}\tilde{\beta} = & \left(2X'\tilde{C}'\Sigma_A\tilde{C}X + 2X'\tilde{S}'\Sigma_C\tilde{C}X + 2X'\tilde{C}'\Sigma_B\tilde{S}X + 2X'\tilde{S}'\Sigma_D\tilde{S}X\right)^{-1} \\ & \times \left(2y_R'\Sigma_A\tilde{C}X + y_I'\Sigma_C\tilde{C}X + X'\tilde{S}'\Sigma_C y_R + \right. \\ & \left. y_R'\Sigma_B\tilde{S}X + X'\tilde{C}'\Sigma_B y_I + 2y_I'\Sigma_D\tilde{S}X - \tilde{\psi}'V\right).\end{aligned}$$

Similar to the alternative hypothesis case, the matrix product $\tilde{\alpha}$ is

$$\begin{aligned}\tilde{\alpha} = & y_R'\Sigma_A y_R - 2y_R\Sigma_A\tilde{C}X\tilde{\beta} + \tilde{\beta}'X'\tilde{C}'\Sigma_A\tilde{C}X\tilde{\beta} + \\ & y_I'\Sigma_C y_R - y_I'\Sigma_C\tilde{C}X\tilde{\beta} - \tilde{\beta}'X'\tilde{S}'\Sigma_C y_R + \tilde{\beta}'X'\tilde{S}'\Sigma_C\tilde{C}X\tilde{\beta} + \\ & y_R'\Sigma_B y_I - y_R'\Sigma_B\tilde{S}X\tilde{\beta} - \tilde{\beta}'X'\tilde{C}'\Sigma_B y_I + \tilde{\beta}'X'\tilde{C}'\Sigma_B\tilde{S}X\tilde{\beta} + \\ & y_I'\Sigma_D y_I - 2y_I\Sigma_D\tilde{S}X\tilde{\beta} + \tilde{\beta}'X'\tilde{S}'\Sigma_D\tilde{S}X\tilde{\beta}\end{aligned}$$

Differentiating with respect to σ^2 yields

$$\frac{\partial h}{\partial \sigma^2} = -\frac{n}{\sigma^2} + \frac{1}{2\sigma^4}\left(\alpha + \psi'\left(V\beta - \delta\right)\right).$$

Setting this equal to zero and solving for σ^2 yields the maximum likelihood estimator for σ^2 under the null hypothesis

$$\tilde{\sigma}^2 = \frac{\tilde{\alpha} + \tilde{\psi}'\left(V\tilde{\beta} - \delta\right)}{2n}.$$

Following the notation of the manuscript,

$$\begin{aligned}\tilde{C} &= \cos(\tilde{\theta})I_n \\ \tilde{S} &= \sin(\tilde{\theta})I_n,\end{aligned}$$

and $\tilde{\theta}$ may be estimated with the method of moments

$$\tilde{\theta} = \arctan\left(\frac{1/n\sum_{t=1}^{n}\sin(\tilde{\theta}_t)}{1/n\sum_{t=1}^{n}\cos(\tilde{\theta}_t)}\right).$$

Bibliography

P. A. Bandettini, A. Jesmanowicz, E. C. Wong, and J. S. Hyde. Processing strategies for time-course data sets in functional MRI of the human brain. *Magnetic Resonance in Medicine*, 30:161–173, 1993.

R. L. Barry, J. M. Williams, L. M. Klassen, J. C. Culham, and R. S. Menon. Preprocessing pipeline considerations to compensate for paradigm-related subject movement. *Proceedings of the International Society of Magnetic Resonance in Medicine*, 16:2473, 2008.

M. A. Bernstein, K. F. King, and X. J. Zhou. *Handbook of MRI Pulse Sequences*. Academic Press, New York, 2004.

M. Bianciardi, M. Fukunaga, P. van Gelderen, S. G. Horovitz, J. A. de Zwart, K. Shmueli, and J. H. Duyn. Sources of functional magnetic resonance imaging signal fluctuations in the human brain at rest: a 7 T study. *Magnetic Resonance Imaging*, In Press, doi:10.1016/j.mri.2009.02.004, 2009.

R. M. Birn, J. B. Diamond, M. A. Smith, and P. A. Bandettini. Separating respiratory-variation-related fluctuations from neuronal-activity-related fluctuations in fMRI. *NeuroImage*, 31:1536–1548, 2006.

B. B. Biswal, F. Z. Yetkin, V. M. Haughton, and J. S. Hyde. Functional connectivity in the motor cortex of resting human brain using echo-planar MRI. *Magnetic Resonance in Medicine*, 34:537–541, 1995.

G. Casella and R. L. Berger. *Statistical Inference*. Wadsworth and Brooks/Cole, Pacific Grove, CA, 1990.

C. Chang and G. H. Glover. Effects of model-based physiological noise correction on default mode network anti-correlations and correlations. *NeuroImage*, In Press, doi:10.1016/j.neuroimage.2009.05.012, 2009.

R. W. Cox. AFNI: Software for analysis and visualization of functional magnetic resonance neuroimages. *Computers and Biomedical Research*, 29:162–173, 1996.

R. W. Cox, A. Jesmanowicz, and J. S. Hyde. Real-time functional magnetic resonance imaging. *Magnetic Resonance in Medicine*, 33:230–236, 1995.

V. Della-Maggiore, W. Chau, P. R. Peres-Neto, and A. R. McIntosh. An empirical comparison of SPM preprocessing parameters to the analysis of fMRI data. *NeuroImage*, 17:19–28, 2002.

J. Dongarra. Basic linear algebra subprograms technical forum standard. *International Journal of High Performance Applications and Supercomputing*, 16:1–111, 2002a.

J. Dongarra. Basic linear algebra subprograms technical forum standard. *International Journal of High Performance Applications and Supercomputing*, 16:115–199, 2002b.

Z. Feng, A. Caprihan, K. Blagoev, F. Zhao, and V. C. Calhoun. Modeling of phase changes in BOLD fMRI. *Proceedings of the International Society of Magnetic Resonance in Medicine*, 16:2490, 2008.

Z. Feng, A. Caprihan, K. B. Blagoev, and V. D. Calhoun. Biophysical modeling of phase changes in BOLD fMRI. *NeuroImage*, In Press, doi:10.1016/j.neuroimage.2009.04.076, 2009.

L. Friedman, G. H. Glover, D. Krenz, V. Magnotta, and The FIRST BIRN. Reducing inter-scanner variability of activation in a multicenter fMRI study: Role of smoothness equalization. *NeuroImage*, 32:1656–1668, 2006.

K. J. Friston, C. D. Frith, P. F. Liddle, and R. S. Frackowiak. Functional connectivity: the principle component analysis of large (PET) data sets. *Journal of Cerebral Blood Flow and Metabolism*, 13:5–14, 1993.

K. J. Friston, A. P. Holmes, K. J. Worsley, J. P. Poline, C. D. Frith, and R. S. J. Frackowiak. Statistical parametric maps in functional imaging: A general linear approach. *Human Brain Mapping*, 2:189–210, 1995.

G. H. Glover, T. Q. Li, and D. Ress. Image-based method for retrospective correction of physiological motion effects in fMRI: RETROICOR. *Magnetic Resonance in Medicine*, 44:162–167, 2000.

R. C. Gonzalez and R. E. Woods. *Digital Image Processing*. Addison-Wesley Publishing Company, Reading, MA, USA, 1992.

A. Gretton, A. Belitski, Y. Murayama, B. Scholkopf, and N Logothetis. The effect of artifacts on dependence measurement in fMRI. *Magnetic Resonance Imaging*, 24: 401–409, 2006.

A. C. Guyton and J. E. Hall. *Textbook of Medical Physiology*. Saunders, Philadelphia, PA, 10 edition, 2000.

E. M. Haacke, R. Brown, M. Thompson, and R. Venkatesan. *Magnetic Resonance Imaging: Physical Principles and Sequence Design*. John Wiley and Sons, New York, NY, USA, 1999.

A. D. Hahn, A. S. Nencka, and D. B. Rowe. Dynamic compensation of B_0 field inhomogeneities restores complex fMRI time series activation power. *Proceedings of the International Society of Magnetic Resonance in Medicine*, 16:1251, 2008.

A. D. Hahn, A. S. Nencka, and D. B. Rowe. Improving robustness and reliability of phase-sensitive fMRI analysis using Temporal Off-resonance Alignment of Single-echo Timeseries (TOAST). *NeuroImage*, 44:742–752, 2009.

R. N. A. Henson, C. Buchel, O. Josephs, and K. J. Friston. The slice-timing problem in event-related fMRI. In *NeuroImage*, volume 9, page 125, 1999.

S. A. Huettel, A. W. Song, and G. McCarthy. *Functional magnetic resonance imaging*. Sinauer Associates, Inc., Sunderland, MA, USA, 2004.

K. A. Jain. *Fundamentals of Digital Image Processing*. Prentice Hall, Englewood Cliffs, NJ, 1989.

S. Jammalamadaka and A. SenGupta. *Topics in Circular Statistics*. World Scientific, Singapore, 2001.

M. Jenkinson, P. R. Bannister, J. M. Brady, and S. M. Smith. Improved optimisation for the robust and accurate linear registration and motion correction of brain images. *NeuroImage*, 17:825–841, 2002.

A. Jesmanowicz, E. C. Wong, and J. S. Hyde. Phase correction for EPI using internal reference lines. *Proceedings of the Society of Magnetic Resonance in Medicine*, 12: 1239, 1993.

A. Jesmanowicz, E. C. Wong, and J. S. Hyde. Self correcting EPI reconstruction algorithm. *Proceedings of the International Society of Magnetic Resonance in Medicine*, 3:619, 1995.

A. Jesmanowicz, P.A. Bandettini, and J. S. Hyde. Single-shot half k-space high-resolution gradient-recalled EPI for fMRI at 3 Tesla. *Magnetic Resonance in Medicine*, 40:754–762, 1998.

P. Jezzard and R.S. Balaban. Correction for geometric distortion in echo planar images from B_0 field variations. *Magnetic Resonance in Medicine*, 34:65–73, 1995.

L. Klassen and R. Menon. BOLD signal phase and magnitude dependence on vessel geometry. *Proceedings of the International Society of Magnetic Resonance in Medicine*, 13:496, 2005.

N. Kriegeskorte, N. J. Bodurka, and P. A. Bandettini. Artifactual time course corre-

lations in echo-planar fMRI with implications for studies of brain function. *International Journal of Imaging Systems and Technology*, In Press.

S. LaConte, Jon Anderson, Suraj Muley, James Ashe, Sally Frutiger, Kelly Rehm, Lars Kai Hansen, Essa Yacoub, Xiaoping Hu, David Rottenberg, and Stephen Strother. The evaluation of preprocessing choices in single-subject BOLD fMRI using NPAIRS performance metrics. *NeuroImage*, 18:10–27, 2003.

S. Lai and G. H. Glover. Detection of BOLD fMRI signals using complex data. *Proceedings of the International Society of Magnetic Resonance in Medicine*, 3: 1671, 1997.

S. Lai, J. R. Reichenbach, and E. M. Haacke. Commutator filter: A novel technique for the identification of structures producing significant susceptibility inhomogeneities and its application to functional MRI. *Magnetic Resonance in Medicine*, 36:781–7, 1996.

F. Lamberton, N. Delcroix, D. Grenier, B. Mazoyer, and M. Joliot. A new EPI-based dynamic field mapping method: application to retrospective geometrical distortion corrections. *Journal of Magnetic Resonance Imaging*, 26:747–755, 2007.

H. W. Lilliefors. On the Kolmogorov-Smirnov test for normality with mean and variance unknown. *American Statistical Association Journal*, 62:399–402, 1967.

B. R. Logan and D. B. Rowe. An evaluation of thresholding techniques in fMRI analysis. *NeuroImage*, 22:95–108, 2004.

B. R. Logan, M. P. Geliazkova, and D. B. Rowe. An evaluation of spatial thresholding techniques in fMRI analysis. *Human Brain Mapping*, In Press, 2008.

N. K. Logothetis. The underspinnings of the bold functional magnetic resonance imaging signal. *The Journal of Neuroscience*, 23:3963–3971, 2003.

W. L. Lou and T. E. Nichols. Diagnosis and exploration of massively univariate neuroimaging models. *NeuroImage*, 19:1014–1032, 2003.

R. E. Martin, B. J. MacIntosh, R. C. Smith, A. M. Barr, T. K. Stevens, J. S. Gati, and R. S. Menon. Cerebral areas processing swallowing and tongue movement are overlapping but distinct: A functional magnetic resonance imaging study. *Journal of Neurophysiology*, 92:2428–2443, 2004.

R. S. Menon. Postacquisition suppression of large-vessel BOLD signals in high-resolution fMRI. *Magnetic Resonance in Medicine*, 47:1–9, 2002.

K. Murphy, R. M. Birn, D. A. Handwerker, T. B. Jones, and P. A. Bandettini. The impact of global signal regression on resting state correlations: are anti-correlated networks introduced? *NeuroImage*, 44:893–905, 2008.

F. Y. Nan and R. D. Nowak. Generalized likelihood ratio detection for fMRI using complex data. *I.E.E.E. Transactions on Medical Imaging*, 18:320–329, 1999.

A. S. Nencka and D. B. Rowe. Complex constant phase method removes venous BOLD component in fMRI. *Proceedings of the International Society of Magnetic Resonance in Medicine*, 13:495, 2005.

A. S. Nencka and D. B. Rowe. Theoretical results demonstrate fundamental differences in venous BOLD reducing fMRI activation methods. *Proceedings of the International Society of Magnetic Resonance in Medicine*, 14:3269, 2006.

A. S. Nencka and D. B. Rowe. Apodization and smoothing alter voxel time series correlations. *Proceedings of the International Society of Magnetic Resonance in Medicine*, 16:2457, 2008.

A. S. Nencka and D. B. Rowe. Image space correlations induced by k-space processes. *Proceedings of the Organization for Human Brain Mapping*, 13, 2007a.

A. S. Nencka and D. B. Rowe. Reducing the unwanted draining vein BOLD contribution in fMRI with statistical post-processing methods. *NeuroImage*, 37:177–188, 2007b.

A. S. Nencka, A. D. Hahn, and D. B. Rowe. The use of three navigator echoes in Cartisian EPI reconstruction reduces Nyquist ghosting. *Proceedings of the International Society of Magnetic Resonance in Medicine*, 16:3032, 2008.

A. S. Nencka, A. D. Hahn, and D. B. Rowe. A Mathematical Model for Understanding the STatistic al effects of k-space (AMMUST-k) preprocessing on observed voxel measurements in fcMRI and fMRI. *Journal of Neruoscience Methods*, In Press, 2009.

D. C. Noll, C. H. Meyer, J. M. Pauly, D. G. Nishimura, and A. Macovski. A homogeneity correction method for magnetic resonance imaging with time-varying gradients. *I.E.E.E. Transactions on Medical Imaging*, 10:629–637, 1991.

D. C. Noll, J. M. Pauly, C. H. Meyer, D. G. Nishimura, and A. Macovski. Debluring for non-2D Fourier transform magnetic resonance imaging. *Magnetic Resonance in Medicine*, 25:319–333, 1992.

S. Ogawa, R. S. Menon, D. W. Tank, S. G. Kim, H. Merkle, J. M. Ellermann, and K. Ugurbil. Functional brain mapping by blood oxygen level-dependent contrast magnetic resonance imaging. *Biophysical Journal*, 64:803–812, 1993.

J. Pfeuffer, P. F. Van de Moortele, K. Ugurbil, X. Hu, and G. H. Glover. Correction of physiologically induced global off-resonance effects in dynamic echo-planar and spiral functional imaging. *Magnetic Resonance in Medicine*, 47:344–353, 2002.

D. Raj, D. P. Paley, A. W. Anderson, R. P. Kennan, and J. C. Gore. A model for susceptibility artefacts from respiration in functional echo-planar magnetic resonance imaging. *Physics in Medicine and Biology*, 45:3809–3820, 2000.

V. Roopchansingh, R. W. Cox, A. Jesmanowicz, B. D. Ward, and J. S. Hyde. Single-shot magnetic field mapping embedded in echo planar time-course imaging. *Magnetic Resonance in Medicine*, 50:839–843, 2003.

D. B. Rowe. Modeling both the magnitude and phase of complex-valued fMRI data. *NeuroImage*, 25:1310–1324, 2005a.

D. B. Rowe. Parameter estimation in the magnitude-only and complex-valued fMRI data models. *NeuroImage*, 25:1124–1132, 2005b.

D. B. Rowe. Complex activation is more focal and concentrated to parenchymal tissue.

Proceedings of the International Society of Magnetic Resonance in Medicine, 13: 1575, 2005c.

D. B. Rowe and B. R. Logan. A complex way to compute fMRI activation. *NeuroImage*, 23:1078–1092, 2004.

D. B. Rowe and B. R. Logan. Complex fMRI analysis with unrestricted phase is equivalent to a magnitude-only model. *NeuroImage*, 24:603–606, 2005.

D. B. Rowe and A. S. Nencka. Complex activation surpresses venous BOLD in GE-EPI fMRI data. *Proceedings of the International Society of Magnetic Resonance in Medicine*, 14:2834, 2006.

D. B. Rowe and A. S. Nencka. Induced correlation in fMRI magnitude data from k-space preprocessing. *Proceedings of the International Society of Magnetic Resonance in Medicine*, 17, 2009.

D. B. Rowe, C. P. Meller, and R. G. Hoffmann. Characterizing phase-only fMRI data with an angular regression model. *Journal of Neuroscience Methods*, 161:331–341, 2007a.

D. B. Rowe, A. S. Nencka, and R. G. Hoffmann. Signal and noise of Fourier reconstructed fMRI data. *Journal of Neuroscience Methods*, 159:361–369, 2007b.

M. E. Shaw, S. C. Strother, M. Gavrilescu, K. Podzebenko, A. Waites, J. Watson, J. Anderson, G. Jackson, and G. Egan. Evaluating subject specific preprocessing choices in multisubject fMRI data sets using data-driven performance metrics. *NeuroImage*, 19:988–1001, 2003.

K. Shmueli, P. van Gelderen, J. A. de Zward, S. G. Horovitz, M. Fukunaga, J. M. Jansma, and J. H. Duyn. Low frequency fluctuations in the cardiac rate as a source of variance in the resting state fMRI BOLD signal. *NeuroImage*, 38:306–320, 2007.

P. Skudlarski, R. T. Constable, and J. C. Gore. ROC analysis of statistical methods used in functional MRI: individual subjects. *NeuroImage*, 9:311–329, 1999.

A. M. Smith, B. K. Lewis, U. E. Ruttimann, F. Q. Ye, T. M. Sinnwell, Y. Yang, J. H. Duyn, and J. A. Frank. Investigation of low frequency drift in fMRI investigation. *NeuroImage*, 9:526–533, 1999.

C. S. Sprenger. *NMR in Physiology and Biomedicine*, chapter Physicochemical principles influencing magnetopharmaceuticals. Academic Press, 1994.

Student. The probable error of a mean. *Biometrika*, 6:1–25, 1908.

B. P. Sutton, D. C. Noll, and J. A. Fessler. Dynamic field estimation using a spiral-in/spiral-out acquisition. *Magnetic Resonance in Medicine*, 51:1194–1204, 2004.

M. Tremblay, F. Tam, and S. J. Graham. Retrospective coregistration of functional magnetic resonance imaging data using external monitoring. *Magnetic Resonance in Medicine*, 53:141–149, 2005.

R. Turner. How much cortex can a vein drain? Downstream dilution of activation-related cerebral blood oxygenation changes. *NeuroImage*, 16:1062–1067, 2002.

V. G. van de Ven, E. Formisano, D. Prvulovic, C. H. Roeder, and D. E. J. Linden. Functional connectivity as revealed by spatial independent component analysis of fMRI measurements during rest. *Human Brain Mapping*, 22:165–178, 2004.

P. van Gelderen, J. A. de Zwart, P. Starewicz, R. S. Hinks, and J. H. Duyn. Real-time shimming to compensate for respiration induced b_0 fluctuations. *Magnetic Resonance in Medicine*, 57:362–368, 2007.

A. Villringer. *Functional MRI*, chapter Physiological changes during brain activation. Springer, 2000.

A. Weissenbacher, C. Kasess, F. Gerstl, R. Lanzenberger, E. Moser, and C. Windischberger. Correlations and anticorrelations in resting-state functional connectivity MRI: A quantitative comparison of preprocessing strategies. *NeuroImage*, In Press, doi:10.1016/j.neuroimage.2009.05.005, 2009.

F. Wilcoxon. Individual comparisons by ranking methods. *Biometrics Bulletin*, 1: 8083, 1945.

F. Zhao, T. Jin, P. Wang, X. Hu, and S.-G. Kim. Sources of phase changes in BOLD and CBV-weighted fMRI. *Magnetic Resonance in Medicine*, 57(3):520–527, 2007.